

ZA-20 Colt

**Proposal for 2018 AIAA Individual
Undergraduate Design Competition**

A-10 Replacement



Ryan Morse

Ryan A. Morse, 2d Lt, USAF
AIAA 921462



Neil R. Weston

Dr. Neil Weston, Instructor



Carl Johnson

Mr. Carl Johnson, Advisor



Table of Contents

Part I: Tables & Figures:.....	4
Part II: Executive Summary:.....	8
Part III: Stakeholder Analysis:.....	10
Part IV: Configuration Selection:	12
Part V: Mission Overview	20
Part VI: Weight Sizing.....	21
Part VII: Weight Sizing Sensitivity Studies.....	27
Part VIII: Constraint Sizing	33
Level Constant Speed Cruise	34
Steady Constant Speed Climb.....	35
Service Ceiling.....	36
Takeoff Distance	37
Approach Speed	39
Load Factor	39
Part IX: Dash Speed, Takeoff Length, and Maximum Load Factor.....	41
Part X: Cost Analysis.....	42
Unit Cost.....	42
Operating Cost	44
Part XI: Optimization Scheme	46
Method	46
Results and A-10 Comparison	49
Part XII: Fuselage Design.....	51
Dimensions and Diagrams	51
Propulsion Integration.....	54



Weapons Integration	55
Landing Gear and Nose Cone	58
Part XIII: Structures Design.....	62
Overall Design	62
Composite Spar Design.....	63
Part XIV: Wing Design.....	71
Part XV: Second Order Aerodynamics.....	76
Part XVI: Weight and Balance	80
Part XVII: Control and Dynamic Stability	84
Appendix: Bibliography.....	91



Part I: Tables & Figures:

Table 1 Stakeholder weightings.....	11
Table 2 Selected components for initial configuration aircraft	12
Table 3 Pugh Matrix for configuration selection.....	13
Table 4 Pugh Matrix for wing attachment	14
Table 5 Pugh Matrix for wing shape.....	14
Table 6 Pugh Matrix for wing angle orientation.....	15
Table 7 Pugh Matrix for tail type design	16
Table 8 Pugh Matrix for number of jet engines	17
Table 9 Pugh Matrix for location of engines	18
Table 10 Pugh Matrix for number of crew	18
Table 11 Mission Fuel Fractions at each flight phase.....	21
Table 12 List of assumptions used in drag polar calculations	24
Table 13 Final converged lift and drag values.....	26
Table 14 Descriptions of variables in Eqns. 13-17.....	33
Table 15 Values for constraint equation during cruise	35
Table 16 Values for constraint equation during climb.....	36
Table 17 Values for constraint equation for service ceiling	37
Table 18 Values for constraint equation for takeoff run.....	38
Table 19 Values input into constrain equation for stall speed.....	39
Table 20 Values input into constrain equation for load factor.....	40
Table 21 Production and development cost categories.....	42
Table 22 Nicolai cost analysis	43
Table 23 Materials cost parameters	44
Table 24 Fuel cost parameters [15].....	45
Table 25 Officer base pay [17]	45
Table 26 Final hourly operation cost	45
Table 27 Convergence tolerances for optimization	48
Table 28 Design objective function results [4][5]	49
Table 29 Landing gear contact point locations	60
Table 30 Requirement compliance	60



Table 31 Assumed material values	66
Table 32 Final design parameters	70
Table 33 Historical wing data	71
Table 34 Wing numerical design	73
Table 35 Lifting surface ratios	75
Table 36 Parasite drag comparison	77
Table 37 Historical and calculated component weights [32]	80
Table 38 Empty center of gravity calculation	81
Table 39 System dynamic modes	88
Table 40 Dynamic mode requirements	88

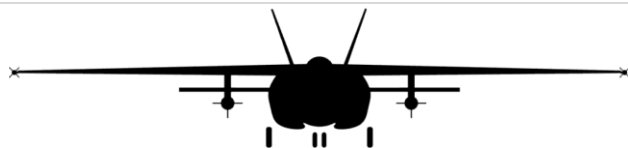


Fig. 1 Basic initial design of aircraft after configuration selection.....	19
Fig. 2 Requirement mission plan view	20
Fig. 3 Linear regression of current aircraft empty weights as function of takeoff weight [4][5].	23
Fig. 4 Plot of quadratic drag polar as calculated.....	25
Fig. 5 Combat radius' effect on takeoff weight.....	27
Fig. 6 Payload's effect on takeoff weight.....	28
Fig. 7 Varying cruise altitude at selected cruise speed	28
Fig. 8 Varying cruise altitude at selection cruise altitude.....	29
Fig. 9 Cruise design space contour plot	29
Fig. 10 Cruise design space carpet plot	30
Fig. 11 Varying loiter altitude at selected loiter speed	31
Fig. 12 Varying loiter speed at selected loiter altitude	31
Fig. 13 Loiter design space contour plot.....	32
Fig. 14 Loiter design space carpet plot	32
Fig. 15 Design point and constraint design space.....	34
Fig. 16 Cruise speed trade study.....	35
Fig. 17 Climb speed trade study	36
Fig. 18 Service ceiling trade study.....	37
Fig. 19 Takeoff run trade study.....	38
Fig. 20 Load factor trade study	40
Fig. 21 Optimized performance constraint space	41
Fig. 22 Wright cumulative learning curve [13]	44
Fig. 23 Optimization flow logic.....	47
Fig. 24 Aircraft dimensions	52
Fig. 25 Overhead x-ray view	53
Fig. 26 Rendered isometric image	53
Fig. 27 Engine installation [18]	55
Fig. 28 Conventional Rotary Launcher [19].....	55
Fig. 29 Weapons bay side cross-section [20].....	56
Fig. 30 Weapons bay front cross-section.....	57
Fig. 31 Forward guns	58



Fig. 32 Gun firing system [21].....	58
Fig. 33 Forward layout cross-section [21][22]	59
Fig. 34 Roskam tricycle landing gear requirements [23].....	60
Fig. 35 Main gear longitudinal angles	61
Fig. 36 Main gear retraction bay.....	61
Fig. 37 Structural overview.....	62
Fig. 38 Former cross-section.....	63
Fig. 39 Lower spar cap with general shape and dimensions.....	64
Fig. 40 Constant weight contour plot.....	67
Fig. 41 Constant cost contour plot	68
Fig. 42 Design loop.....	68
Fig. 43 Best obtained result [0/90/0].....	69
Fig. 44 Failure analysis outcome	69
Fig. 45 Wing thickness ratio selection chart [30]	72
Fig. 46 Selected airfoils [31].....	72
Fig. 47 Wing layout and structural dimensions	73
Fig. 48 Vertical stabilizer platform.....	74
Fig. 49 Horizontal stabilizer platform.....	74
Fig. 50 X-FOIL viscous data	76
Fig. 51 Second order drag polar.....	77
Fig. 52 VSP platform area	77
Fig. 53 Numerical lift to drag chart	78
Fig. 54 AVL lift results at cruise condition	78
Fig. 55 Trefftz plot at 15 degrees AOA	79
Fig. 56 AVL neutral point calculation	82
Fig. 57 Normalized chord locations.....	82
Fig. 58 CG excursion diagram	83
Fig. 59 AVL stability derivatives.....	85
Fig. 60 Decoupled linear state space model.....	86
Fig. 61 Longitudinal mode poles	87
Fig. 62 Lateral mode poles.....	87

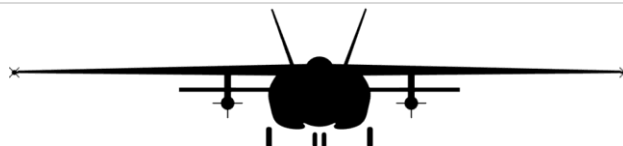


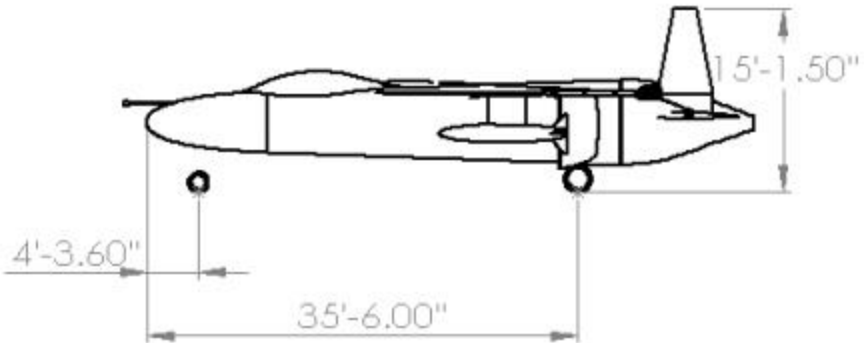
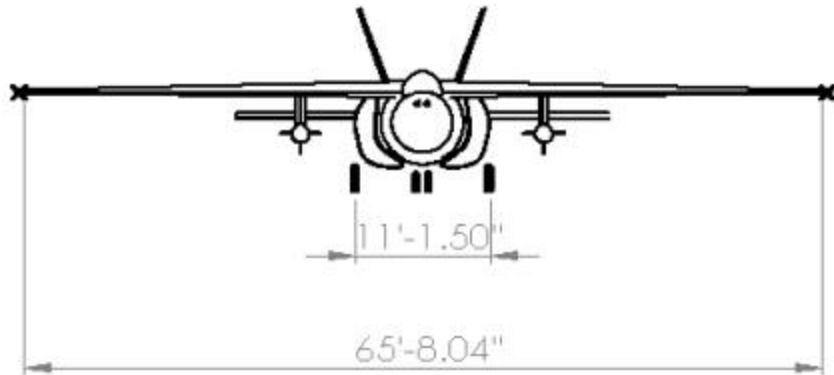
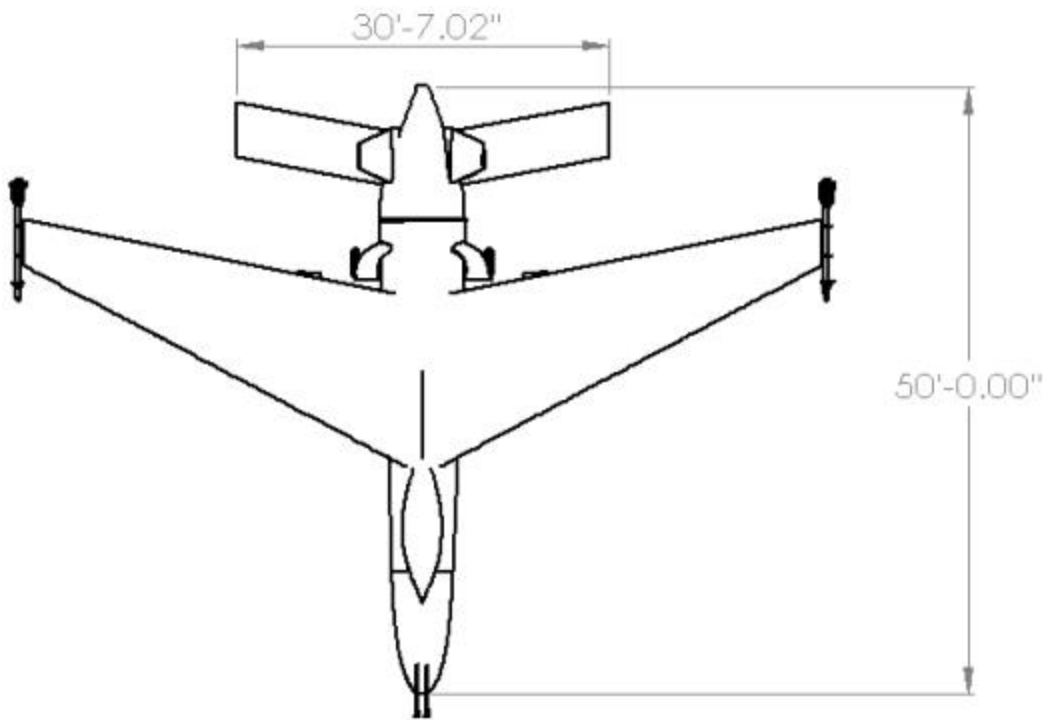
Part II: Executive Summary:

The Fairchild Republic A-10 Thunderbolt II, despite continuous admiration from the crew who flies her and the friendly ground forces protected by the Close Air Support (CAS) mission, grows older with each passing year. The airframe originally developed in the 1970's benefits from multiple upgrades and is fully mission capable, but decades of high operation tempo take their toll, and the weapons system nears the end of its service life. To prevent an interruption in capability, an innovative, realistic design to the following Request For Proposal (RFP) is submitted.

- 1-2 Crew
- AAO of 4 hours 500 nm from base
- 35 mm cannon lethal to armored vehicles
- Electro-optical targeting system
- Modern communications array
- Payload of 14000 lb of stores on at least 10 stations and 750 rounds of cannon ammunition
- Max Speed of at least 300 KTAS and Cruise Speed of at least 200 KTAS
- 45,000 ft ceiling
- Takeoff from 6000ft nonimproved runways at 5000ft elevation on a hot day
- Design load factor of 8 g
- MIL-SPEC compliant
- Entry date 2025

The most celebrated aspects of the A-10 remain her simplicity, ruggedness, and dedication to CAS. These axioms live on in the Colt, as sexy stealth and lofty multi-role promises take a back seat to cost effectiveness and a CAS first mindset. This, however, does not imply that innovation is abandoned. In the single seat, all weather jet, 10 total weapons stations exist with six residing internally with room for nearly any modern CAS ordnance to cut drag and lower signatures. Two 35 mm fixed cannons provide lethality to both hard and soft ground targets. State of the art sensing, targeting, electronic warfare, and battle space communication systems are included at launch. Responsible use of composites in unreparable areas balance performance with cost. The greatest innovation, however, proves the industry first powerplant. A single, next generation, high-bypass turbofan powers the design. The selected engine, a minimally modified, off the shelf operational powerplant, results not only in a mature supply train and reliable design, but structural weight savings and steep fuel savings. This especially results in much longer flight times possible without utilizing the aerial refueling capability. This cost-effective merging of innovation and traditional design results in the best initial proposal for a modern spiritual successor to the mighty A-10.





Part III: Stakeholder Analysis:

The background and RFP suggest a focus on a reliable, cheap, utility attack aircraft that excels in its role, CAS, championing simplicity and ease of maintenance in austere environments. The aircraft is interpreted by the RFP as an aircraft designed to operate in the current expected battlespace—asymmetric conflicts with little to no air resistance or after air-superiority has already been established. Advanced platforms capable of operating against technologically developed threats like Russia or China already exist at great cost. The main threats this aircraft would face include groundfire or AA armaments common in the proxy and guerrilla wars America has exclusively participated in from the early 1970's. Survivability of these threats at the necessary low-levels required for CAS is a must. Similar to how the A-10 was built to defeat Russia's expansive armor inventory if the Cold War ever came to broil, this aircraft will be designed to defeat infantry ground forces and insurgents as the modern enemy.

The design philosophy intends to buck the trend of increasing complexity, cost, and size seen in the modern fighter world in examples such as the F-111, F-15, and F-22. Instead, the intention is to retrace the F-5/F-20 approach of decreasing size and cost as a light attack platform and prove Mr. Augustine wrong. Exotic traits such as high speeds, stealth, and complex manufacturing processes will be abandoned to maximize loiter time, payload, economy, and survivability.

The payload, flight time, and weapon integration are projected to prove some of the greatest measures of effectiveness from the requirements. For example, from the RFP, 35 mm is an impressive gun caliber for an airborne system. The famed system in the A-10 strikes fear at 30 mm. One of the few current autocannons of this caliber is the German Rheinmetall 35 mm x 228 KDG, and integrating the space for the ammunition and all other stores will be a challenge, but at its core the system must put warfighting as its thesis.

Determining measures of effectiveness important to the stakeholder often involves one of the most difficult portions of developing an original aircraft, as often the stakeholders might not know exactly what they desire. The military excels at this. Although thousands of pages of requirements exist, mission creep and over aggressive cost promises at times push programs to oblivion. To the credit of the RFP, seven performance measures are identified as critical to quantifying the effectiveness of the proposed design: Range with Loitering, Dash Speed, Cruise Speed, Fly-Away Cost, Operating Cost, Takeoff Length, and Positive Load Factor.

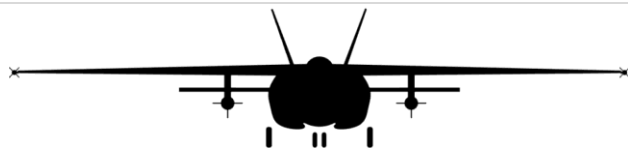


These performance measures are normalized by a baseline performance, and the designer still determines the weightings by interpreting the stakeholders and baseline, but these qualifiers still hint what is valued by the stakeholders. The weightings selected for the design are listed below in Table 1.

Table 1 Stakeholder weightings

Factor:	Range	Dash Speed	Cruise Speed	Fly-Away Cost	Direct Operating Cost	Takeoff Length	Max Load Factor
Weight:	0.20	0.10	0.10	0.25	0.20	0.10	0.05

The penultimate factor chosen stands as fly-away cost, or the accession cost per unit. One of the greatest challenges to initiate a program in the current political climate becomes convincing Congress that a need exists and the program will provide maximum value to the taxpayer. Despite the current uptick in military spending [1], the most advanced performance in the world is useless if it cannot find funding. In a similar vein, direct operating cost, or the expected cumulative cost per flight hour, trails directly behind, as the total lifetime program cost and yearly percentage of the defense budget play just as large in the public’s collective conscience. Upper leadership understand that any single program holds a responsibility to not adversely affect mission effectiveness of other projects for a single new capability. For this weighting, the chosen most important direct performance measure reigns range. This is because range not only corresponds to distance available to potential targets, but also total flight time. A commercial jet requires the ability to fly far, but military outside of cargo usually requires the ability to fly for long periods of time. Even utilizing aerial refueling, each minute dedicated to refueling or after the aircraft must Return To Base is a minute out of the fight, and engagements are entirely unpredictable. Dash speed, cruise speed, and takeoff length are all weighted lower, as although they are performance metrics, they less directly dictate mission effectiveness, and are considered more ‘nice to have’ performance. Dash speed and cruise speed only come more strongly into effect on long distance flights. All Air Force bases in major areas of focus for international security like USCENTCOM or PACAF feature well developed, long runways where maximum performance takeoffs are not required. Operations from unimproved or improvised locations are also rare. Load factor is ranked the lowest, as maneuverability in a heavy attack plane takes a back seat to total endurance and payload, and it sharply siphons these abilities. From a cost saving standpoint and the projected expectation of air superiority, low observability is not directly considered as a design goal.



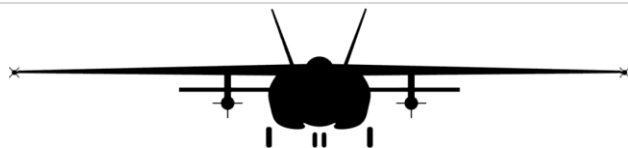
Part IV: Configuration Selection:

The first step towards a viable design of this aircraft is the configuration selection for the general shape of the aircraft, which is accomplished through Pugh Matrices. Table 2 lists each component evaluated by Pugh Matrices. The weightings are based upon the maximizing coefficients discussed prior. In order to minimize unrealistic designs, a maximum of five alternatives are discussed for each component.

Table 2 Selected components for initial configuration aircraft

Components	Alternatives				
Wing Layout	Tandem	Canard	Three Surface	Conventional	Flying Wing
Wing Attachment	High Wing	Mid-Wing	Low Wing	-	-
Wing Shape	Delta	Conventional	Multi-Wing	-	-
Wing Angle	Dihedral	Flat	Cathedral	-	-
Tail Type	Duel	Conventional	T-Tail	H-Tail	Cruciform
Number of Engines	One	Two	-	-	-
Engine Location	On Fuselage	Fuselage internal	-	-	-
Crew Number	One	Two	-	-	-

The first component in the configuration selection is the wing layout of the aircraft. The five alternatives used are a tandem wing, canard, three surface wings, conventional, and flying wing. Table 3 shows the Pugh Matrix for the wing layout selection. The Figures of Merit (FOM) for the general shape are manufacturing, control complexity, speed/acceleration, weight, and maneuverability. At discretion, values for each FOM are assigned based on the perceived merit of each component. The FOMs are weighted by a value range from 1-5, with 1 being low on the priority list, and 5 being one of the most valuable FOM's taken into consideration. Each option in the Pugh Matrix is graded under each FOM from a scale of 1-5, 1 being the lowest and 5 the highest. Once each option is graded, each score is multiplied by the FOM's corresponding weight value; then each score is summed at the bottom of the matrix. The option with the highest score is



selected as that component for the configuration selection. The two highest-weighted FOM's are manufacturing/maneuverability and weight for the wing layout component. The structural complexity is defined as the difficulty required of integrating the wing to the fuselage. The control complexity is how the lifting surfaces affect each other aerodynamically and the analysis necessary to provide stable control. Since the aircraft will need to be a stable aerodynamic platform with low weight, speed is generally a low concern. The conventional wing layout is selected for the design.

Table 3 Pugh Matrix for configuration selection

		Wing Layout				
FOM	Weight	Tandem	Canard	Three Surface	Conventional	Flying Wing
Manufacturing	4	2	3	1	5	1
Control Complexity	3	3	2	2	4	1
Speed/Acceleration	2	2	4	3	3	2
Weight	5	2	4	2	5	3
Maneuverability	4	3	3	4	4	2
Total	18	43	58	42	79	34

The wing attachment Pugh Matrix, shown in Table 4, has three alternatives: high-wing, mid-wing, and low-wing. The FOM's are fuselage interference, ground clearance, maneuverability, stability, and aesthetic appeal. Fuselage interference refers to the projected difficulties integrating systems with respect to potential interference from the wing position. Ground clearance describes the space between the wing and the ground for external stores. Maneuverability is the wing's ability to perform any maneuver. Aesthetic appeal regards how the stakeholders and passengers might think the aircraft looks, a topic worth giving at least a small consideration in light of the X-32. Ground clearance owns a high priority in the assessment of the wing attachment because of the type of stores available to use, including external fuel tanks, as well as to ease the loading for armament crews. The high-wing attachment is selected for the aircraft because the wing structure will avoid interfering with large systems in the center of the aircraft. High-wings also provide excellent ground clearance for stores and improve Foreign



Object Debris (FOD) resilience at unimproved forward landing strips. Additionally, the high-wing arrangement will naturally supply a level of lateral stability.

Table 4 Pugh Matrix for wing attachment

		Wing Attachment		
FOM	Weight	High-Wing	Mid-Wing	Low-Wing
Fuselage Interference	3	5	2	4
Ground Clearance	4	5	4	1
Maneuverability	4	2	4	5
Stability	3	4	3	2
Aesthetic Appeal	1	2	3	4
Total	18	57	53	46

The wing shape is the next component in the Configuration Selection process. Table 5 shows the FOMs and alternatives used for the evaluation of the wing shape. The three alternatives in the Pugh Matrix are a delta wing, conventional wing, and a multi-wing. The FOMs are manufacturing, speed capability, lift, and fuel storage. While the delta wing has the best speed capability and fuel storage capability, the conventional wing has improved manufacturing characteristics (in that the conventional wing is less complex and less expensive to build) and lift (the conventional wing produces more lift over the design envelope with less drag). The only positive attribute the multi-wing shape possesses is exceptional fuel storage. The conventional wing shape is selected for the aircraft.

Table 5 Pugh Matrix for wing shape

		Wing Shape		
FOM	Weight	Delta	Conventional	Multi-Wing
Manufacturing	4	2	4	1
Speed Capability	3	5	4	3
Lift	5	2	4	3
Fuel Storage	4	5	3	5
Total	16	53	60	48



The wing angle is defined as the orientation of the wing with respect to the y-axis of the aircraft. This is analyzed using the matrix shown in Table 6. The angles evaluated are dihedral, flat, and cathedral (anhedral), while the FOM's are stability, aesthetic appeal, and again ground clearance. Stability is how much the wing angle could contribute to flight characteristics at certain flight profiles. The overall ground clearance of the wing angle with consideration to wing attachment is the most-weighted FOM, from previous considerations. While the dihedral option has the most stability enhancement, the flat wing angle is chosen for its interaction with the high wing selection. Dihedral combined with a high-wing may increase lateral stability to the point of low maneuverability, as well as lowering certain aesthetics.

Table 6 Pugh Matrix for wing angle orientation

		Wing Angle		
FOM	Weight	Dihedral	Flat	Cathedral
Stability	3	4	3	1
Aesthetic Appeal	1	3	4	4
Ground Clearance	4	3	4	4
Total	8	27	29	23

The next component for the configuration selection is the tail type for the aircraft. Table 7 shows the corresponding Pugh Matrix for the tail type with the alternatives analyzed being dual, conventional, T-Tail, H-Tail, and cruciform. The main FOMs for the tail design Pugh Matrix are manufacturing, control complexity, redundancy, weight, and drag. Redundancy is the extent to which a pilot of the aircraft can maintain control after a portion of the tail is either damaged or broken off in flight. Drag is how relative form, parasitic, and interference drag is expected from the horizontal and vertical stabilizers. Control complexity is how difficult it is for aircraft to maintain stable flight with respect to the tail configuration. Three tail types rank close to one another for the design choice: conventional tail, T-Tail, and cruciform tail. The T-Tail finds the best rating for jet wash, being that the stream produced by the engines does not come into contact with the horizontal stabilizers. The highest rated FOM is redundancy to increase survivability from enemy fire. The conventional tail has improved manufacturing simplicity and weight over the T-Tail, however, the conventional tail is rated low on the redundancy FOM. While the H-Tail



configuration of the A-10 performs very similarly to the dual tails, the added structure and complexity of the control surfaces placed on the horizontal stabilizer makes it a less desirable choice. In the end, the dual tail is chosen as the design, based on overall satisfactory scores across all FOMs and high marks for redundancy.

Table 7 Pugh Matrix for tail type design

		Tail Type				
FOM	Weight	Dual	Conventional	T-Tail	H-Tail	Cruciform
Manufacturing	4	3	4	3	2	4
Control Complexity	3	3	4	3	3	4
Redundancy	5	5	2	2	5	2
Weight	3	3	4	3	3	4
Drag	2	3	4	4	2	3
Total	17	61	59	48	55	56

The number of jet engines is the next configuration selection conducted, shown in Table 8. The FOMs for the engine number Pugh Matrix are power, weight, and redundancy; as before, redundancy is how much control the pilot has when the engine or one of the engines of the aircraft is disabled. Power is the relative thrust produced by the engines to keep the aircraft in the air. Because of the desired small size, simplicity and range, weight and fuel consumption are the highest rated FOMs. Overall, a single engine is selected for the aircraft, mainly because it is expected that modern high-bypass turbofans will produce similar levels of thrust at significant fuel savings compared to earlier generations of turbojets. This allows for increased range and loiter time. While this could lower survivability and redundancy, because of the selected engine integration in the next Pugh Matrix, damage taken that could disable one engine is assumed to also damage the other engine because of proximity.

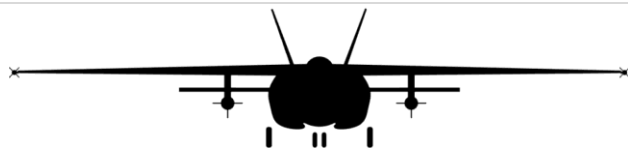


Table 8 Pugh Matrix for number of jet engines

FOM	Weight	Number of Engines	
		One	Two
Power	3	3	5
Weight	5	5	2
Redundancy	4	2	4
Fuel Consumption	4	4	2
Total	16	58	49

The next selection Pugh Matrix is the for the location of the engines. As the previous Pugh Matrix determined the number of engines to be one, the possible locations of the engines correspond with this design choice. This eliminates symmetric placements such as wing pylons. Table 9 shows the Pugh Matrix for the engine placement. The two possible locations selected for evaluation are on the fuselage, and built into the fuselage itself. The FOMs from Table 9 are the drag produced by the engine location, fuel storage, and maintenance of the aircraft. The fuel storage is how much the wings could store fuel in correlation to the location of the engines. The maintenance FOM is how difficult it would be for maintainers to access and repair the engines on the aircraft; this corresponds to how expensive engine repairs would be. Maintenance difficulties attributed to engine repair or replacement is the highest-weighted FOM, as maintenance time per flight hour directly affects mission readiness. After evaluation, the engines are chosen to be built into the fuselage. While internal fuel storage is reduced from the engine and associated inlet ducting, the drag reduction of a non-pyloned internal engine is substantial. Placing the line-of-thrust along the longitudinal axis will also improve control.



Table 9 Pugh Matrix for location of engines

		Engine Location	
FOM	Weight	On Fuselage	Fuselage Internal
Drag	3	1	5
Fuel Storage	4	4	2
Maintenance	4	2	3
Total	11	27	35

The final selection Pugh Matrix includes the total number of crew. Work load is defined as relative stress on the pilots from both flying the aircraft and handling navigation, communication, and target identification. Weight and cockpit integration both measure the effects on performance and disruption of the simplest fuselage design because of crew areas. Weight and cockpit integration are the highest weighted FOM's. Table 10 shows the Pugh Matrix for the crew, where a single pilot is selected for the aircraft. While a Combat System Officer (CSO, Air Force), would split and reduce crew work load, all necessary equipment to accommodate the second crewmember would reduce payload, internal volume available, and increase complexity. Modern advances in cognitive engineering, the demonstrated effectiveness of a single pilot in platforms such as the F-16, F-22, F-35, and matching this mission set, the A-10, prove a single skilled pilot more than capable of managing all operations of modern war-fighting jets.

Table 10 Pugh Matrix for number of crew

		Number of Crew	
FOM	Weight	One	Two
Work Load	3	2	5
Weight	5	4	2
Cockpit Integration	4	5	1
Total	12	46	29

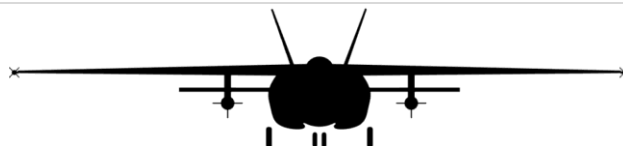


Figure 1 shows an initial sketch of the aircraft layout after configuration selection as produced in Vehicle Sketch Pad (VSP).

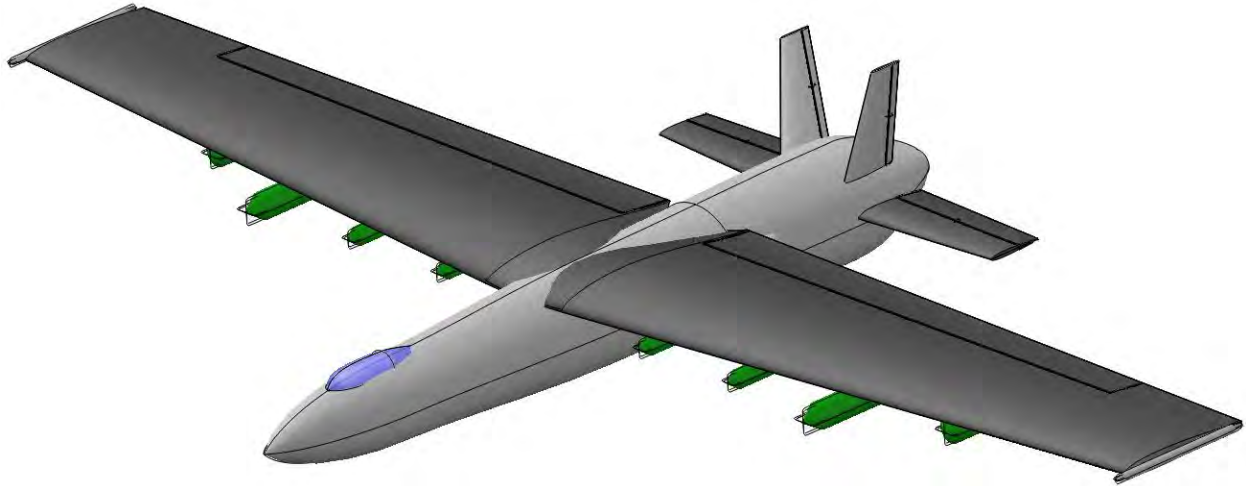
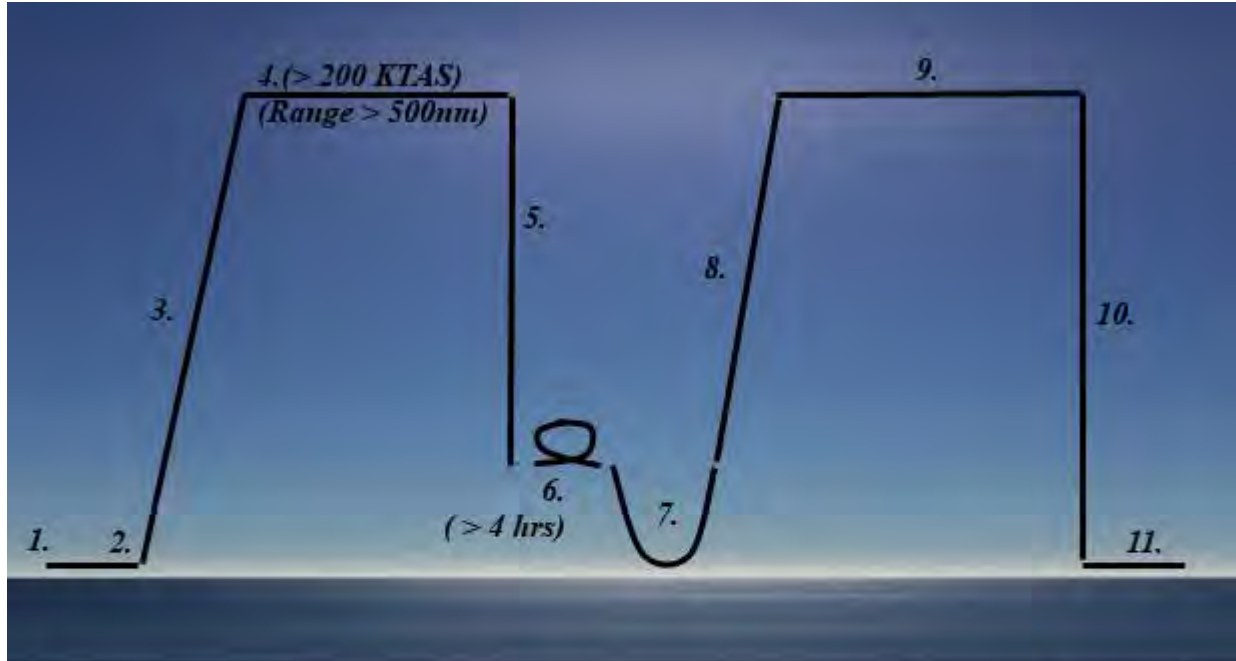


Fig. 1 Basic initial design of aircraft after configuration selection



Part V: Mission Overview

The following mission modeled is the design mission, or what is considered to act as the baseline typical mission based on multiple requirements as listed in the RFP. The mission breaks down into 11 distinct flight phases where performance and design points are tailored to meet this minimum mission. Below Fig. 2 provides a plan view of the modeled mission.



- 1. Start/Taxi
- 2. Takeoff
- 3. Climb
- 4. Cruise Out

- 5. Descent 1
- 6. Loiter
- 7. Attack

- 8. Climb 2
- 9. Cruise Back
- 10. Descent 2
- 11. Land/Taxi

Fig. 2 Requirement mission plan view

This outlines the minimum mission. Cruise speed must be at least 200 KTAS to a combat area no less than 500 nm away from the home base where the maximum performance takeoff with full combat load must be completed within 6000 ft of runway at an elevation of 5000 ft on a hot day. This, however, only outlines minimum performance, and a full analysis of potential performance, trade studies, and a mission optimization will be performed to explore where designing to greater performance proves cost effective and justified relative to the tradeoffs and opportunity cost propagating as second and third order effects from these changes.



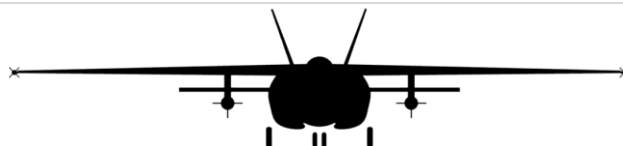
Part VI: Weight Sizing

The overall purpose of the weight sizing is to determine the mission takeoff weight for an aircraft given specific flight phases and empty weight calculated from a weight regression of similar aircraft. The different flight phases essentially impact the fuel weight required to complete the full mission. The fuel that is consumed in each mission phase is quantified by a fuel fraction; this is defined as the ratio of the weight at the end of the mission phase to the weight at the beginning of the mission phase. *Roskam Part I* [2] provides the information for fuel fractions, and the calculated values are contained in Table 11. The Mission Fuel Fraction (M_{ff}) for start, taxi, takeoff, descents, and landing are assumed to equal 0.99 [2].

Table 11 Mission Fuel Fractions at each flight phase

Phase	M_{ff}
Start	0.9900
Taxi	0.9900
Takeoff	0.9900
Climb	0.9928
Cruise Out	0.9330
Descent 1	0.9900
Loiter	0.8890
Attack	0.9922
Climb 2	0.9922
Cruise Back	0.9261
Descent 2	0.9900
Land/Taxi	0.9900

The Mission Fuel Fraction values for the climb and cruise are found through analyses of the endurance and range for climb and range respectively. The Mission Fuel Fractions during a specific time period (climb, loiter, and attack) are found with Eqn. 1.



$$M_{ff} = e^{-\frac{E(TSFC)}{\left(\frac{L}{D}\right)}} \quad (1)$$

The variable E is the time elapsed during the climb or segment, TSFC is the Thrust Specific Fuel Consumption of the engine at the climb point, and L/D is the lift to drag ratio for the climb.

Climb is modeled using the endurance of the segment, and the climb requirement is primarily determined by the climb gradient. This gradient is defined as a ratio of the ground distance covered to the altitude climbed as a percentage. The climb is assumed at a rate of 1000 fpm or a gradient of 3.9 percent and at 250kts, and is carried out between sea level and the cruise altitude, 15,000 ft (as determined by the next section). The time to cruise using these values for climb rate and cruise altitude is found to be 15 minutes. The TSFC and thrust at each flight stage is curve fit to engine deck data [3] based on Mach number, altitude, and power setting for the CFM International CFM56 turbofan engine. This allows the fuel consumption and thrust to faithfully change at each speed and altitude based on actual data. The values for TSFC during climb and cruise are assumed to be the same 0.442 and 0.470 lb/lb/hr using this methodology. The lift to drag ratio is iteratively determined for the weight sizing process, and this will be discussed further in the aerodynamic section of the report.

During cruise, the process is similar but for one key difference. The cruise Mission Fuel Fraction is determined not by endurance, but by the combat range (R) and velocity (V) associated with cruise. Eqn. 2 below gives the mission fuel fraction during cruise.

$$M_{ff} = e^{-\frac{R(TSFC)}{V\left(\frac{L}{D}\right)}} \quad (2)$$

The initial weight sizing utilizes the requirement metrics, but both the combat range of the aircraft and the optimal cruise velocity are increased to maximize the objective function as discussed in a later section.

The Fission Fuel Fraction is determined by multiplying the fuel fractions for each mission phase. This will provide the amount of fuel used over the course of a nominal mission (startup to taxi/landing). The Mission Fuel Fraction is found to be 0.7107 for the final objective function optimized mission. The value for fuel fraction can then be translated into a fuel weight through Eqn. 3.



$$W_F = \frac{(1 - M_{ff})W_{TO}}{1 - M_{ff,tfo}} \quad (3)$$

The trapped fuel and oil will account for 0.5 percent of the total fuel weight, or an $M_{ff,tfo}$ of 0.005, where $M_{ff,tfo}$ is the fuel fraction of the trapped fuel and oil that remains after normal operations. The empty weight for the mission is found through Eqn. 4.

$$W_E = W_{TO} - W_{CREW} - W_{PAYLOAD} - W_F - W_{TFO} \quad (4)$$

The payload weight is determined based on the requirement of 14,000 lb total of stores and the estimated crew weight of 160 lb per *Roskam Part I* [2]. The takeoff weight is estimated at a value, and this value for takeoff weight is modified to obtain the correct empty weight.

The actual empty weight is calculated through a linear regression relationship between similar aircraft. The values are compiled into a log-log plot of takeoff weight to empty weight. The linear fit coefficients for this log-log plot are modified to match the form shown in Eqn. 5 where η is a projected weight saving factor using projected technologies to be calculated in a later section.

$$\log(W_E) = \frac{1}{B} [\log(W_{TO}) - (A - B \log_{10} \eta)] \quad (5)$$

Fig. 3 provides the linear fit performed for similar modern aircraft takeoff and empty weights [4][5].

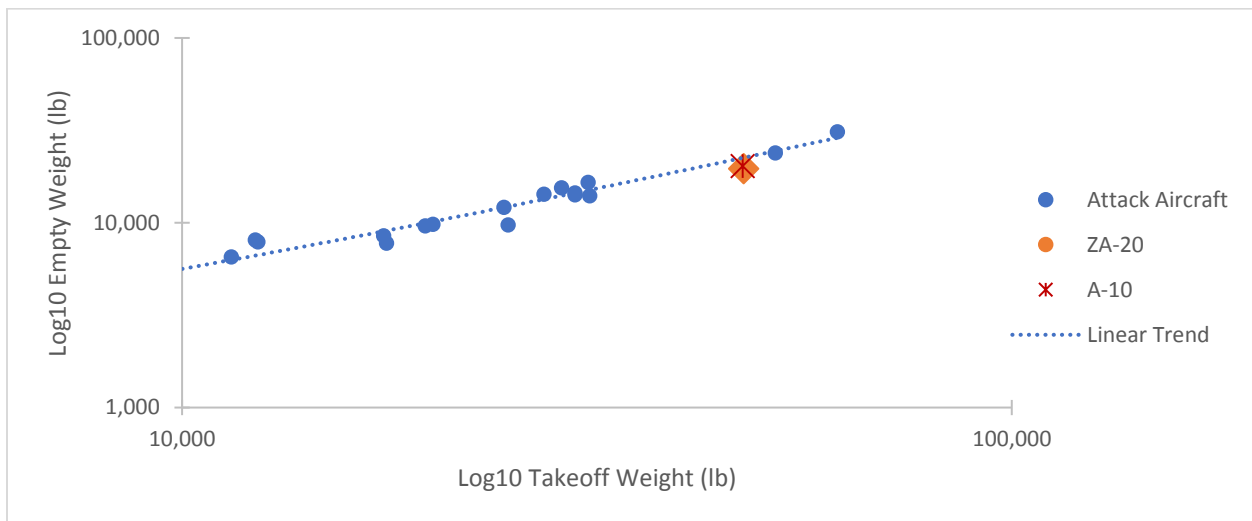
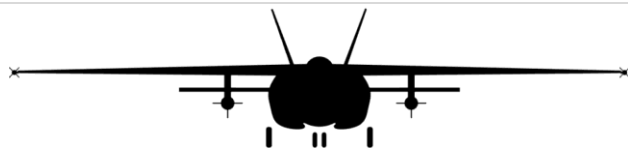


Fig. 3 Linear regression of current aircraft empty weights as function of takeoff weight [4][5]



The final values for A and B are determined to be -0.1667 and 1.1287, respectively. The assumed value for takeoff weight is input into Eqn. 5 and the empty weight is calculated. As part of the iterative optimization scheme to be discussed, the assumed takeoff weight is iteratively modified to converge the empty weight calculations from Eqn. 4 and Eqn. 5.

The lift to drag ratio utilized in the weight sizing procedure is calculated iteratively at each stage of flight to calculate each Mission Fuel Fraction. This is done using a quadratic drag polar, and there are a number of assumptions that are used in this calculation. Table 12 lists the assumptions used in the drag polar calculations.

Table 12 List of assumptions used in drag polar calculations

Variable	Value
c	0.8565
d	0.5423
Takeoff Weight (W_{TO})	47,500 lb
Wing Loading	80 psf
Skin Friction Coefficient (C_f)	0.0045
Oswald's Efficiency Factor (e)	0.839
Aspect Ratio (AR)	7.0
Wetted Area (S_{wet})	2,471 ft ²
Wing Surface Area	594 ft ²
Parasite Drag Coefficient ($C_{D,0}$)	0.0187
Quadratic Coefficient (K)	0.0542

The c and d parameters are linear regression coefficients that are obtained through empirical data from similar aircraft [2]. These can be used to determine the wetted area, S_{wet} , using the takeoff weight of the aircraft. Equation 6 provides the relationship between the takeoff weight and wetted area.

$$\log(S_{wet}) = c + d \log(W_{TO}) \quad (6)$$

The current assumption for the takeoff weight from the weight sizing is used to determine the wetted area of the wing. The chosen wing loading is a result of the constraint analysis that is detailed later in this report. The skin friction coefficient is determined from *Roskam Part I* [2] that provides a figure showing that comparable jet aircraft have equivalent skin friction around 0.0045.



Oswald's Efficiency Factor, e , for this aircraft is determined using Eqn. 7 where AR is the aspect ratio of the wing [6].

$$e = 1.78(1 - 0.045 AR^{0.68}) - 0.64 \quad (7)$$

The parasite drag coefficient, $C_{D,0}$, is computed using Eqn. 8 [2].

$$C_{D,0} = \frac{c_f S_{wet}}{S} \quad (8)$$

This value for $C_{D,0}$ is constant for the aircraft no matter the flight phase, so it carries throughout this analysis process. The quadratic coefficient (K) is used to simplify the equation for the quadratic drag polar, as calculated through Eqn. 9 below.

$$K = \frac{1}{\pi A e} \quad (9)$$

These values are all used to determine the quadratic drag polar. Equation 10 provides this relationship between lift and drag, and Fig. 4 depicts this equation for the values given in Table 12 as the drag polar.

$$C_D = C_{D,0} + K(C_L)^2 \quad (10)$$

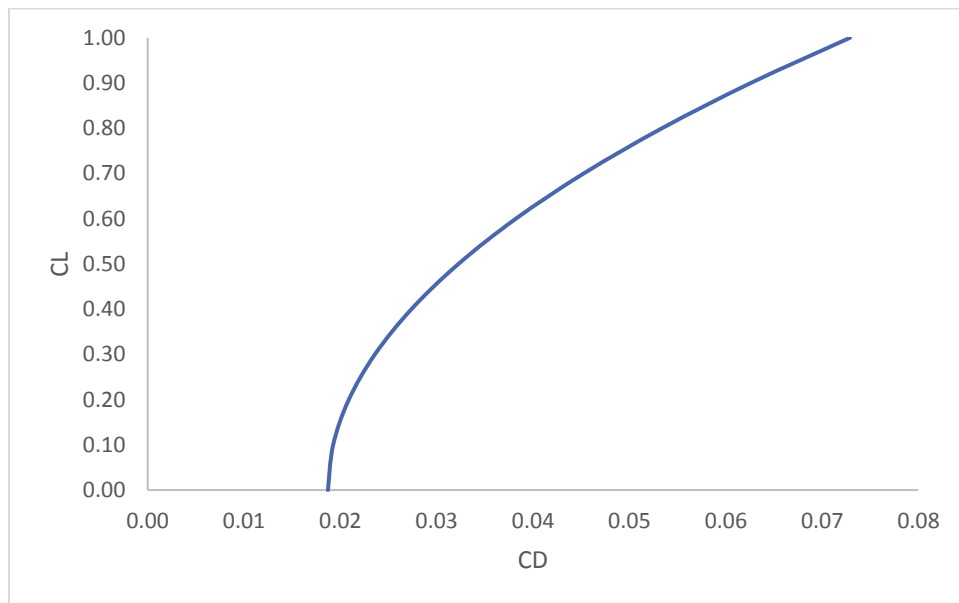


Fig. 4 Plot of quadratic drag polar as calculated



The next step to determine the lift to drag ratio for the different mission phases is to calculate the lift coefficient at the specific mission phases. For this procedure the lift to drag ratio at each segment is considered. The air density is found using the Standard Atmosphere in slugs/ft³ with an altitude input of feet with Eqn. 11. The coefficient of lift is found through Eqn.12:

$$\rho = (6.62724 * 10^{-15}) \left(518.7 - 0.00356 * \frac{A}{2} \right)^{4.256} \quad (11)$$

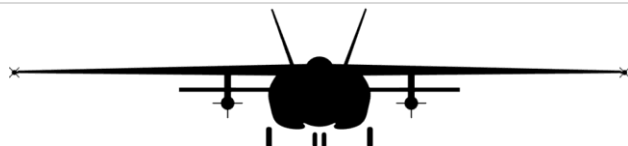
$$C_L = \frac{2W}{\rho V^2 S} \quad (12)$$

This equation is true given the assumption that lift is approximately equal to weight in steady constant speed flight. The weight at each segment, W, is determined by the Mission Fuel Fractions. The value obtained for lift is input into Eqn. 10 to obtain the drag, and dividing the drag from the lift will provide the lift to drag ratio.

This process is complete when the takeoff and empty weights, drag polar, and other factors converge via the optimization scheme to be discussed. The final values for lift and drag at each flight segment are listed in Table 13. Because the Mission Fuel Fraction of descents are assumed, they are not calculated.

Table 13 Final converged lift and drag values

Segment	Altitude (ft)	Velocity (kts)	Weight (lb)	C _L	Induced Drag (K C _L ²)	Lift to Drag Ratio
Climb 1	7,500	250	46,126	0.4577	0.0114	15.2245
Cruise 1	15,000	300	45,793	0.3881	0.0082	14.4423
Loiter	5,000	200	42,300	0.3687	0.0074	14.1828
Attack	5,000	300	37,605	0.2410	0.0031	11.0241
Climb 2	300	200	37,438	0.3714	0.0075	14.1828
Cruise 2	15,000	270	37,147	0.3137	0.0053	13.0475



Part VII: Weight Sizing Sensitivity Studies

Although a set mission is already defined in the RFP, the actual design point in terms of expected selected altitude and speeds for loiter and cruise must be selected based on stakeholder analysis and sensitivity studies. Although this analysis is completed early in the design iteration before expected takeoff weights are finalized, it still provides insight to how the final mission given in Table 13 is selected. Typical operations of A-10 missions are looked at as a starting point, and the performance of the aircraft at various flight conditions are compared to find an optimized design point to use as constant in the cost function analysis.

First are the effects of desired aircraft performance. These relationships are given in Fig. 5 and Fig. 6. As expected, both of these parameters simply linearly increase takeoff weight. Finding the optimal cost versus benefit point of these two variables becomes a major objective of cost function optimization scheme analysis.

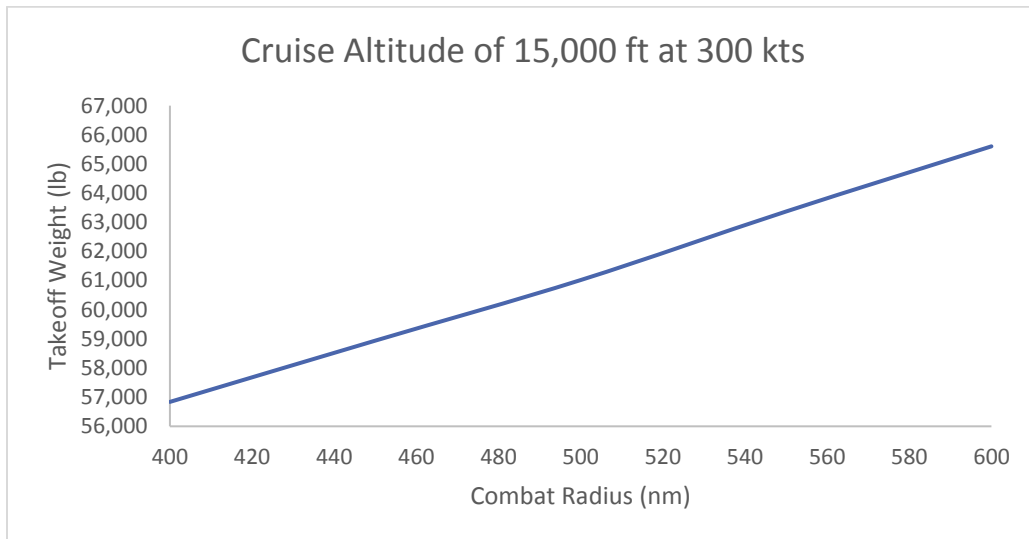


Fig. 5 Combat radius' effect on takeoff weight



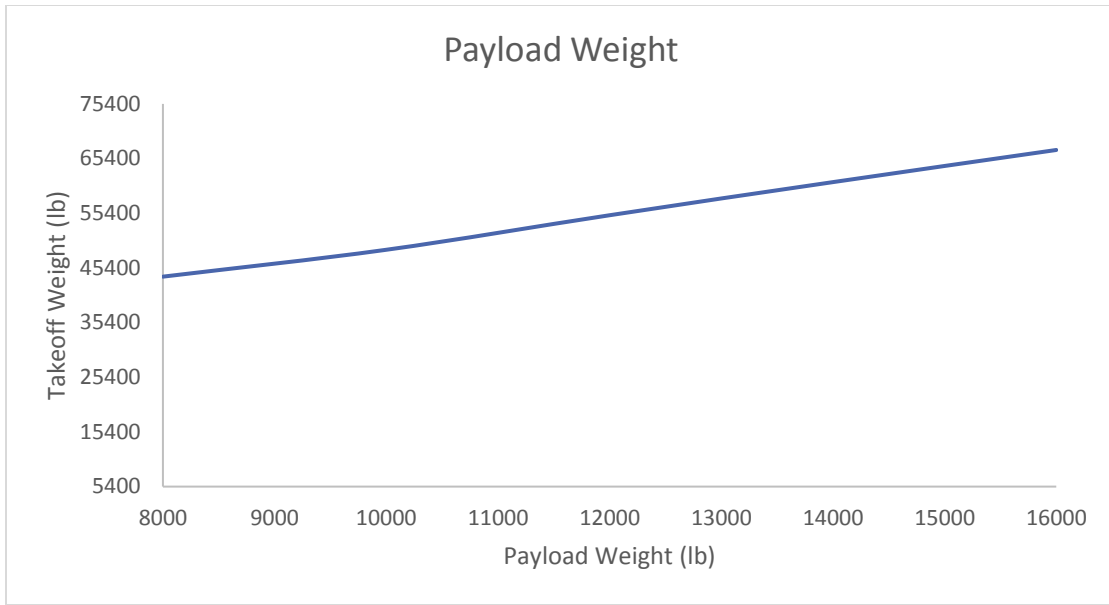


Fig. 6 Payload's effect on takeoff weight

For the cruise condition, a visualization of the trends can be taken by taking a snapshot slice. Below, the two trend lines comparing cruise speed and cruise altitude to final takeoff weight at the selected points are demonstrated in Fig. 7 and Fig. 8.

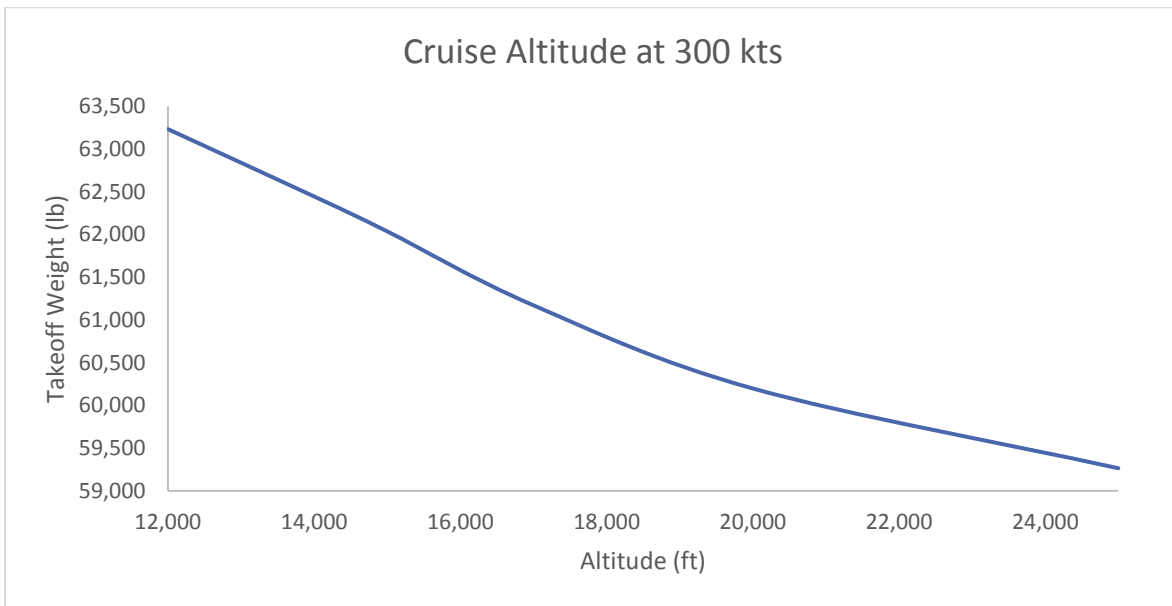
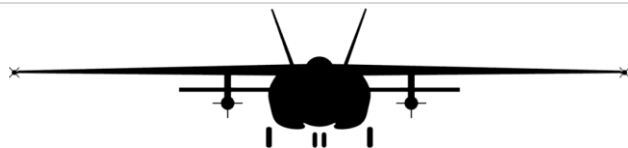


Fig. 7 Varying cruise altitude at selected cruise speed



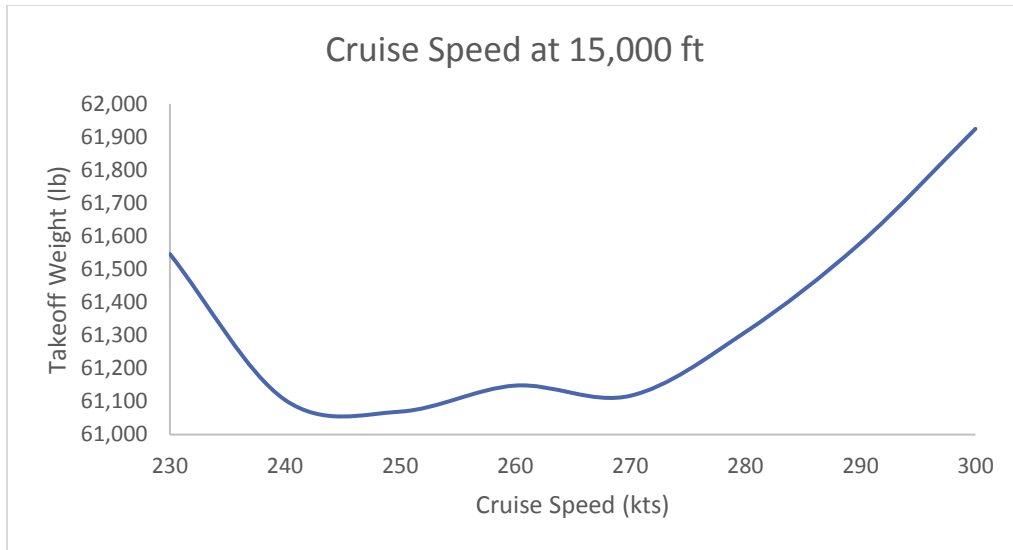


Fig. 8 Varying cruise altitude at selection cruise altitude

From these two figures, there seems to be a marked benefit in terms of fuel savings and hence final takeoff weight with increasing cruise altitude. At a particular altitude, there also exists a sweet spot in efficient cruise speed. Combining these two design spaces to be compared at once, Fig. 9 and Fig. 10 are extrapolated.

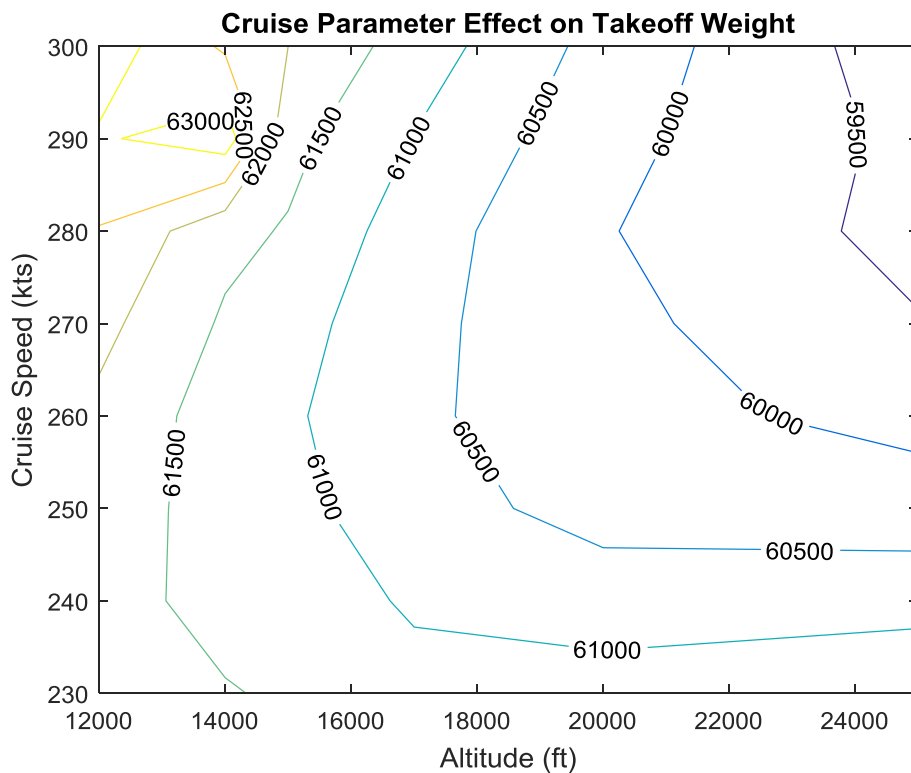


Fig. 9 Cruise design space contour plot



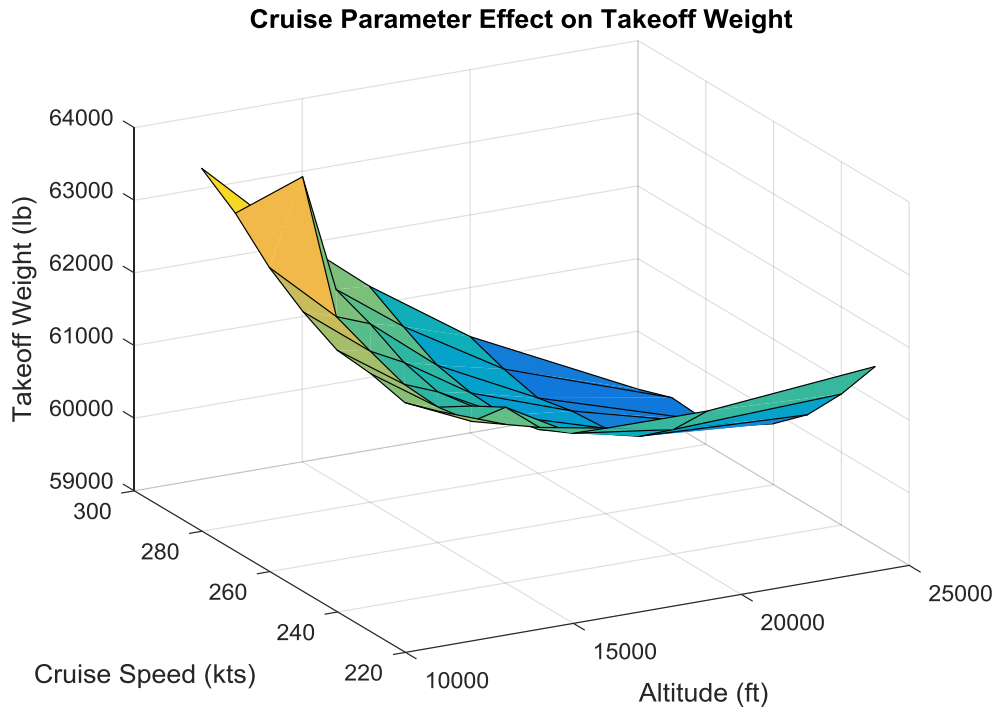


Fig. 10 Cruise design space carpet plot

As especially demonstrated in Fig. 10, for each chosen cruise altitude, there exists a cruise speed that minimizes the cost to takeoff weight. However, the objective function values cruise speed, not cruise altitude. This leaves cruise altitude up to stakeholder analysis. A lower cruise altitude is selected to allow quick engagements with ground forces and minimize time spent descending to an attack altitude. If the aircraft is ferried to a faraway location, a higher altitude is recommended. Also, to be demonstrated in the optimization scheme analysis, a quicker cruise speed is found to be justified by the objective function despite the increase in takeoff weight.

For the selected loiter conditions, the same analysis is completed with the results listed in Fig. 11 through Fig. 13.



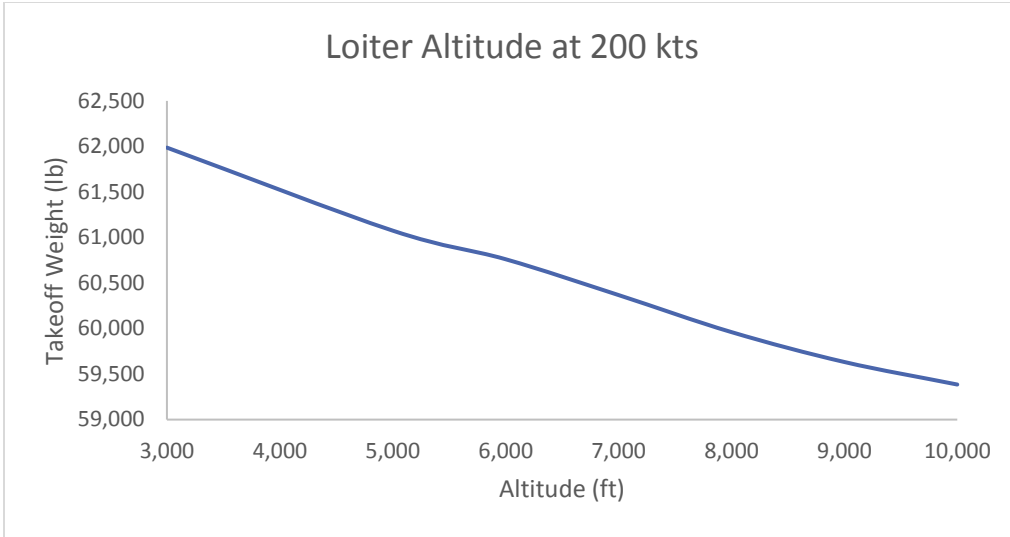


Fig. 11 Varying loiter altitude at selected loiter speed

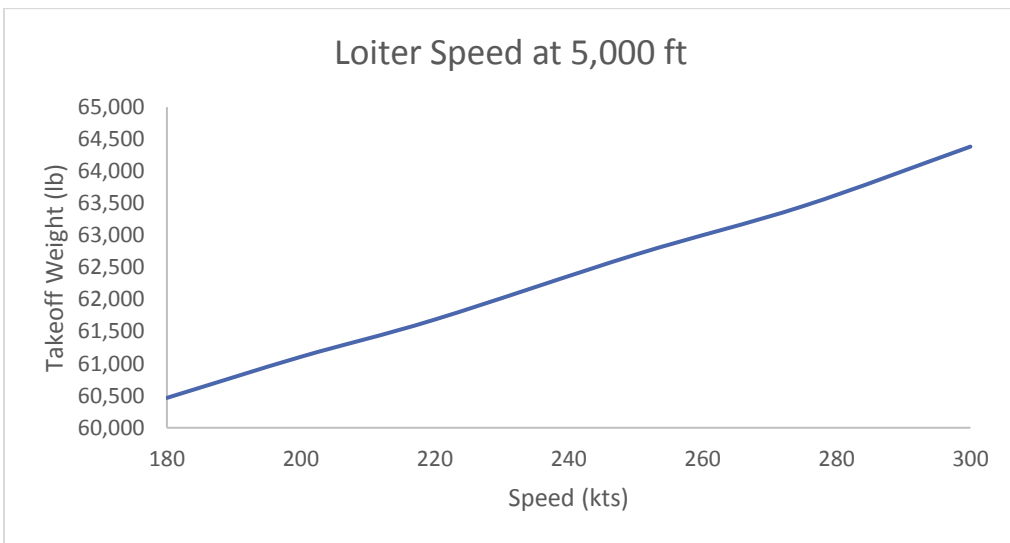
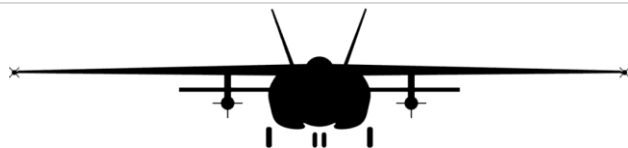


Fig. 12 Varying loiter speed at selected loiter altitude



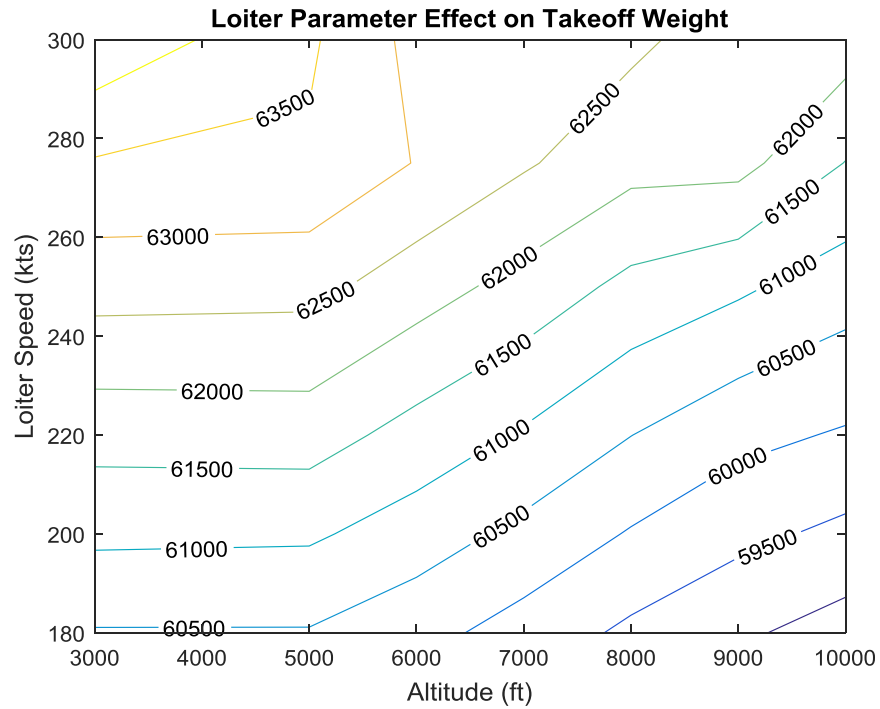


Fig. 13 Loiter design space contour plot

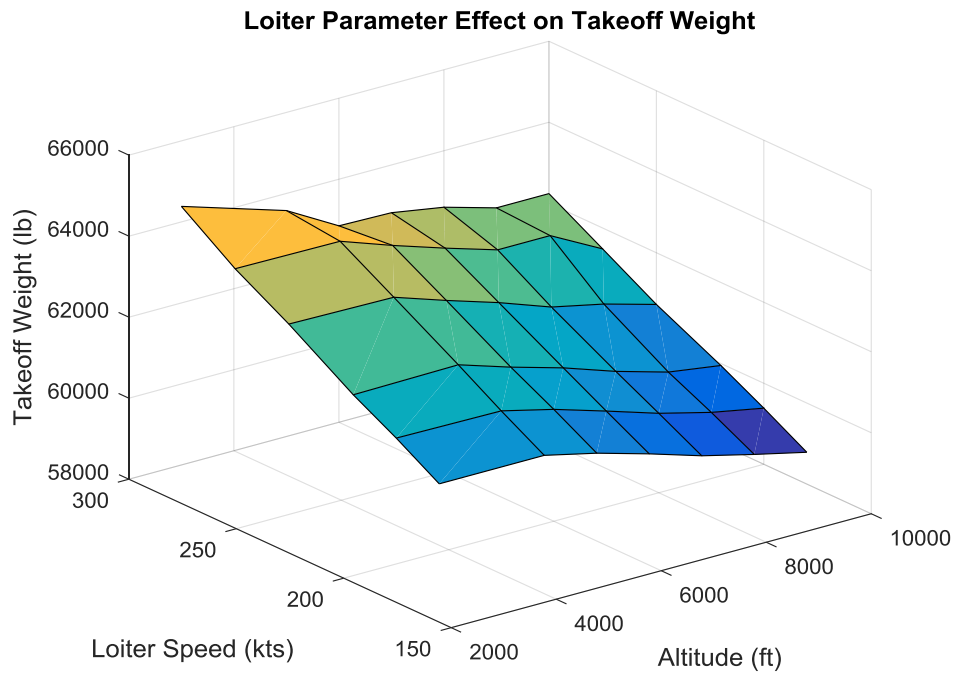


Fig. 14 Loiter design space carpet plot

Most of the same trends are observed except an optimal speed is less obvious. As loiter does not affect the objective function in these variables, the highest reasonable altitude and slowest reasonable speed is selected to reduce takeoff weight and in turn allow for longer loiter times.



Part VIII: Constraint Sizing

Energy constraint sizing relationships are modified from Mattingly [7]. The basis for constraint sizing stems from the energy based constraint equations provided in Eqns. 13-17.

$$\frac{T_{SL}}{W_{TO}} = \frac{\beta}{\alpha} \left(\frac{qS}{\beta W_{TO}} \left[K_1 \left(\frac{n\beta W_{TO}}{q} \frac{W_{TO}}{S} \right)^2 + K_2 \left(\frac{n\beta W_{TO}}{q} \frac{W_{TO}}{S} \right) + C_{D_o} \right] + \frac{1}{V} \frac{\partial}{\partial t} \left[h + \frac{V^2}{g_o} \right] \right) \quad (13)$$

$$\beta = \frac{W}{W_{TO}} \quad (14)$$

$$K_1 = \frac{1}{\pi A R e} \quad (15)$$

$$K_2 = 0 \quad (16)$$

$$q = \frac{1}{2} \rho V^2 \quad (17)$$

Table 14 provides the symbol names and descriptions:

Table 14 Descriptions of variables in Eqns. 13-17

W_{TO}	Takeoff Weight
T_{SL}	Thrust at Sea Level
β	Weight Ratio
α	Thrust Lapse
σ	Density ratio (ratio of local density to sea level)
n	Load factor
q	Dynamic Pressure
S	Wing Reference Area
K₁	1st Order Coefficient of Drag Polar
K₂	2nd Order Coefficient of Drag Polar (Assumed zero)
C_{D,0}	Zero Lift Drag Coefficient
V	Airspeed
g_o	Nominal Acceleration due to Gravity (32.2 ft/s ²)
e	Oswald's Efficiency Factor
AR	Aspect ratio



These equations are modified for various flight conditions to determine the effect on the required thrust to weight ratio and wing loading. This procedure is completed in accordance with the requirements provided in the RFP and selected MIL-STD. This constraint analysis involves the constraints from requirements on the cruise speed, the rate of climb, the aircraft's service ceiling, the takeoff distance, approach speed and the energy load factor. Values from Table 12 are again applied as common values used in between all flight phases. The final design space is given as Fig. 15 with explanation and trade studies following.

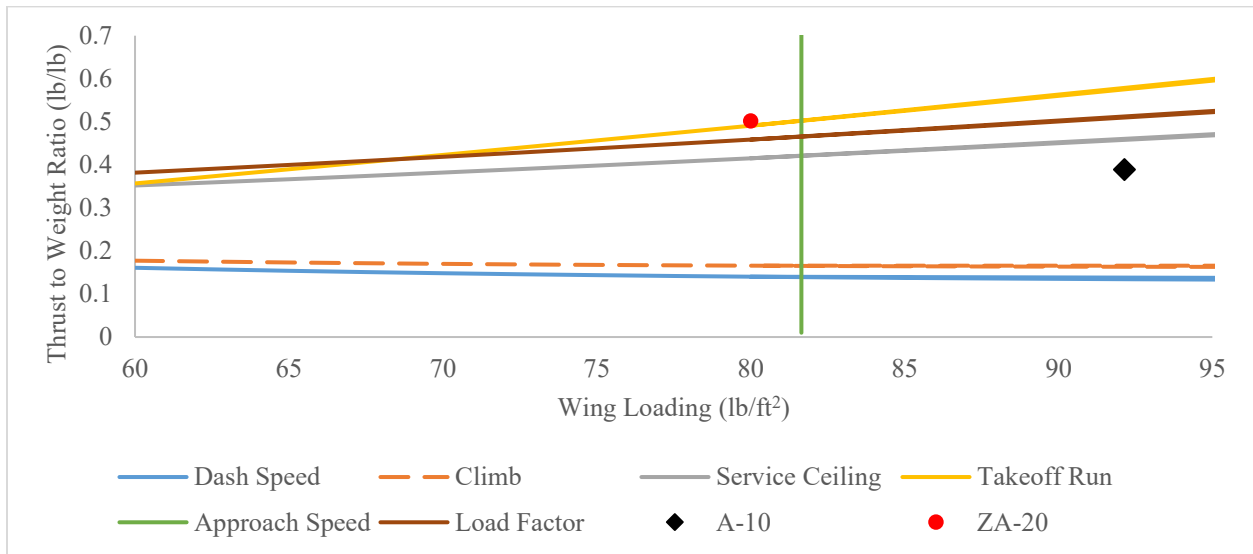


Fig. 15 Design point and constraint design space

Level Constant Speed Cruise

At cruise, the aircraft is assumed to be in steady level flight with a clean wing configuration. This implies that acceleration is zero, the climb rate is zero, the load factor is one, the configuration drag is zero, and the values for altitude and airspeed are known. This simplifies Eqn. 13 to the form shown in Eqn. 18.

$$\frac{T_{SL}}{W_{TO}} = \frac{\beta}{\alpha_{cruise}} \left(K_1 \frac{\beta}{q} \left(\frac{W_{TO}}{S} \right) + \frac{C_{D_o}}{\frac{\beta}{q} \frac{W_{TO}}{S}} \right) \quad (18)$$

In all constraint sizing analysis, the weight ratio is determined as the weight at the start of the flight phase as determined by the Mission Fuel Fraction, the thrust lapse is determined by the engine deck data [3], and the density at each altitude is calculated by the Standard Atmosphere.



The values used in this equation for cruise are provided in Table 15.

Table 15 Values for constraint equation during cruise

Variable	Value
β	0.963
α_{Cruise}	0.470
V	300 kts
Altitude	15,000 ft
ρ	0.00150 slug/ft ³

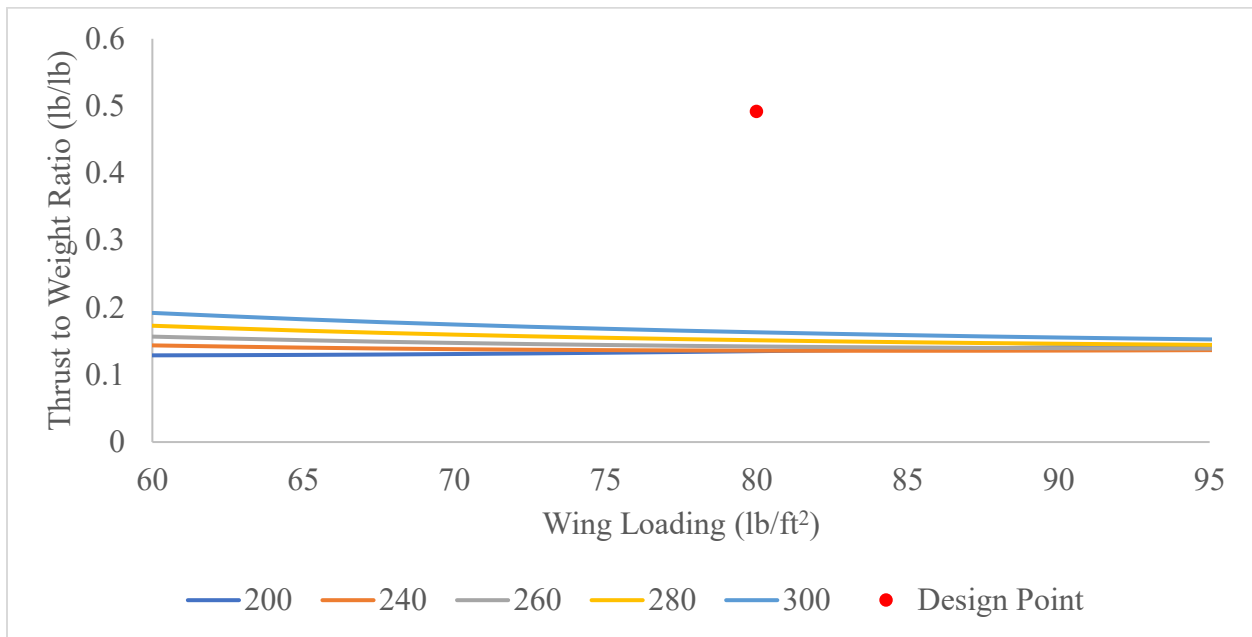


Fig. 16 Cruise speed trade study

A trade study of testing various cruise speeds is conducted in Fig. 16, but it is found to be a non-factor.

Steady Constant Speed Climb

In constant speed climb, the assumptions used to simplify the constraint equation are a constant speed, constant rate of climb, as well a load factor of approximately one. The values for the altitude, rate of climb, and airspeed are all known for the climb phase. Using these assumptions, Eqn. 13 becomes Eqn. 19 shown below.



$$\frac{T_{SL}}{W_{TO}} = \frac{\beta}{\alpha_{climb}} \left(K_1 \frac{\beta}{q} \left(\frac{W_{TO}}{S} \right) + \frac{C_{D_o}}{\frac{\beta}{q} \frac{W_{TO}}{S}} + \frac{1}{V} \frac{\partial h}{\partial t} \right) \quad (19)$$

The values input into equation are recorded in Table 16.

Table 16 Values for constraint equation during climb

Variable	Value
β	0.970
α_{Climb}	0.615
V	250 kts
Rate of Climb	1000 fpm
Climb Distance	15,000 ft
Density	0.00238 slug/ft ³

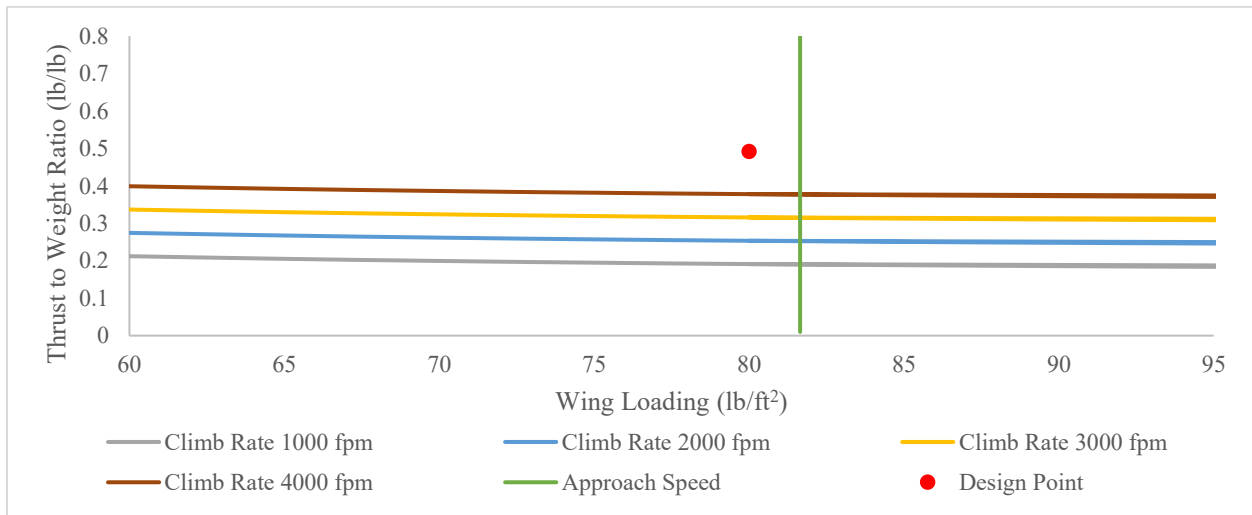


Fig. 17 Climb speed trade study

Service Ceiling

Service ceiling simply takes Eqn. 19 again but substitutes the density of the maximum altitude as specified by the RFP where the aircraft can climb at 100 fpm. Table 17 lists the assumed values for the design point calculation, and Fig. 18 captures the associated trade study.



Table 17 Values for constraint equation for service ceiling

Variable	Value
β	0.600
α_{Ceiling}	0.131
V	300 kts
Rate of Climb	100 fps
Altitude	45,500 ft
Density	0.000460 slug/ft ³

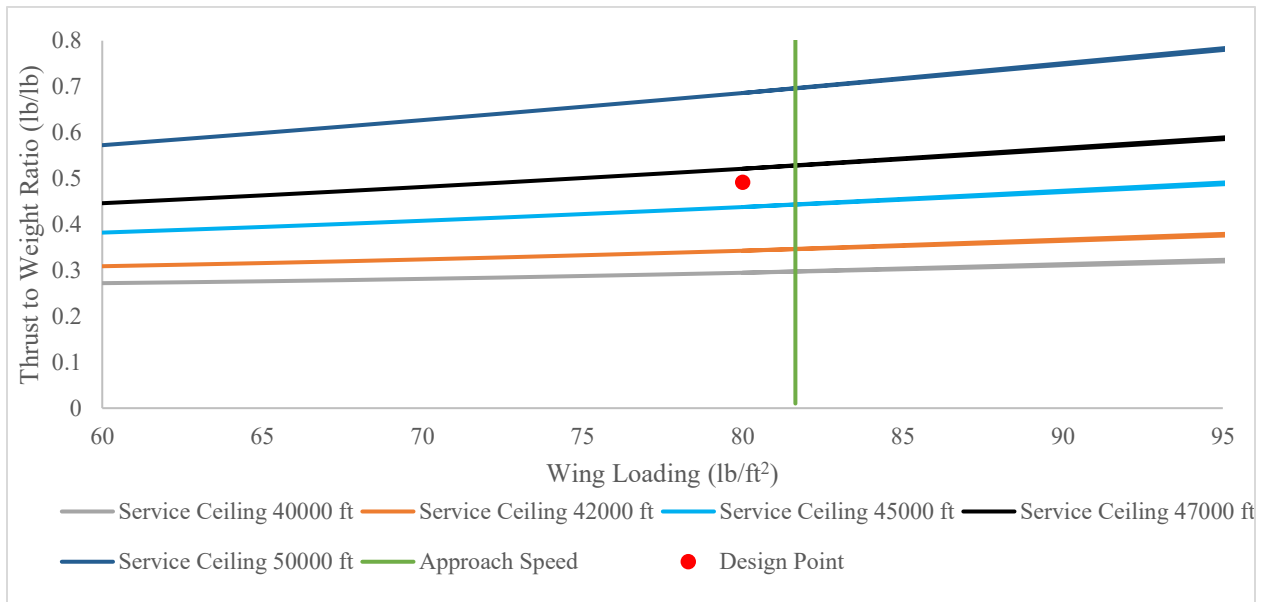


Fig. 18 Service ceiling trade study

From Fig. 18, the required service ceiling can strongly influence the required thrust to weight ratio at takeoff. While the RFP requirement is easily met, anything above 46,000 ft would not prove reachable by this design.

Takeoff Distance

The takeoff distance is approximated using a relationship for military takeoffs derived from Roskam [2] at the elevation and temperature required by the RFP. This equation is a function of the maximum lift coefficient available at takeoff, lift independent drag, bypass ratio of the engine, and the rolling drag coefficient estimated for the runway as well as parameters used in the other constraints. This relationship is listed as Eqns. 20 and 21.



$$R_2 = 0.75 * \frac{5 + BPR}{4 + BPR} \quad (20)$$

$$\frac{T_{SL}}{W_{TO}} = \frac{\beta}{R_2 \alpha_{TO}} \left(\frac{1}{C_{Lmax}} \left(\frac{0.0447 W_{TO}}{\rho \delta} \frac{1}{S} + 0.72 C_{Do} \right) + \mu_g \right) \quad (21)$$

Table 18 provides the parameters used in Eqn. 21, and Fig. 19 is the corresponding trade study.

Table 18 Values for constraint equation for takeoff run

Variable	Value
Takeoff Distance (δ)	3,000 ft
Assumed Max Lift Coefficient	2.2
Runway Drag Coefficient (μ_g)	0.08 [8]
β	0.99
α_{TO}	1.000
Bypass Ratio (BPR)	11.0 [9]

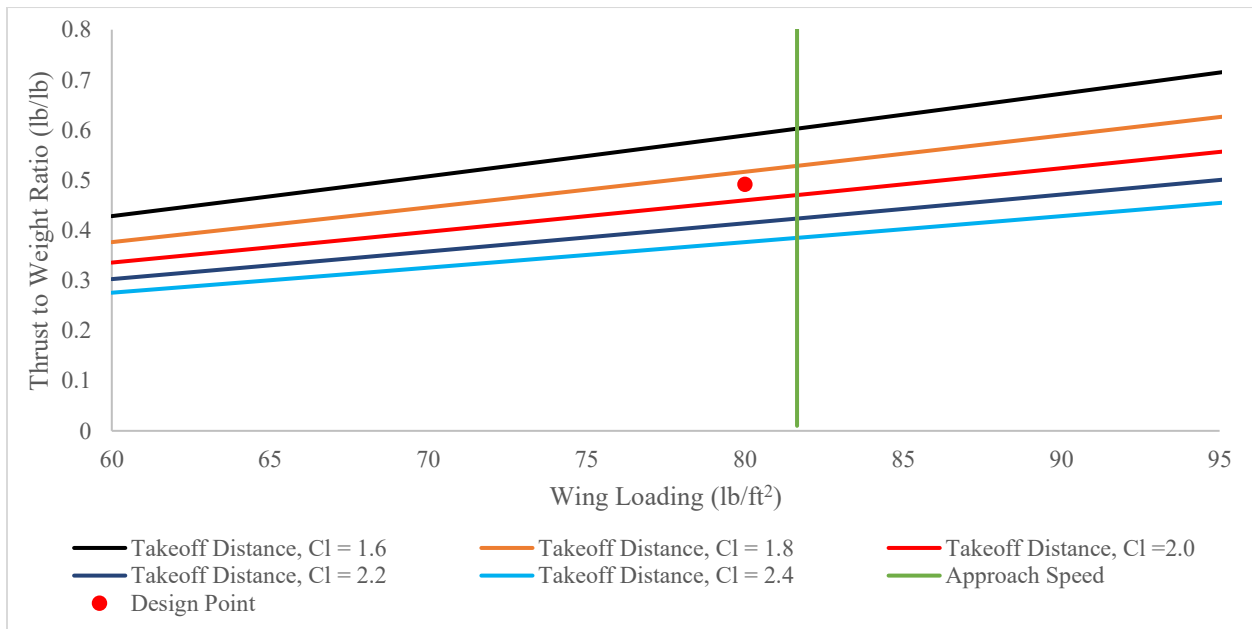


Fig. 19 Takeoff run trade study

The assumed lift coefficient as recommended by Roskam [2] is verified by Fig. 19 as providing adequate risk reduction for this requirement incase this lift coefficient. However, as found in later sections this assumption is confirmed valid.



Approach Speed

The approach speed constraint is based again off $C_{L,max}$ and is a constant wing loading at any thrust to weight ratio. It is calculated as Eqn. 22 which is simply the stall speed in landing configuration with a chosen safety factor at the RFP requirement altitude and temperature. The active constraint line for approach speed listed in each of the previous figures is calculated at the same stated assumed lift coefficient.

$$\frac{W_{TO}}{S} = \frac{\rho(V_{stall})^2 C_{L,max}}{2\beta K_{app}^2} \quad (22)$$

The values used in this relation are provided in Table 19 below.

Table 19 Values input into constrain equation for stall speed

Variable	Value
V_{stall}	167 kts
$C_{L,max}$	2.2
β	0.99
Density	0.00197 slug/ft ³
K_{app}	1.2

Ninety-seven percent of the aircraft takeoff weight is used in the case that the aircraft will require a landing immediately after takeoff. As the primary varying factor is again assumed to be the lift coefficient, no trade study is performed on this constraint.

Load Factor

As a final constraint, load factor as listed in the RFP is considered. This constraint can be determined at multiple flight conditions, but parameters expected during the attack run when loadings are likely to be at their highest are selected. Equation 13 is again modified to include the aircraft load factor for Eqn. 23.

$$\frac{T_{SL}}{W_{TO}} = \frac{\beta}{\alpha_{man}} \left(K_1 n^2 \frac{\beta}{q} \left(\frac{W_{TO}}{S} \right) + \frac{C_{D_o}}{\frac{W_{TO}}{S} \frac{\beta}{q}} \right) \quad (23)$$

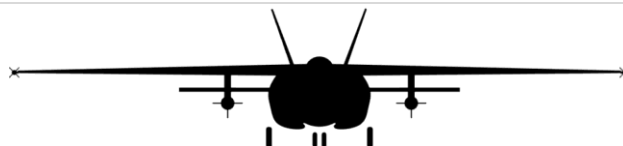


Table 20 lists the assumed values for the design point calculation, and Fig. 20 captures the associated trade study which finds load factor to be a design driver.

Table 20 Values input into constrain equation for load factor

Variable	Value
β	0.550
α_{man}	0.657
Load Factor (n)	6.0
V	250 kts
Altitude	5,000 ft
Density	0.00205 slug/ft ³

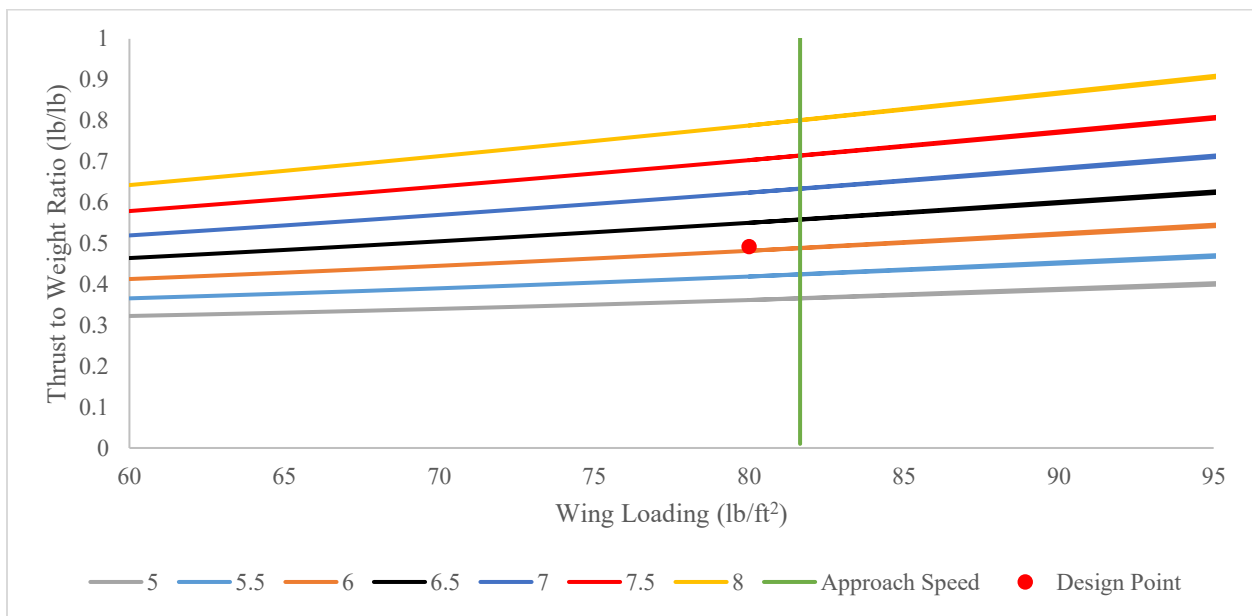


Fig. 20 Load factor trade study

As demonstrated by Fig. 20, the final takeoff weight is quite sensitive to the maneuver load factor based on the energy equation. In fact, at the chosen design point even with a mostly unloaded aircraft based on mission fuel fraction, following the RFP requirement of a load factor of eight would push the thrust to weight ratio to unreasonable levels. From this, it is believed to be justified to utilize a chosen maximized load factor of six and incur the penalty in objective function. As this is a CAS aircraft, and not an Air Superiority Fighter where maneuverability is a top concern, it is determined that this will not sharply harm mission capability.



Part IX: Dash Speed, Takeoff Length, and Maximum Load Factor

Dash speed, minimum takeoff length, and maximum load factor all follow a similar calculation scheme as a follow-on procedure to constraint sizing. This is because the three each depend on finding the margin in takeoff weight ratio between the current assumed value and the point where any more performance would cause the parameter to become a design driver and would necessitate an increase in the thrust to weight ratio. For example, the cruise speed constraint is directly linked to dash speed by increasing the required cruise speed until the demanded speed is no longer achievable at the current design point. This would occur in Fig. 16 when the constraint line raises to the point it touches the design point at the selected wing loading. Load factor is found the same way, but takeoff length is found by decreasing the distance as decreasing takeoff run is more demanding and desirable.

Dash speed is artificially limited to a local Mach 0.8 to avoid considerations for any complex transonic effects. With the sweep of the wings, Mach 0.8 is expected to exist below the critical Mach number of the aircraft. While the aircraft most likely could fly faster than this speed at an increased cost in terms of wave drag, the dash speed is still limited to avoid unreasonable speeds without the wave drag and high compressibility included in the drag calculations. This proves a risk reduction step to avoid overselling projected performance.

This process is completed iteratively for these three performance measures for any selected mission and becomes a loop necessary to be closed by the objective function optimization. Below Fig. 21 demonstrates the constraint space with these values optimized.

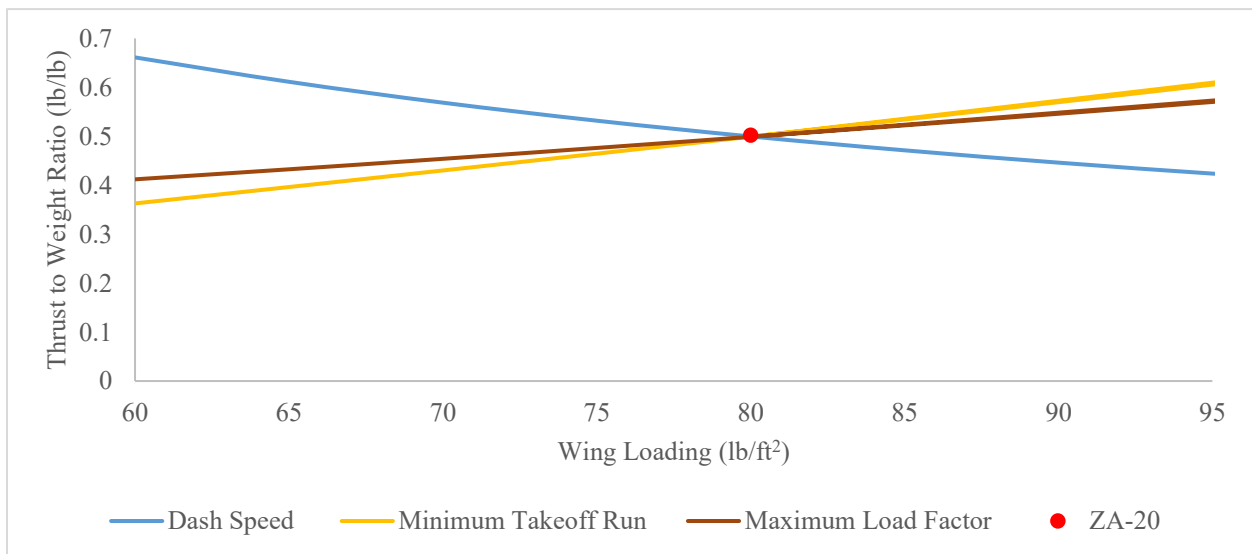


Fig. 21 Optimized performance constraint space



Part X: Cost Analysis

Unit Cost

For the total fly-away cost of the aircraft including all development, testing, materials, and manufacturing, an estimate is performed using the Nicolai Life Cycle Cost method [10]. This estimation scheme calculates total expected cost of different segments either in direct dollars or total work man-hours to be paid to those employed in the project including associated benefits. The method was developed in 1998, but an inflation factor is included with all figures to update them to 2017 dollars. The total cost is found for both a production run of 500 and 1,500 aircraft per the RFP. Two test aircraft are expected to be built which adds to both production runs. Table 21 below lists each category used in the calculation and their associated labor rates.

Table 21 Production and development cost categories

Variable	Category	Labor Rate (Dollar/hour)
AE	Airframe Engineering (Hours)	123.05
TT	Tooling (Hours)	126.26
ML	Manufacturing Labor (Hours)	104.86
DS	Development & Support (Dollars)	-
FT	Flight Test (Dollars)	-
QC	Quality Control (Dollars)	-
MM	Manufacturing Materials (Dollars)	-

Below in Eqns. 24 through Eqn. 30 the curve fit relationships for each cost category are listed. As evident, the total program cost of each category is found to simply act as a function of the major design drivers of total number of aircraft produced, dash speed as found previously, and the empty weight of the aircraft.

$$AE = 4.86 W_e^{0.777} V_{max}^{0.894} n^{0.163} \quad (24)$$

$$DS = 66 W_e^{0.63} V_{max}^{1.3} \quad (25)$$

$$FT = 1852 W_e^{0.325} V_{max}^{0.822} n_{test}^{1.21} \quad (26)$$

$$TT = 5.99 W_e^{0.777} V_{max}^{0.696} n^{0.263} \quad (27)$$

$$ML = 7.37 W_e^{0.82} V_{max}^{0.484} n^{0.641} \quad (28)$$

$$QC = 0.13 ML \quad (29)$$

$$MM = 16.39 W_e^{0.921} V_{max}^{0.621} n^{0.799} \quad (30)$$

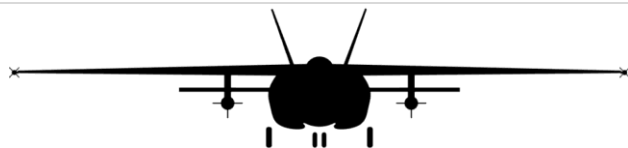


The resulting costs per program and total program cost without avionics are listed in Table 22. The cost of the avionics is assumed to equal 30 percent of the total cost of modern military aircraft unit cost [11]. The selected engine from the CFM International LEAP family has a unit cost of \$10.6M [12] which when added with the avionics cost produces the final fly-away unit cost.

Table 22 Nicolai cost analysis

Aircraft Produced	500	1,500
AE Cost	\$583 M	\$697 M
TT Cost	\$444 M	\$592 M
ML Cost	\$2.1 B	\$4.4 B
DS Cost	\$83 M	
FT Cost	\$17 M	
QC Cost	\$4.0 M	\$8.0 M
MM Cost	\$1.0 B	\$2.6 B
Cost Without Engine	\$8,797,000	\$5,607,000
Engine Cost	\$10.6 M	
Avionics Cost	\$8.3 M	\$6.9 M
Flyaway Unit Cost	\$27,710,000	\$23,154,000

Overall the fly-away cost arises as higher than the current A-10, but some of this disparity stems from inflation differences. As will be demonstrated with the objective function, the new aircraft's increase in price proves more than justified with performance, especially when the fact that the resulting airframe comes brand new at zero hours with multiple innovations while still maintaining value at the forefront of the design. This departs in stark contrast to the performance-at-any-cost philosophy prevalent in recent military designs. In all future calculations the fly-away cost of 500 production aircraft is utilized, as although the greatest optimism is applied to the commercial success of the design, the current budgetary climate for military aircraft acquisitions is forecasted to remain slow without a new major conflict. United States sanctions on international sales of next-generation proprietary designs could also easily hamper the total available market. Therefore, an estimated production run of 500 aircraft is projected as a risk-reduction method. If demand proves greater than this conservative estimate, the unit price of the aircraft will only ultimately decrease, as per T.P. Wright, the more humans complete a task, the more proficient they become and the less time the task requires to complete [13]. This concept is included as Fig. 22.



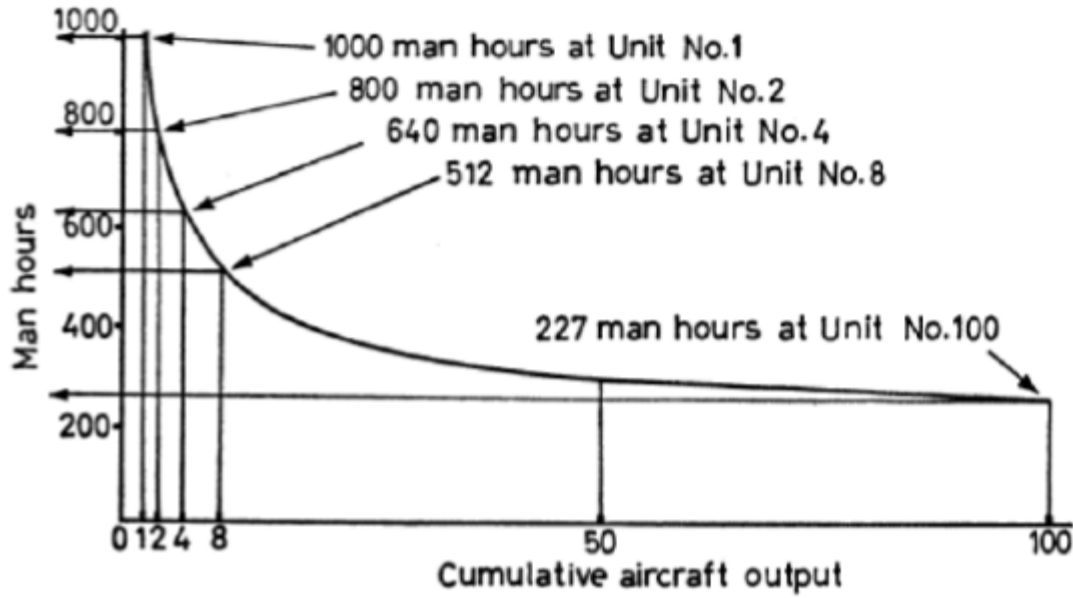


Fig. 22 Wright cumulative learning curve [13]

Operating Cost

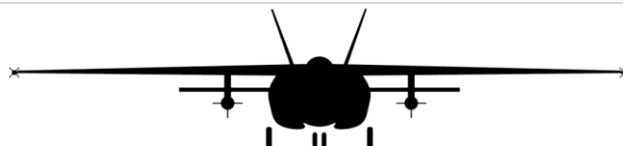
The operating cost per hour is calculated around an assumed total annual number of flight hours of 300. This proves again a conservative estimate, as many USAF airframes of similar operations tempo can fly many more operation and training hours in a year, but this aircraft can certainly expect to fly at least 300 hours in a year, and increasing the assumption point only raises the risk of underestimating the operating cost per hour which acts as a risk reduction.

Operating cost is broken down into three major contributors: Materials Cost which includes parts, supplies, and pay for supporting personnel, Fuel Cost, and Crew Pay for the flight crew. Materials Cost per flight hour (MC) is a function of the following variables per Table 23 and calculated by Eqn.31 [14].

Table 23 Materials cost parameters

Variable	Value
Unit Cost Without Engine (C_a)	\$8,797,000
Engine Cost (C_e)	\$10,600,000
Number of Engines (N_E)	1

$$MC = 3.3 \frac{C_a}{10^6} + 10.2 + \left(58 \frac{C_e}{10^6} - 19 \right) N_E \quad (31)$$



Fuel Cost simply takes the calculated mission time, fuel used, and current fuel cost of the design mission and assumes this as the typical mission for fuel burned per hour. Table 24 lists the values used in this calculation.

Table 24 Fuel cost parameters [15]

Variable	Value
Total Mission Time	10.08 Hr
Fuel Used	13,821 lb
	2,051 gal
Cost per Gallon	\$3.73

Crew Cost (CC) is calculated from a weighted average of the expected distribution of flying officers in each group as a function of their respective base pay as published by the Department of Defense and a ratio of flight crew to aircraft in operation ($Ratio_{crew}$) of 1.1 as suggested by Raymer [16]. This is given as Eqn.32. The expected distribution of flying officers and their base pay from 2017 [17] is given in Table 25. Other benefits like Basic Housing Allowance or Flight Pay is not considered in this first order estimate.

Table 25 Officer base pay [17]

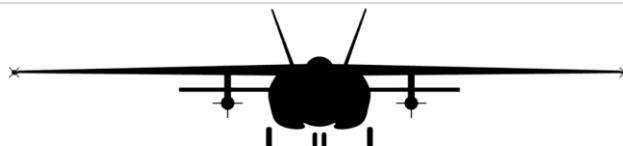
Rank and Time in Service	Base Pay (BP_i)	Percentage of Officers (P_i)
Captain, Over Four	\$5,398	70%
Lieutenant Colonel, Over Eight	\$6,918	20%
Colonel, Over Ten	\$7,885	10%

$$CC = 12 Ratio_{crew} (\sum (BP_i P_i)) \quad (32)$$

The final costs from each major contributor and in total per flight hour is tallied in Table 26.

Table 26 Final hourly operation cost

Cost Contributor	Cost per Hour
Materials Cost	\$1,053
Fuel Cost	\$759
Crew Cost	\$262
Total Cost	\$2,074



Part XI: Optimization Scheme

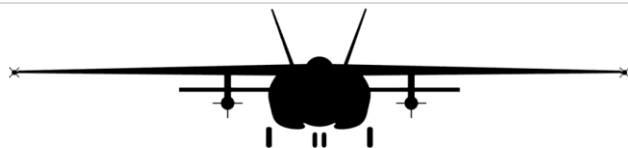
Over the course of the design, one of the greatest challenges proves finding an effective way of simultaneously converging all dependent assumed mission parameters, calculating and converging the resulting aircraft performance relevant to the objective function, and then actively optimizing the objective function to balance all compromises in mission and aircraft performance to find the optimum mission and aircraft per the weightings found in the Stakeholder Analysis.

Method

This quickly becomes an n-space optimization problem, as the design tool must not only maximize output of the final objective function given as Eqn. 33 from the seven performance outputs, but also converge and calculate the performance outputs themselves at multiple levels of convergence by the methods discussed over the past multiple sections of this report.

$$OF = W_1 \left(\frac{\text{Range}_{4hr \text{ Loiter}}}{500 \text{ nm}} \right)^2 + W_2 \left(\frac{V_{max}}{300 \text{ KTAS}} \right)^2 + W_3 \left(\frac{V_{cruise}}{200 \text{ KTAS}} \right)^2 + W_4 \left(\frac{\$40M}{\text{Unit Cost}} \right)^2 + W_5 \left(\frac{\$3000}{\text{Operating Cost}} \right)^2 + W_6 \left(\frac{6000 \text{ ft}}{\text{Takeoff Run}} \right)^2 + W_7 \left(\frac{\text{Max Load Factor}}{8} \right)^2 + \begin{cases} 1, \text{ stealth} \\ 0, \text{ external} \end{cases} \quad (33)$$

From the previous sections, Vmax, Takeoff Run, and Max Load Factor are calculated at each point from constraint sizing, V_{Cruise} is constrained as determined from the trade studies, and costs are calculated at each mission point as discussed. This leaves the two final optimization loop variables as Range, constrained to the RFP requirement, and Cruise Speed, which is a known also constrained by RFP requirement, but quickly increases required takeoff weight from increased drag. The ultimate intent of this optimization is to maximize the objective function by increasing these two mission parameters in the best combination to the point right before secondary consequences render any further demanded performance detrimental to the stakeholder in terms of tradeoffs. This opportunity cost stems from layers of interdependencies in the model. For example, increasing the mission combat range directly increases required fuel, which means a higher takeoff weight, which increases costs and takeoff run, and reduces load factor. Because of the selected factor weighting, this may or may not prove enough to increase the objective function, but each factor reaches a point where diminishing returns become dominant.



The optimization tool is built from scratch in Excel, and through clever data manipulation optimizes the entire system in one scheme utilizing built in optimization solvers. The solver operates at three major iterative levels with constraints assigned to each variable.

First, the mission profile is calculated from selected constant flight phases, payloads, and Mission Fuel Fractions. At this single point the lift to drag ratio at each flight phase is converged and any weight saving estimates from advance materials in the structural design and choice of engine are converged.

Next the empty weight and takeoff weight are iteratively converged as described in the weight sizing section to minimize the difference in the calculated and assumed takeoff weight. After each step in this loop, the lift and drag loop again needs to be closed to satisfy that assumed drag equals the calculated value at that point.

Finally, in the third outer loop, each factor used in the objective function is found, the current value of the objective function is calculated, and then the solver jumps back to the beginning, alters the initial cruise speed and range and repeats the process. After a few points immediately surrounding the initial guess are tested, the solver follows the gradient vector of steepest ascent until a local maximum or a boundary condition is reached. Multiple runs are completed to pick the largest local maximum. This flowchart is outlined below as Fig. 23.

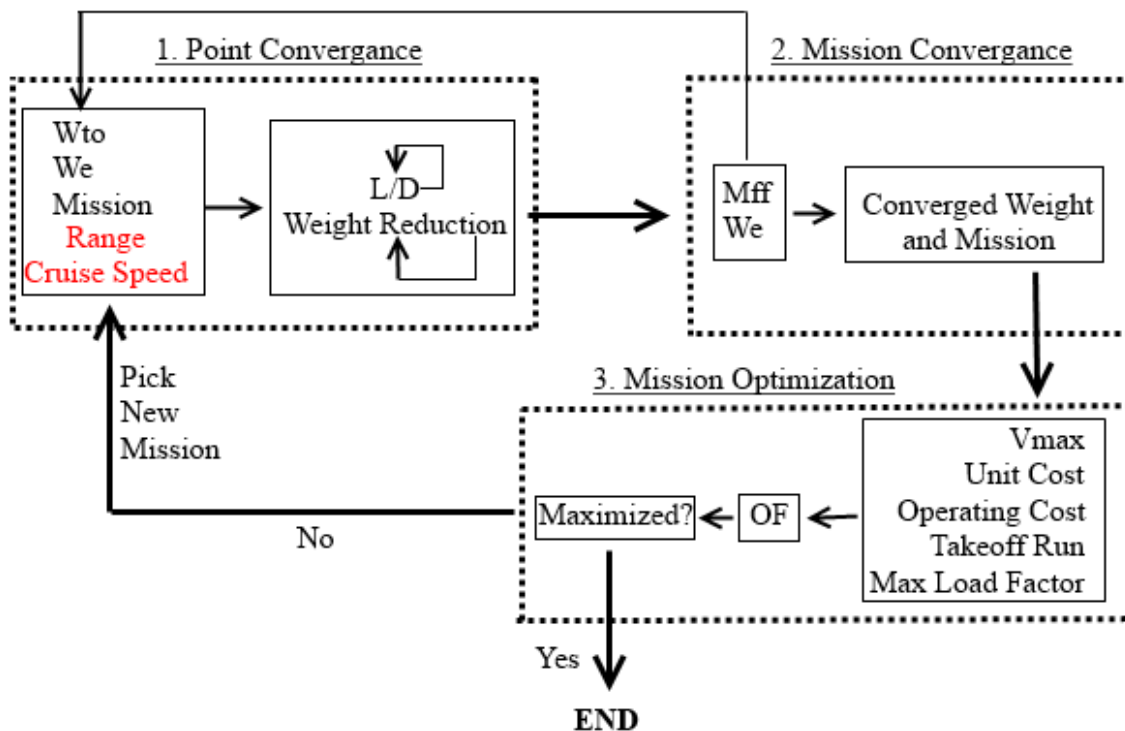


Fig. 23 Optimization flow logic



Because of limitations within Excel, only one goal-seek, minimization, or maximization optimization scheme can be commanded and saved into memory at once. Excel also does not allow utilizing directly calculated values in comparison iteration steps because this forms recursive formulas. To circumnavigate this handicap, converging multiple values while still within the overall Objective Function can be accomplished with dummy variables and active constraints. For example, for the lift to drag ratio calculated for each flight phase to find the phase Mission Fuel Fraction, a ‘guess’ or dummy variable for the local lift to drag ratio is inputted into the active calculation to find the Mission Fuel Fraction. A cell finding the difference between the dummy ratio and the actual ratio found by the drag polar is then added. In the optimization scheme the dummy cell is added as the variable cell the program can alter in iteration, and the difference cell is set as a constraint within a small margin of zero. This is necessary to act as an iterative part of the convergence process, as the weight at each phase directly affects the local lift to drag ratio, and the lift to drag ratios over the course of the flight affect total weight circularly.

A similar process is followed for both the weight reduction technology factor (η) of the structure and the engine to be discussed in the weight estimation section, the thrust required by the engine, and the weight-sizing empty weight convergence. The convergence tolerances of these variables are listed in Table 27.

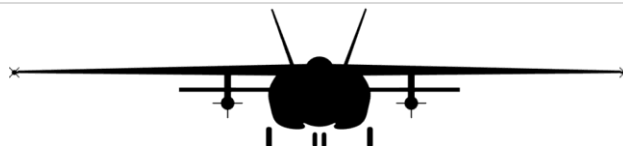
Table 27 Convergence tolerances for optimization

Variable	Constraint
Lift to Drag Ratio	± 0.02
Required Thrust	± 0.02 (lb)
η_{Wing}	± 0.0001
η_{Engine}	± 0.0001
Empty Weight	± 1.0 (lb)

All convergence values are then run through one last layer of convergence in Eqn. 34 below.

$$Output = \sqrt{\sum (Dummy_i - Actual_i)^4} \quad (34)$$

The output of this equation is constrained to a similarly near zero low value, and if it is met a high degree of confidence can be held that the system is properly converged to all constraints.



Results and A-10 Comparison

The final results of this analysis are below in Table 28. Because, as to be discussed in the fuselage design section, the majority ordnance is stored internally, the binary stealth criteria is determined to be met for the ZA-20.

Table 28 Design objective function results [4][5]

A-10			
Category	Weighting	Output Value	Normalized Contribution
Range	0.20	250 nm	0.0152
Dash Speed	0.10	450 KTAS	0.0683
Cruise Speed	0.10	300 KTAS	0.0683
Fly-Away Cost	0.25	\$18.8M	0.3434
Direct Operating Cost	0.20	\$17,000 per hr	0.0008
Takeoff Length	0.10	4,500 ft	0.0539
Max Load Factor	0.05	8.0	0.0152
Non-Observable Stores	No	0.0	0.0000
Objective Function Score	1.8657		
ZA-20			
Category	Weighting	Output Value	Normalized Contribution
Range	0.20	700 nm	0.1189
Dash Speed	0.10	501 KTAS	0.0846
Cruise Speed	0.10	300 KTAS	0.0683
Fly-Away Cost	0.25	\$27.7M	0.1581
Direct Operating Cost	0.20	\$2,074 per hr	0.1270
Takeoff Length	0.10	2,900 ft	0.1299
Max Load Factor	0.05	6.4	0.0097
Non-Observable Stores	Yes	1.0	0.3034
Objective Function Score	3.2955		

From the results, it is not surprising that the heavily weighted factors of costs contribute the most behind the lump sum of observability. At the conservative estimate of \$28M per aircraft, the design is well below the budgeted \$40M. The simple design, maintenance considerations of the aircraft, off the shelf components, super-efficient single engine, and single-seat operation also contribute to a low hourly cost of operation.



Impressive loaded takeoff performance and single-fueling combat range also especially push the objective score farther into the black. This level of range, which still includes four hours of overwatch, could easily transfer to loiter times if target areas are closer to the base of operations. Loiter times and range also can be extended nearly indefinitely by aerial refueling, but time spent fueling translates to time away from the fight. As discussed previously, the most important aspects of a CAS prove the ability to reach and spend time on station protecting blue forces on the ground at an effective cost, which this design excels at.

Comparing apples to apples, the new design nearly doubles the total objective score of the old A-10. The new design is superior in almost every category with the exception of fly-away unit cost, in which the A-10 holds a serious advantage and max load factor where the A-10 holds a respectable advantage. Although the new design has been approached with the philosophy of minimizing accession and design cost to the point where the two cost factors stand weighted the highest of any other in the optimization scheme, no new design of a satisfactory level of performance could compete in terms of development cost with the industry-favorable conditions that existed at the time of the A-10 development and production. However, as a direct balance the current cost per flight hour of the A-10 is much higher than that of the proposed aircraft. This is both because of the increased maintenance cost of keeping decades old aircraft airworthy, and the increased fuel cost of the less efficient engines. In all other interested areas, the new design provides dominant benefits in terms of direct improvement.

In conclusion, especially when coupled with the A-10's fleeting service life and no other direct mission capable aircraft ready to fill the role, this design is more than justified in terms of performance and long-term cost benefits for production as a new design to fill this desperately critical role in the United States Air Force's Mission.



Part XII: Fuselage Design

In designing a fuselage to carry out the mission as described, many factors must be simultaneously incorporated into the final configuration ranging from landing gear stability and center of gravity excursion to be explored in a later section, to weapons and cockpit integration. This portion in some respects is the most important, as placing the systems in respect to the layout is when the project ceases acting as a ‘paper airplane’, and becomes a feasible airframe. Although this initiates the most preliminary of analysis, as millions of man-hours will eventually become required to route each hydraulic line, optimize the final shape of compartments, and integrate thousands of parts, the initial proof of concept follows to ensure spaces exist for major systems and to demonstrate the thought process behind the layout.

The primary design driver proved to be integrating the sheer size of the high bypass engine, especially in diameter, into the fuselage. At its widest, at the fan, seven feet in diameter plus margins for the aircraft structure itself must be allotted. This expands the width overall of the airframe to a size larger than typical for a single seat attack aircraft. This opens up benefits and opportunity for utility as well as the expected detractors of radar cross-section and platform drag. Initially, the weapons stores were expected to be placed along stations underneath the wing for simplicity, however it is discovered that with the ample internal volume of the design an internal rotary weapons bay similar to the B-1 or the recent updates to the B-52 is utilized. Keeping the majority of weapons internal qualifies the aircraft for the low weapons observability requirement of the Objective Function. An important challenge to approach with further analysis proves designing suitable air intakes and ducts that deliver the required mass flow rate to the engine without experiencing excessive internal turbulence or contributing harsh profile drag, as the fan is not directly exposed to the free stream as is usual with these powerplants. A representative air intake system is included as a first order demonstration. Each intake is just over one half of the area of the fan and is offset from the skin to avoid boundary layer ingestion. The intakes also act as a combined diffuser and first stage compressor, taking advantage of ram air effects.

Dimensions and Diagrams

On the following pages in Fig. 24, Fig. 25, and Fig. 26 the overall dimensioned orthographic diagrams produced in SolidWorks of the design are included with Fuselage Station, Butt Line, and Water Line defined as well as a rendered isometric image.



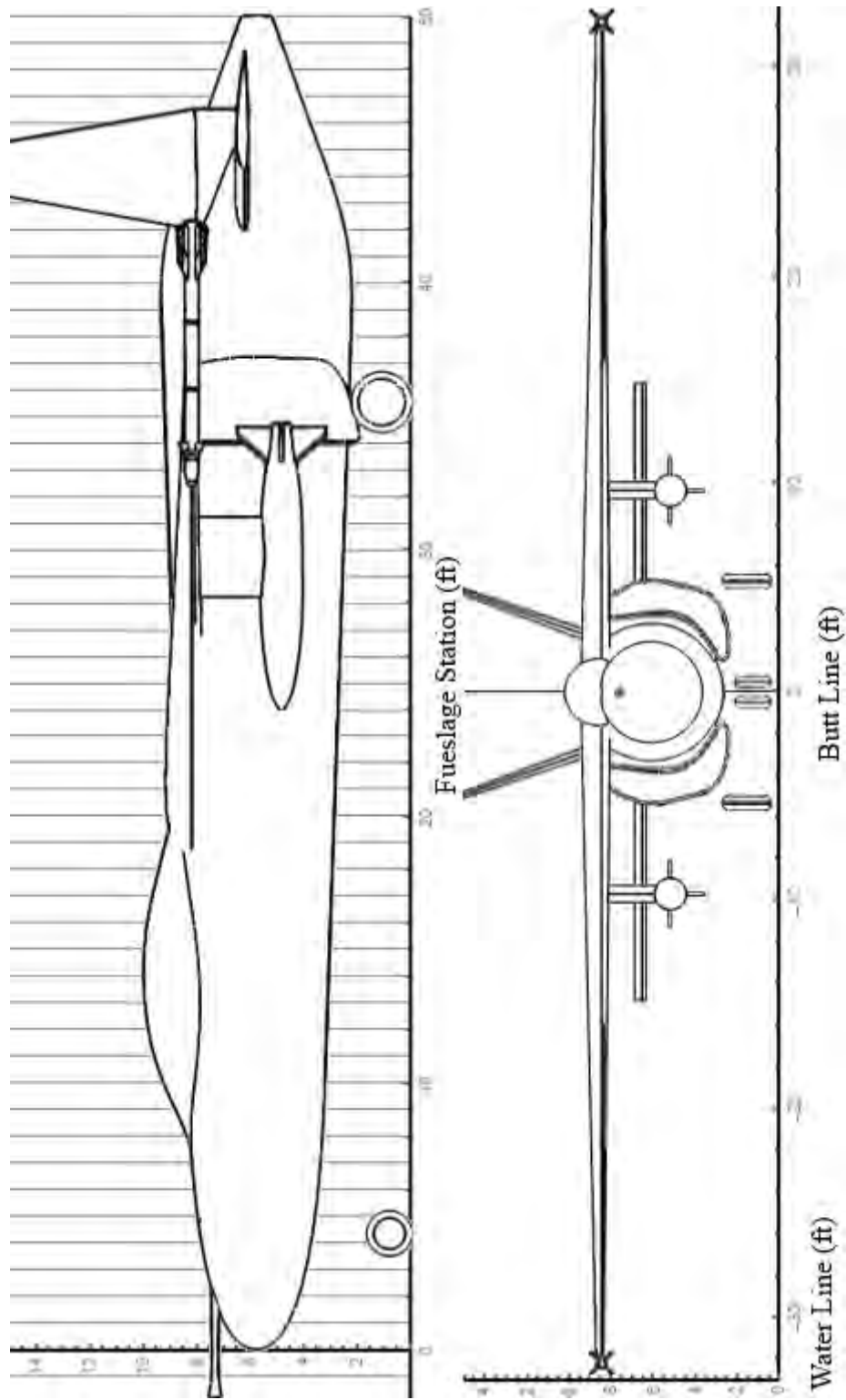


Fig. 24 Aircraft dimensions



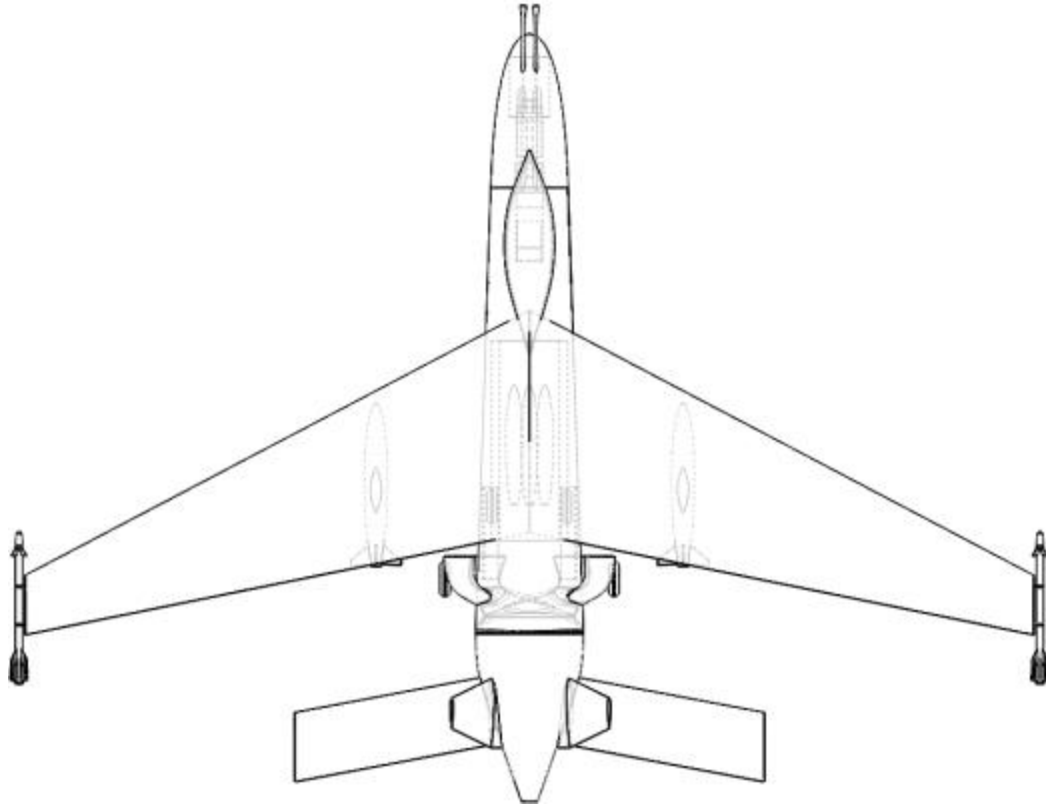


Fig. 25 Overhead x-ray view

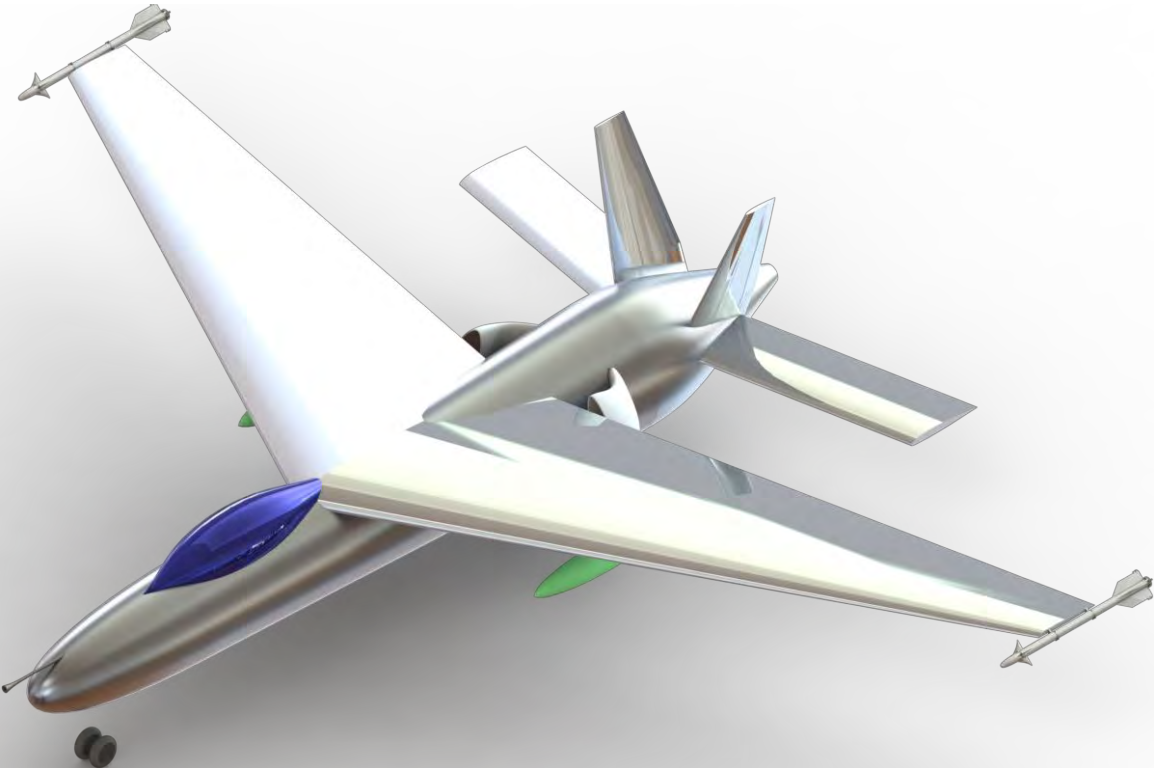
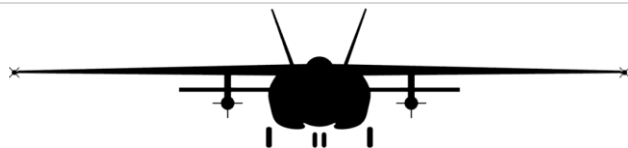


Fig. 26 Rendered isometric image



Propulsion Integration

The selected power plant is the CFM LEAP-1A High-Bypass Turbofan which family powers the latest generation of both the A320 and B737. This cutting-edge jet engine represents the current best state of modern weight and efficiency possible. This engine entered service in 2017, with all development, supply chain, and support infrastructure already established. This gives cutting edge performance without the development risks associated with designing a new engine. The powerplant boasts 15 percent TSFC improvement over the already impressive performance of the previous generation of turbofans, meets the necessary 25,000 lb of thrust required for the design with some thrust to spare, a bypass ratio of 11 and compressor ratio of 40, and weighs 15 percent less than the previous similar turbofans because of modern additive manufacturing and composite integration [9]. These innovations in an already operating and proven design at a reasonable cost assist to meet all requirements for the Colt, and perfectly fits the application for a turbofan in an attack aircraft where efficiency greatly contributes to the ability to engage targets far from base and also facilitates game-changing time on station.

Beyond the air intakes, the fuselage is hollow and dedicated to the engine installation. The tail cone is designed to follow the taper of the engine, as once past the fan stages the diameter sharply decreases for the engine core. Bypass flow is routed around the primary turbomachinery and finally remixed with the hot exhaust gas in the tail nozzle. Controls for all empennage control surfaces are routed through multiple reinforced channels for redundancy and to protect from catastrophic engine failure. Although this common, off the shelf, commercial powerplant is expected to validate itself as more reliable and requiring much less maintenance than the cutting-edge turbojets with afterburners often used, routine maintenance up to engine swaps will be necessary often over the life of the airframe. To facilitate this, the cowling on the underside includes access panels near the most commonly inspected machinery. Also, the entire cowling underneath the horizontal stabilizer is removable. The engine itself is removed by dropping straight down and out. A cross section of the tail cone including the selected engine illustrating the general installation is below as Fig. 27.



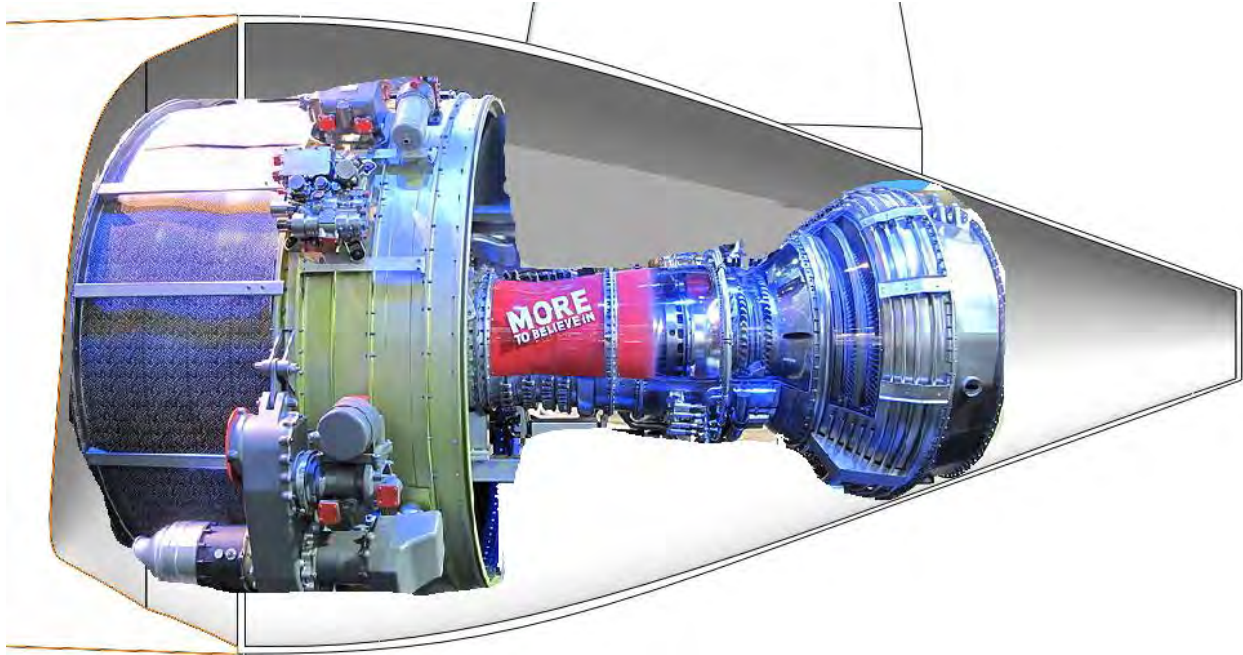


Fig. 27 Engine installation [18]

Weapons Integration

The primary inspiration for the primary weapons bay is the Conventional Rotary Launcher (CRL) utilized in the B-1 Lancer shown in Fig. 28.



Fig. 28 Conventional Rotary Launcher [19]

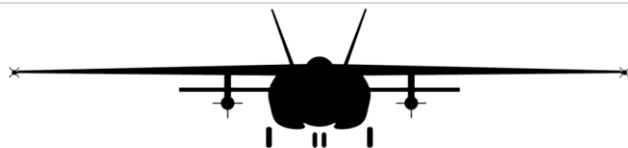
This system allows for not only the efficient storage of ordinance, but also a variety of weapons systems to be loaded onto the aircraft at once. Below in Fig. 29 are shown the relative sizes of two very common weapons loaded on current attack aircraft, unguided ‘dumb’ bombs, and the laser guided AGM-65 Maverick missile.





Fig. 29 Weapons bay side cross-section [20]

The primary weapons bay runs continuously from Fuselage Station 12 to 25, or for 13 uninterrupted feet. The space can also be reconfigured to accommodate ordnance up to 21 inches in radius which allows the aircraft to add nuclear capability if necessary. While AGM-65 Mavericks typically require visual line of sight with the target, when the missile is stored internally this telemetry will be fed to the missile via the primary visual/infrared sensor package located at the bottom of the fuselage. This location is chosen to supply maximum targeting visibility to the ground. In the A-10 at any given time with the external wing station targeting pod, a significant portion of the battle space is obscured by the aircraft. With the bottom permanently affixed sensor location, 100 percent of the horizon is visible with banks up to 15 degrees. Visual line of sight with the guidance laser will reestablish after the Maverick is clear of the bay. Up to six “six-shooter” (and hence namesake of the design) internal stores can be loaded as shown in Fig. 30.



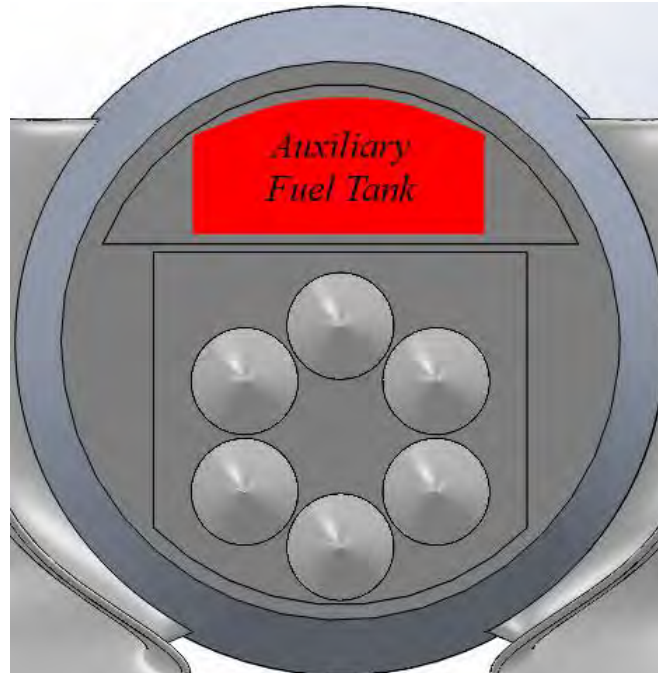


Fig. 30 Weapons bay front cross-section

Larger ordinance as required for a full mission loadout are attached to two under the wing hardpoints. Finally, two wing tip stations allow for air-to-air capability primarily intended for self-defense or use against vulnerable targets like hostile helicopters. Any external hardpoints also are compatible with external fuel tanks to allow for mission flexibility and extended range for ferry flights. The fuel tank above the weapons bay provides the capability for an extra 389 gal of fuel beyond mission requirement, and the fuel tank also includes internal baffles to prevent extreme weight shifts.

In response to one of the A-10's most recognizable and beloved features-- its gun, the RFP requires an upgraded caliber of 35 mm as opposed to the 30 mm of the A-10. In the interest of cost and keeping with the design philosophy of utilizing off the shelf equipment whenever possible, despite few options in this caliber, the design of a new gun system is ruled out. Instead, the Swedish Rheinmetall KDG Millennium 35 mm AA cannon [21] is chosen for conversion to airborne service. This system is chosen for its proven design, small size and rate of fire. Because the cannon is a single barrel system, two guns are integrated into the nose as shown in Fig. 31. The ammunition hopper is located behind the cockpit and the cartilages are fed forward by a linked belt system. The ammunition loading hatch is located on the bottom of the fuselage clear of the wings or other obstructions for ease and efficiency of loading. All hot gun exhaust is piped behind the cockpit



and to the top of the fuselage. This is to prevent obstructing the pilot's vision during the critical attack flight phase, and to prevent engine ingestion of the corrosive firing byproducts. The system schematic is given in Fig. 32.

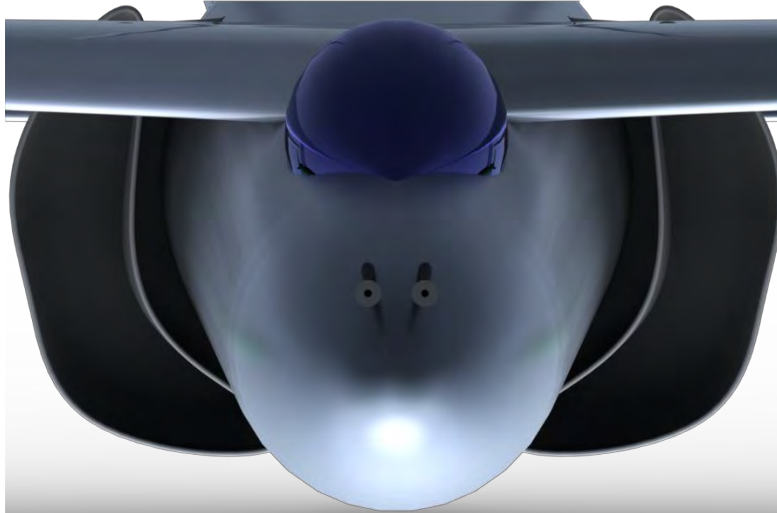


Fig. 31 Forward guns

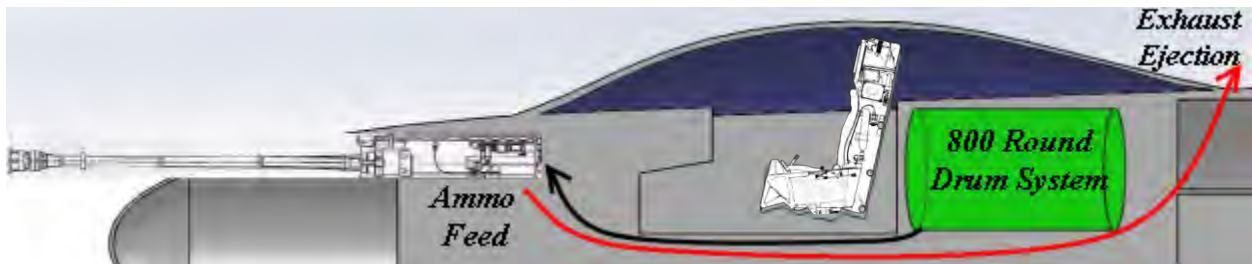


Fig. 32 Gun firing system [21]

Landing Gear and Nose Cone

The nose cone becomes one of the most contested areas for space within the aircraft as the gun, cockpit and associated avionics, forward sensing radar, and nose landing gear must all fit into the reduced diameter of the forward fuselage. Below in Fig. 33 is a midplane cross-section with all components properly sized in their respective spaces.



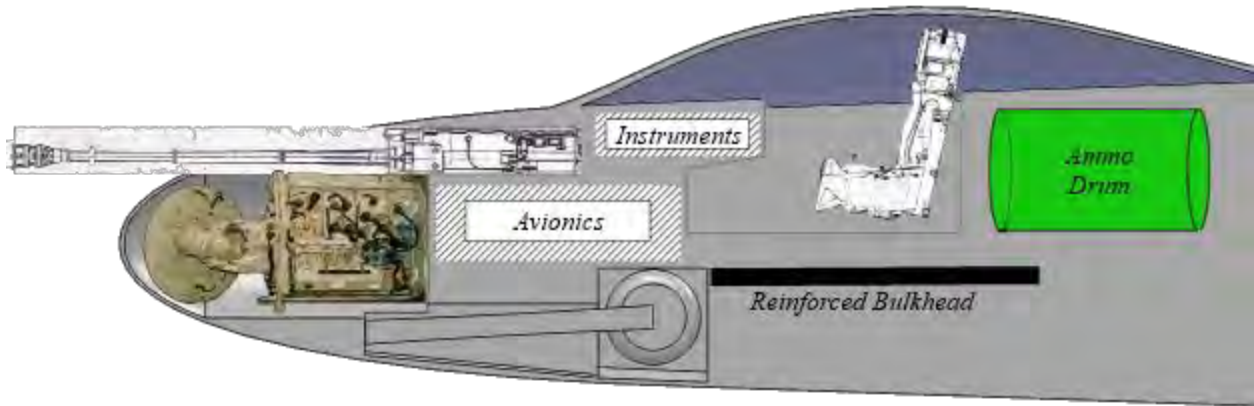


Fig. 33 Forward layout cross-section [21][22]

An advanced forward sensing radar inhabits a majority of the radome. Directly above the radar is allocated the twin cannon barrels. The nose gear bay is directly below which follows a simple direct aftward rotation scheme. Space for the cockpit instrumentations is included behind the panel, and the primary avionics bay resides above the landing gear bay. If vibrations from the guns are found too extreme in this area even with dampers, a second suggestion location for the avionics is below the reinforced bulkhead directly below the cockpit. This bulkhead is designed to protect the pilot from ground fire and bolster survivability. A standard zero-zero ACES II ejection system is also included in the cockpit. The canopy is hydraulically opened via a clamshell mechanism and entrance/egress is expected from the port side.

For the landing gear, a traditional tricycle configuration is selected. With the landing gear design several considerations and requirements must be met. A certain amount of clearance must be allowed between the tail cone and runway during takeoff rotation. The longitudinal center of gravity must remain sufficiently ahead of the main gear contact point in all loading configurations to prevent the aircraft from tipping backwards, and a proper combination of distance between the nose gear and main gear and wheel track must be struck to ensure lateral stability during ground operations. Below are the tricycle gear placement requirements as suggested by Roskam [23] in Fig. 34.



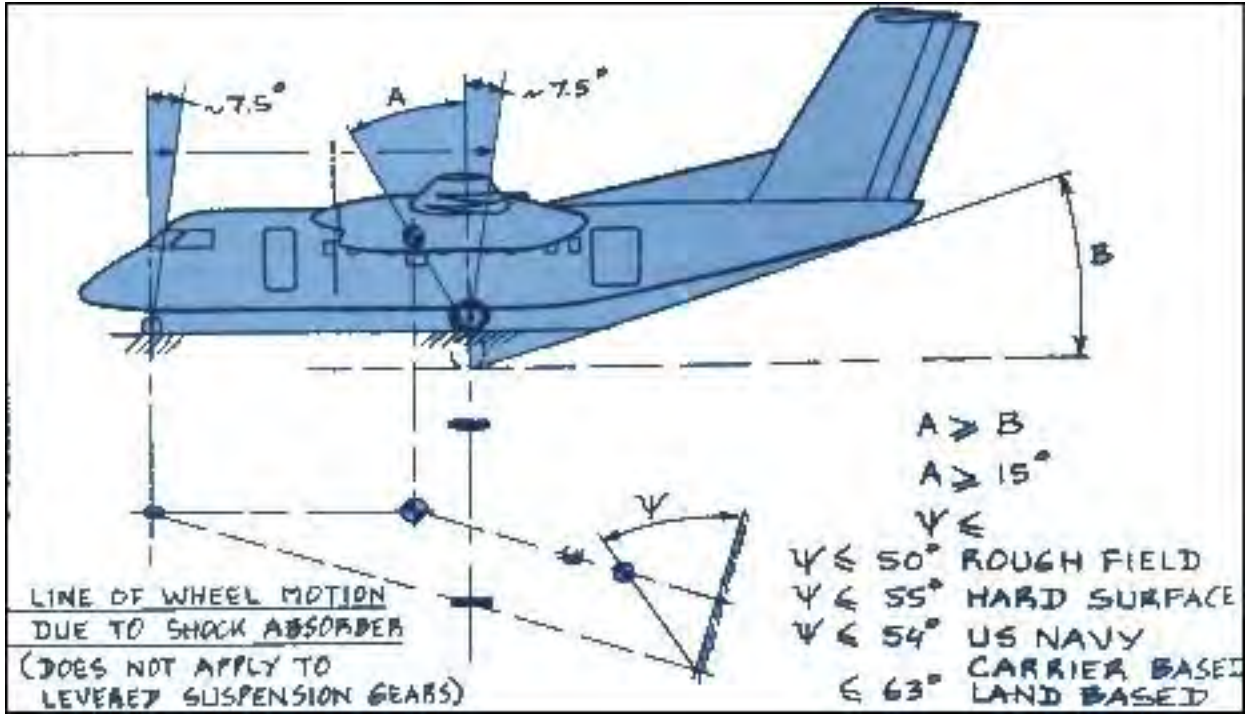


Fig. 34 Roskam tricycle landing gear requirements [23]

Per these requirements, the contact point with the ground of each gear from the datum point of the nose are listed in Table 29. The corresponding requirement angles in degrees from this configuration are listed in Table 30.

Table 29 Landing gear contact point locations

Gear:	Nose	Main
X Location	-46 in	-426 in
Y Location	± 3 in	± 66 in
Z Location	69 in	69 in
Tire	20 x 6 in	27 x 7.5 in

Table 30 Requirement compliance

Angle	Requirement	Actual Design
A	≥ 15	43.6
B	$\leq A$	20.0
Ψ	≤ 55	55.0



The challenge of this design is to balance enough height on the main gear to allow enough rotation clearance with the nose cone while keeping the center of gravity as close the ground as possible. The main gear is also placed behind the air intake to minimize the risk of Foreign Object Debris ingestion. The longitudinal requirements as listed in Table 30 are illustrated in Fig. 35.

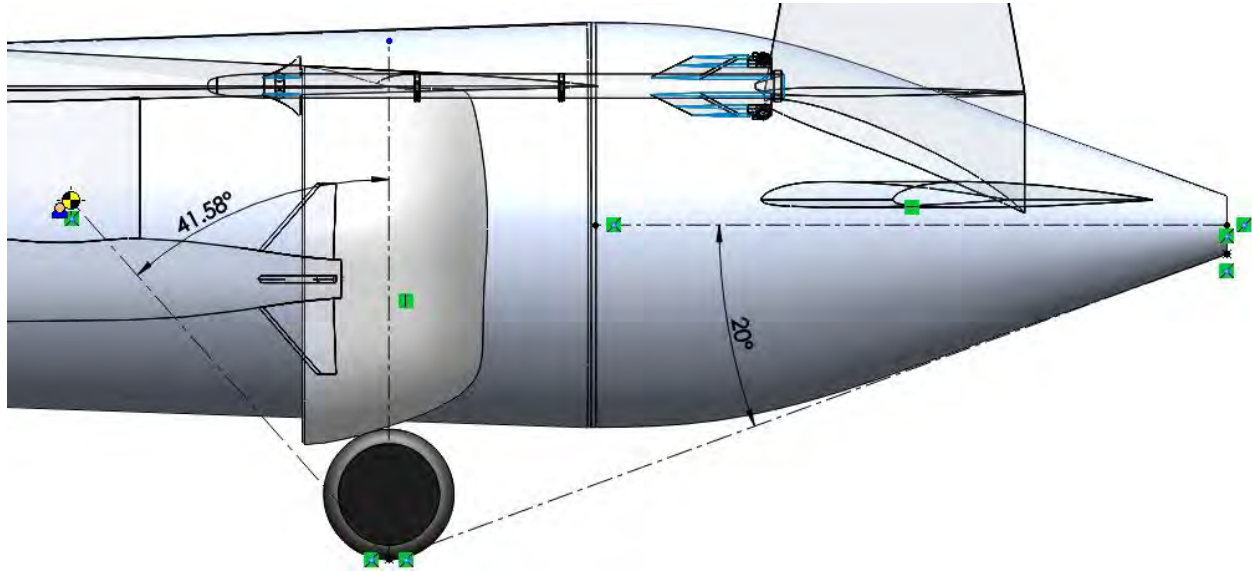


Fig. 35 Main gear longitudinal angles

The main gear also needs to maintain enough distance from the nose gear to keep the ground track distance reasonable. Even at the final locations along the X Axes, a wide ground track is required to maintain lateral stability. Because of this, a slightly more complex gear retraction scheme is required than for the nose gear. The gear first rotates inwards towards the centerline by hydraulic strut before rotating forward to the final retraction position shown in Fig. 36.

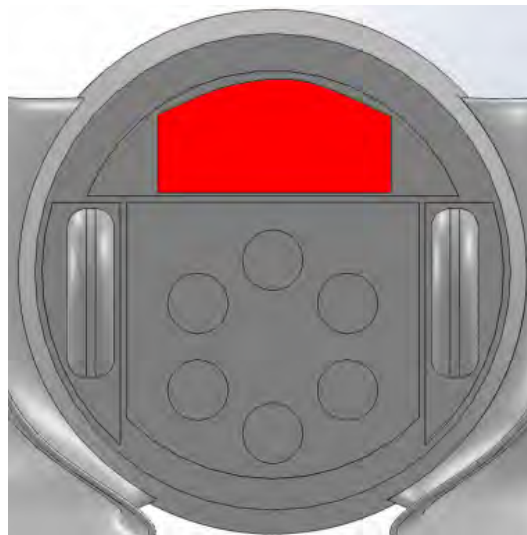


Fig. 36 Main gear retraction bay



Part XIII: Structures Design

Overall Design

The primary structural material for the overwhelming majority of the aircraft is standard aerospace-quality aluminum. This material is traditionally chosen for its light weight, strength, economy, reparability, and resistance to corrosion. Ultimately, employing tried and true techniques to the structure of the aircraft keeps cost and development time to a minimum, which in this design is considered more valuable than ‘squeezing out the last ten percent of performance for an extra thirty percent of the cost’.

The structure can be divided into three sections: the forward section which is predominated by the cockpit and increased system density, the more open center section which contains the wing box, weapons bay, internal auxiliary fuel tank, and landing gear bays, and the primarily hollow tail cone which also must connect the empennage. The overall layout of these major structures are placed relative to each other in Fig. 37.

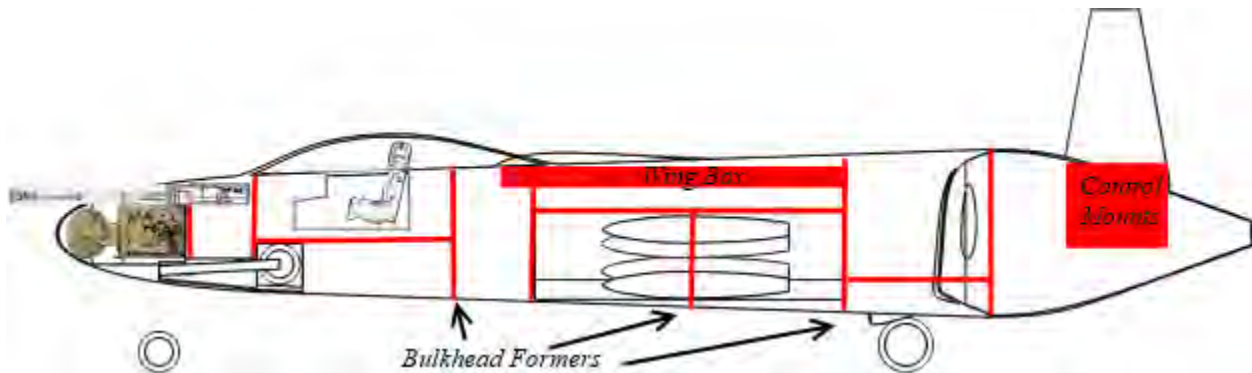


Fig. 37 Structural overview

Each vertical line represents a strengthening former placed in strategic locations on the aircraft where increased strength is expected to be required. For example, at the engine mount, surrounding the weapons bay, the primary wing structure integrated with the body fuel tank, surrounding landing gear, and surrounding the pilot. An Example former is given at the intersection of the weapons bay and landing gear bay in Fig. 38. These formers assist to bolster torsional stiffness along the longitudinal axes. However, these practices are universally standard for many aerospace structural applications. Because of this, much more time is spent to explain the structural analysis of this design’s modern innovation, the composite wing spar.



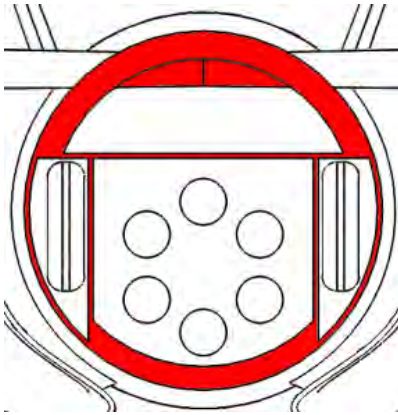


Fig. 38 Former cross-section

Composite Spar Design

Composites as a rule of thumb are expensive to produce and extremely difficult to repair, however, in this design the wing acts a major contributor to the total structural weight. Also, in terms of survivability and ease of repair, if the main spar of an aircraft is damaged, nine times out of ten the airframe can no longer remain salvageable. For these reasons, a composite spar and spar cap are designed as the primary wing structure to add performance without risks to ease of maintenance and at a fraction of the cost for a full composite design.

Fiber Reinforced Polymers (FRP) are a relatively new material that can be engineered to meet certain design criteria, such as high strength or low weight. They are usually designed by combining layers (lamina) of composites with different fiber orientations into one piece (laminate). The fiber length can be controlled in order to help dictate strength and production costs. For this design the fibers are considered continuous and continue throughout the composite. Although FRP's rarely reach the strength of metallic construction materials, they are a popular choice in construction projects whenever weight is a concern. Due to this, it is common to use FRP composites in the construction of commercial transport airplanes since high strength and low weight are high priority factors, although FRP will not be used in areas of critical load. The objective of this design is to withstand the loads and temperature changes while being as light and low cost as possible.

A schematic of the composite cross-section to be designed and the assumed applied loads can be viewed in Fig. 39. In that figure, $N_x = 8150$ kN, $N_y = 5800$ kN, and $M_x = -100$ kN-m are the assumed allowable loads expected on the aircraft. Interim SI units are utilized to satisfy the Laminator software utilized for the design.



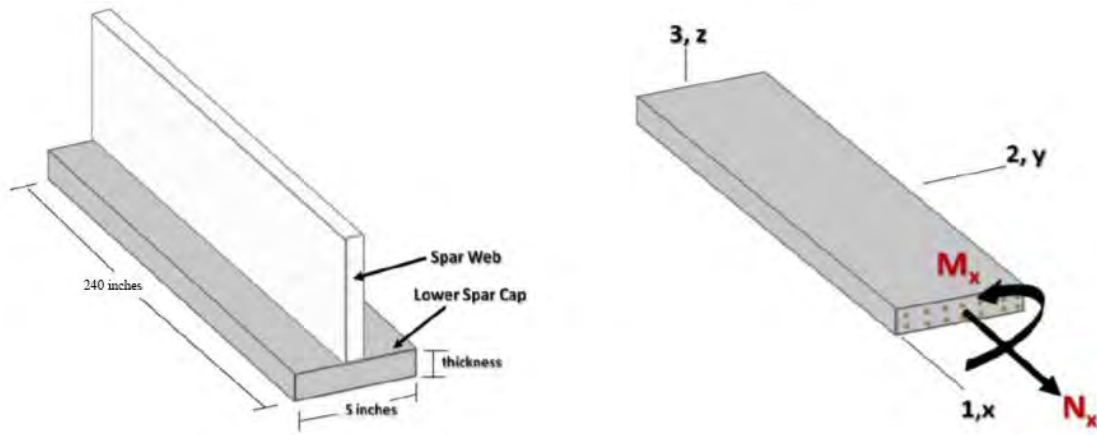


Fig. 39 Lower spar cap with general shape and dimensions

The next most important design goal is to minimize the composite cost and weight, mainly through minimizing the composite thickness. The cost and weight can also be controlled by changing the materials and the volume fraction. The final major design goal would be to control the coefficient of thermal expansion of the composite so that it closely matches the that of surrounding material of the aircraft. This is primarily to remove as much shear stress between the materials as possible. The rest of the aircraft is made out of aluminum which has an approximate coefficient of thermal expansion $24E-6 \text{ } ^\circ\text{C}^{-1}$ [24]; therefore this will be the coefficient that the design will aim for. It should be noted that the composite materials are constrained to epoxy and high modulus carbon fiber, so the design variables will be the stacking sequence, angle ply (which are constrained to $0, \pm 30, \pm 45, \pm 60, 90$), and the fiber volume fraction.

Before material selection, the constraints placed on the solution are first looked at. The design requires a material that can withstand large tensile loads. Other loads—temperature or moisture—are not accounted for, so high tensile strength is the driving force for material selection. There are many types of material that could be chosen from to satisfy the needs, however, for simplicity options are constrained to a composite consisting of an epoxy matrix and high modulus carbon fiber. In addition, for optimization the laminate thickness, weight, thermal coefficients, and cost must be considered. Cost is the limiting factor for material selection. The amount of money spent on material will limit thickness and how much thermal loading it can withstand.

To start, a high-modulus carbon fiber must be chosen. From Mallick, [25] one such carbon fiber with a considerably high modulus is the HMS-4 PAN carbon fiber. Internet research reveals a carbon fiber similar to this. This carbon fiber, developed by the Hexcel company named



HexTow® HM63 Aerospace, is a carbon fiber with a very high tensile modulus and loading strength. It is used mostly in the Aerospace Industry for use on aircraft. It immediately satisfied needs for both a high modulus, and a reasonable Coefficient of Thermal Expansion (CTE). There are other fibers to consider, but each is either too heavy, expensive, or contains insufficient information for fiber analysis.

Finally, an epoxy resin is chosen that will serve as the matrix for the carbon fiber. Overall, with a simple selection process, an epoxy that is used specifically for carbon fibers is chosen. The selected matrix is EL2 Laminating Resin. According to the Data Sheet, it has a high tensile strength to help support the carbon fiber, along with a high modulus [26]. In addition, it is light, cheap, and easy to use with the carbon fiber selected. Together, these two materials will help form a strong, sturdy material.

To narrow the design space from infinite possibilities with numerous unknowns, several reasonable assumptions must be accomplished. These slight estimations based on engineering intuition range from typical composite theory to broader assumptions about particular materials when not all mechanical empirical properties or data could be discovered. Assumptions eventually used in the design reduce to two major categories: composite theory assumptions and assumptions for the chosen materials' properties.

A few common assumptions suggested from Mallik [25] take the composite as perfect from the manufacturer, suggesting that there exist no voids and the bond between the fiber, matrix, and lamina stay perfect. All fibers in lamina are assumed to be exactly parallel, wetted, and ply angles exact. The fiber and matrix by themselves are considered to act nearly isotropic. Also, the laminate is assumed to contain no residual stress, no interlaminar stresses, and the effects of cyclic loading or moisture are not considered.

While the reported material properties and published data sheets contain many of the most common elastic constants, physical properties, and strengths, several holes are found when attempting to complete the extensive list of inputs required to run an iteration of the Laminator software. Values of coefficient of thermal expansion and poisson's ratio are assumed per Table 2.2 in Mallik [25] for the EL2 polymer matrix, as these values are not available from the manufacturer. In terms of material properties of the HM63, high modulus carbon fiber is much more complete with only poisson's ratio needing estimation from typical values supplied by Mallik. All shear modulus' are calculated by Eqn. 35.



$$G = \frac{E_{11}}{2(1 + \nu_{12})} \quad (35)$$

Ultimate strength estimation contains several of the larger assumptions, as typically only tensile ultimate strengths are listed for individual materials, and the multi-axial stress state listed in the design requires all strengths entered into Laminator. As the matrix is assumed isotropic, its tensile strength is assumed to be the transverse strength in both tension and compression. Pure compression strength is assumed to follow the buckling mode using Eqn. 36.

$$\sigma_{LCu} = 2 \nu_f \sqrt{\frac{\nu_f E_m E_f}{3(1 - \nu_f)}} \quad (36)$$

Shear strength is assumed to be one half of the longitudinal tensile strength. The final assumed materials are listed below in Table 31 [25][26][27][28][29].

Table 31 Assumed material values

Material Property	HM63 Carbon Fiber	EL2 Epoxy Matrix	Lamina
ρ	1.83 g/cm ³	1.10 g/cm ³	1.56 g/cm ³
E_1	441 GPa	2.90 GPa	265.8 GPa
E_2	~	~	0.890 GPa
G_{12}	183.8 GPa	1.12 GPa	4.38 GPa
ν_{12}	0.20	0.30	0.24
CTE ₁	-1.2*10 ⁻⁶ m/m °C	65*10 ⁻⁶ m/m °C	0.506*10 ⁻⁶ m/m °C
CTE ₂	~	~	18.42*10 ⁻⁶ m/m °C
σ_{LTu}	4.688 GPa	85 MPa	4.096 GPa
σ_{LCu}	~	~	2.79 GPa
σ_{TTu}	~	~	85 MPa
σ_{TCu}	~	~	85 MPa
τ_u	~	~	2.048 GPa
Cost	209.44 \$/kg	13.84 \$/kg	~

The intent of developing a design algorithm is to identify the relationships between different variables in the design space, and to identify design drivers that impact design objectives in the strongest fashion to focus the early design process. With the material values of density, cost, and all dimensions fixed except thickness, the two primary design variables become the total thickness, which impacts the final volume of the spar cap, and fiber volume fraction which impacts the material distribution of the volume. Where λ is the cost per kilogram of the material and l , w ,



and t are the length, width, and thickness of the spar cap respectively, the following two equations are derived from the rule of mixtures to find the total weight and cost of the designed spar cap.

$$W = w l t [\rho_f v_f + \rho_m (1 - v_f)] \quad (37)$$

$$C = w l t [\lambda_f \rho_f v_f + \lambda_m \rho_m (1 - v_f)] \quad (38)$$

The weight in Eqn. 37 is based simply on density times the volume of the spar cap, and Eqn. 38 extends this to cost by multiplying both the fiber and matrix weight by their respective cost per weight.

The following two figures map these equations onto contour plots of constant cost and weight over a range of 0.2-2.0 cm for thickness and 0.40-0.75 for fiber volume fraction.

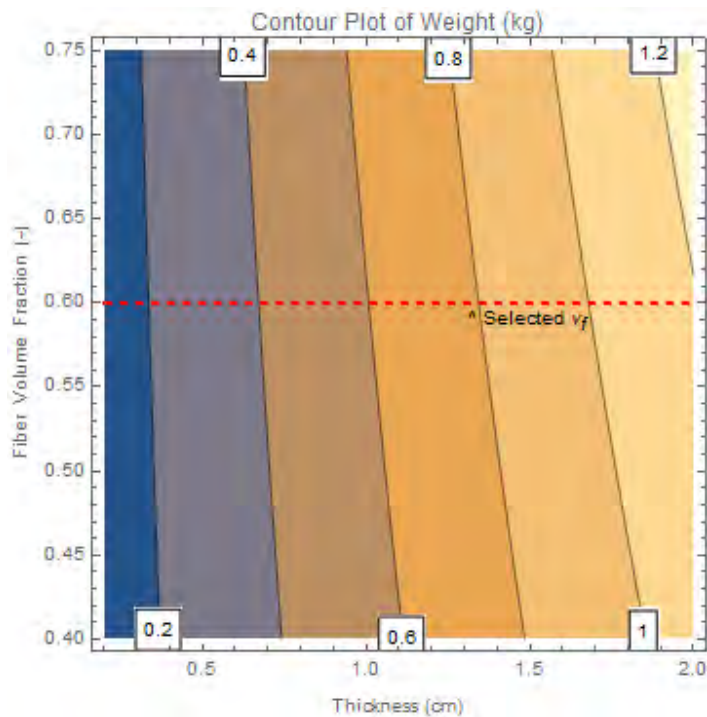


Fig. 40 Constant weight contour plot



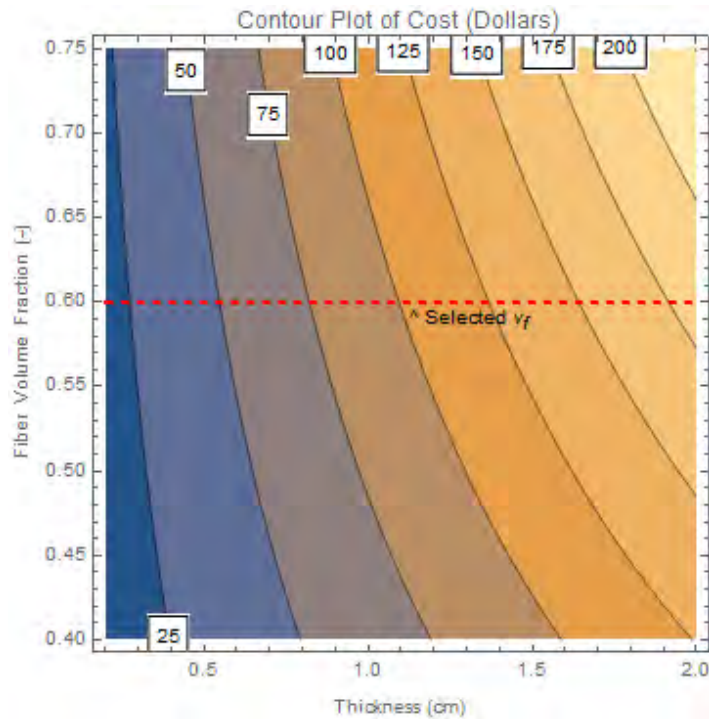


Fig. 41 Constant cost contour plot

As seen in Fig. 40, volume fraction plays a small part in total weight compared to total thickness. While volume fraction does affect cost more in Fig. 41, especially at higher thicknesses, total thickness once again proves the design driver in both weight and cost of the design where a reasonable volume fraction can easily be set as a constant. This leads to the following algorithm:

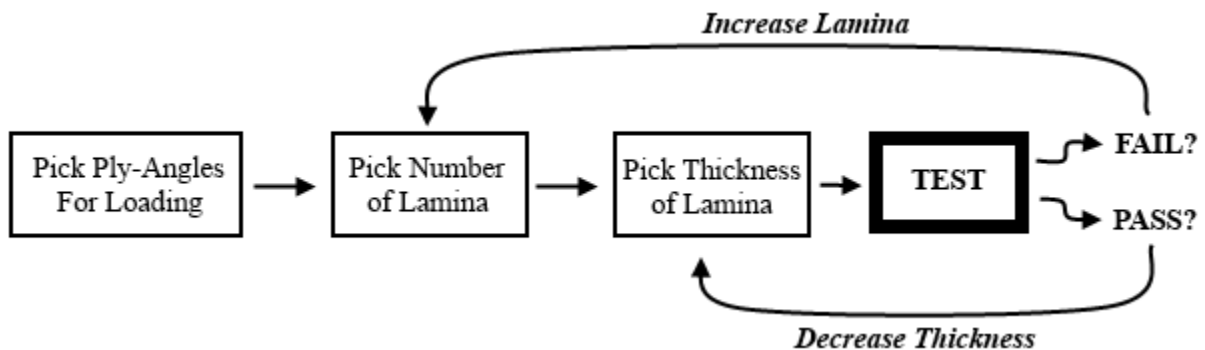


Fig. 42 Design loop

Figure 42 outlines the final iteration plan based on the relationships discussed in this section. As total thickness drives both cost and weight of the design, volume fraction is selected at a reasonable balance between cost and weight, and only thickness and number of lamina are varied once a ply-angle stacking is selected. This drives the thickness, and hence cost and weight, to minimize very close to the allowable stress in each lamina.



The first step towards determining the stacking of the laminate is to understand the loads given. Since there is a longitudinal moment applied, it is superior to put the 0° lamina on the far edges of the laminate to withstand the tension and compression generated by the moment. The lamina that withstands the moment generated compression needs to be a somewhat thicker since the ultimate compression strength of the lamina is lower in the compression mode. All the composite lamina also need to be designed to take into account the tension in the X-direction as well. Finally, for the transverse force in the Y-direction, a lamina of 90° and smaller thickness is required to take the load without fracture. A fiber volume fraction of 0.60 is selected as a reasonable compromise between strength and cost/weight after it is found 0.70 would become more expensive, and 0.50 would be heavier with less strength. After iterations following the previously described design algorithm for various thicknesses and orientations, the optimal result found is as shown in the Fig. 43 below:

Stacking Sequence

Enter the TOTAL number of layers in the full stack:

Enter the stacking sequence below:

Check here if this is a symmetric layup and enter only 1/2 of the stack

Layer	MatID	Ply Angle	Thickness
1	1	0	0.0046
2	1	90	0.0015
3	1	0	0.0045

Fig. 43 Best obtained result [0/90/0]

Figure 43 above shows the optimum design of the laminate with a total thickness equal to $0.0046+0.0015+0.0045=1.06$ cm.

Layer	Max Stress (+)	Max Strain (+)	Tsai Hill (+)	Hoffman (+)	Tsai-Wu (+)
1	1.05	1.05	1.02	1.03	1.16
2	1.08	1.08	1.08	1.08	1.12
3	1.27	1.27	1.26	1.26	1.20
---	-----	-----	-----	-----	-----
Min	1.05	1.05	1.02	1.03	1.12

Fig. 44 Failure analysis outcome



In Fig. 44 it is shown that all of the failure analysis criteria are larger than 1.0, which indicates that the laminate is safe and it is not going to fail under the given load. The Max Stress Criteria is utilized as a safe baseline to determine if the laminate withstood the load or not. Table 32 below lists the final characteristics of the designed spar cap.

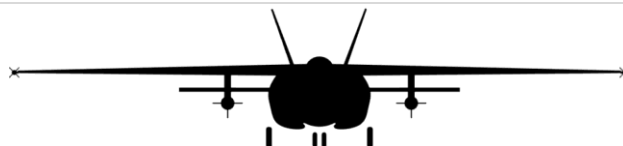
Table 32 Final design parameters

Characteristic	Value
Volume Fraction (v_f)	0.6
Thickness (t)	0.417 in
Weight per ft (W)	1.391 lb
Cost per ft (C)	\$ 96.86

Given an extended amount of time to dive into more complex sensitivity studies and iterate, a more optimal solution would eventually converge using the design algorithm. However, as is true with any system, to find a universally optimized solution, the entire universe must be searched. This presented solution represents the best current compromise found with the time available.

After running the parameters through the design algorithm and the Laminator software, analysis shows that under the given constraints the ideal stacking sequence is $[0,90,0]$ with a laminate thickness of 0.417 in. This setup withstands the applied loads on the system, and has a minimized thickness in order to minimize weight and cost. As for the goal of matching the CTE of the composite and the surrounding aluminum in the aircraft, this goal is partially met. Since aluminum is an isotropic material, it proves difficult to match the CTE in all directions for the composite. As it stands, the only ways to change the thermal properties of a composite is to change the fiber/matrix properties, which are constrained, or change the volume fraction of fibers. It is also decided that the volume fraction should be kept at 60 percent in order to retain composite strength and to prevent the fibers and matrix from debonding. However, the CTE_2 of the composite is close to the CTE of aluminum, so this goal is met, and the interstitial shear stress minimized.

The final weight of the composite is 1.391 lb per ft and the total material cost is \$96.86 per ft. This composite might not be cheaper than aluminum utilized in the rest of the design, but it is ~75 percent lighter than an equivalent volume of aluminum. Therefore, the most useful aspect for the use of an FRP in an aircraft is effectively utilized since low weight in an aircraft is more highly valued than the final cost of the material. These weight and cost percentages are fed back into the design optimization loop discussed previously in terms of added cost and saved weight.



Part XIV: Wing Design

Similar to weight sizing, the first step in designing a wing is not starting from scratch. Decades of experience and data designing wings exist, and these are used as inspiration to tailor to this mission. Wing data from selected relevant aircraft is listed in Table 33 [30].

Table 33 Historical wing data

Jet	Dihedral	Incidence	AR	Sweep	Taper	Max Speed
Lockheed S3A	2.5 (deg)	0.0 (deg)	7.9	15.0 (deg)	0.25	450 (KTAS)
Lockheed C-141	-3.5	0.0	7.5	25.5	0.41	492
Bae Nimrod	2.7	0.0	7.8	20.0	0.23	500
McDD KD-10	1.7	0.0	7.5	35.0	0.25	530
B7373	6.0	1.0	7.0	25.0	0.28	462
B7572	5.0	3.2	7.9	25.0	0.26	529
DC-9-50	1.5	0	8.7	24.0	0.18	537
Average	2.27	0.6	7.7	24.2	0.27	500
ZA-20	0.0	0.0	7.0	24.0	0.27	501

Following the procedure described by Roskam [30], the expected cruise lift coefficient is first calculated by Eqn. 39.

$$C_{Lcruise} = \frac{(W_{TO} - 0.5 W_{fuel})}{q S} \quad (39)$$

At the cruise condition, this gives a value of 0.36. Sweep angle at the quarter cord ($\Lambda_{1/4}$) is selected as the average from Table 33 as 24 degrees. These two parameters are combined with the desired critical Mach number of 0.80 for dash speed in Fig. 45 [30] which gives the optimal thickness ratio at the root for the wing.



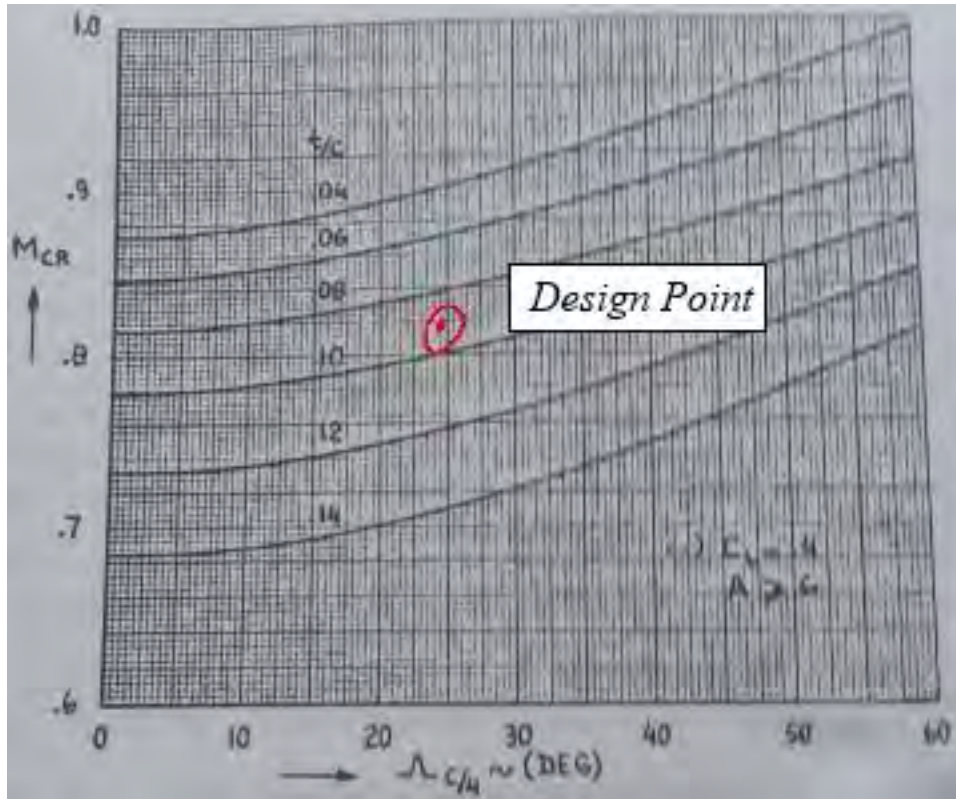


Fig. 45 Wing thickness ratio selection chart [30]

This results in a chord to thickness ratio of 0.09. Combining this value with the expected lift coefficient yields the selected root airfoil, the NACA23009. Also from the wing data the thickness ratio from root to tip typically decreases by about 25 percent, giving a thickness ratio at the tip of 0.07 which corresponds to the NACA23007 airfoil. These two airfoils are demonstrated below with relative chord size in Fig. 46 [31].

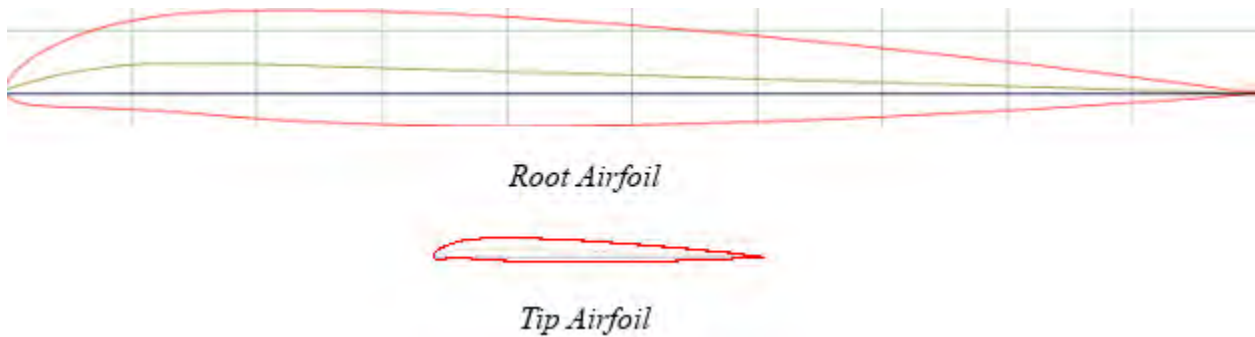


Fig. 46 Selected airfoils [31]



From the constraint sizing the final wing dimensions are as follows in Table 34.

Table 34 Wing numerical design

Parametric	Value
Area	594 ft ²
Wingspan	64.5 ft
Aspect Ratio	7.0
Sweep Angle	24.0 deg
Taper Ratio	0.27
Root Chord	14.5 ft
Tip Chord	3.9 ft

Figure 47 outlays the structural and control surface layout of the main wing. The main spars discussed in the previous section are placed at 0.25 and 0.75 percent of the chord respectively. Ribs are placed along the wing at 68 inch intervals and at key locations such as the boundary between ailerons and at the external store station. A simple slotted flap runs inboard with the bomb pylon allowing room for deployment. Internal fuel volume exists within the spars.

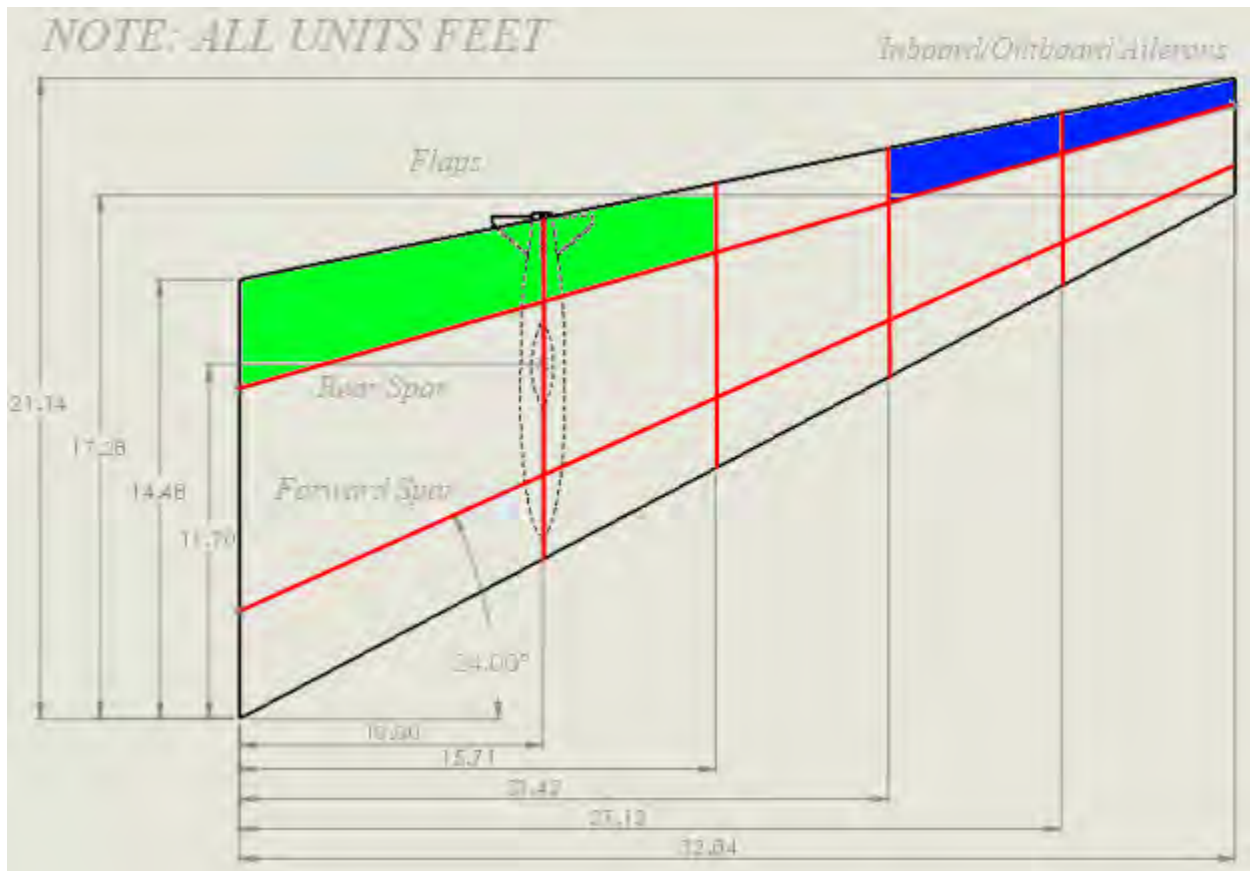


Fig. 47 Wing layout and structural dimensions



Internal fuel volume of the main wing is calculated by Eqn. 40, where λ_w is the taper ratio and τ_w is the thickness ratio of the tip compared to the wing. This calculates to equal 214 ft³, or 79 percent of the required mission fuel. Further fuel is added as needed to the center auxiliary tank.

$$V_{fuel} = 0.54 \frac{S^2}{b} (t/c)_r \left[\frac{1 + \lambda_w \sqrt{\tau_w} + \lambda_w \tau_w^2}{(1 + \lambda_w)^2} \right] \quad (40)$$

Finally, the vertical and horizontal stabilizers are dimensioned in Fig. 48 and Fig. 49.

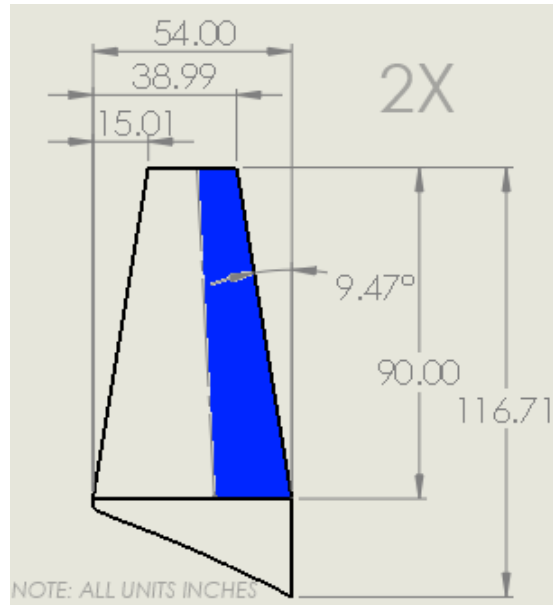


Fig. 48 Vertical stabilizer platform

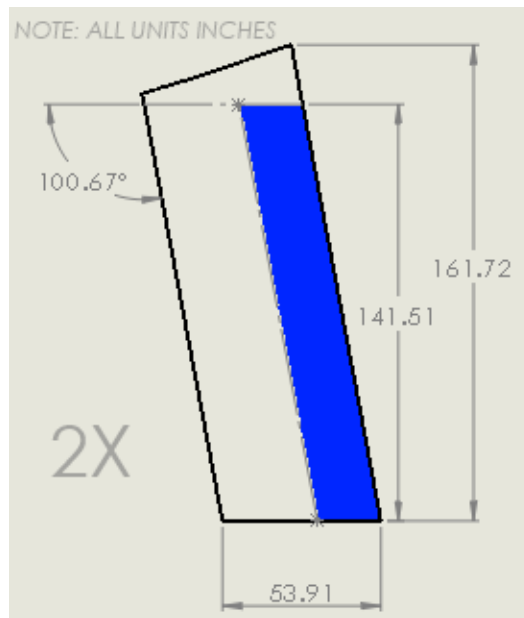


Fig. 49 Horizontal stabilizer platform



On both lifting surfaces the primary flight control resides on the assumed platform, and an extension is added to merge the surface with the tail cone. The twin vertical surfaces are offset from plumb by 20 deg to project lifting area in both the lateral and longitudinal directions, and the surfaces taper at a ratio of 0.44. The horizontal stabilizer does not exhibit any taper or angle relative to the Y-Axes, but does parallel the trailing edge of the main wing with a sweep of 16 degrees. This is both to allow any downwash to more easily interact with the secondary lifting surface, and also to reduce transonic effects similar to the taper of most modern jet aircraft. This is especially important that the empennage stall after the main wing to maintain control. The horizontal airfoil is the NACA2210 and the vertical airfoil is the NACA0010. The elevator consists of the final 40 percent of the horizontal stabilizer and the twin rudders occupy the final 45 percent of the vertical stabilizers chord wise.

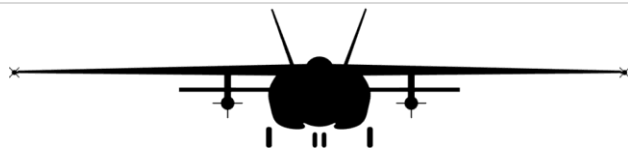
From the areas of these surfaces, the Normalized Vertical Volume (V_v) and the Normalized Horizontal Stabilizer Volume (V_h) as defined by Eqn. 41 and Eqn. 42 are listed in Table 35.

$$V_v = \frac{A_v l}{S b} \quad (41)$$

$$V_h = \frac{A_h l}{S \bar{c}} \quad (42)$$

Table 35 Lifting surface ratios

Parameter	Value
Length from Wing (l)	17.0 ft
Vertical Area (A_v)	79.0 ft ²
Horizontal Area (A_h)	144.8ft ²
Wing Reference Area	594.2 ft ²
Wing Span	64.5 ft
Average Chord	9.2 ft
V_v	0.0350
V_h	0.450



Part XV: Second Order Aerodynamics

Three additional aerodynamic analyses are initiated deeper into the design stage to test assumptions and form simulation-based data of a higher order of accuracy than basis methods. The deeper into any development project, the more in-depth testing must become. Once feasibility is established, the race against deadlines for optimization kicks off. Then, more fine-tuned but time intensive techniques like Computational Flight Dynamics (CFD) or Finite Element Analysis (FEA) are utilized.

To start, viscous analysis of the main wing is carried out in X-FOIL at cruise conditions and with a Reynolds Number of six million, lift and drag sweeps over expected angles of attacks are plotted in Fig. 50.

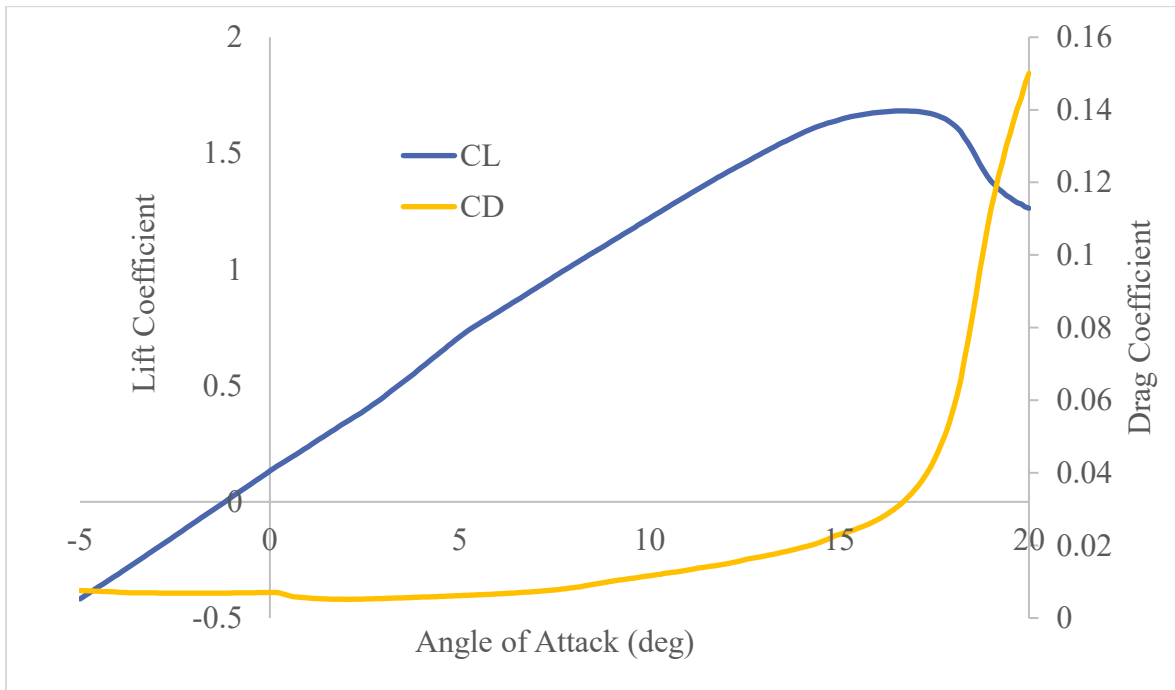


Fig. 50 X-FOIL viscous data

As expected, a stall now occurs which does not develop until approximately 17 degrees. Buffer is expected past 13 degrees as flow separation becomes apparent by the steep increase in drag. This data is combined to form a second order drag polar in Fig. 51.



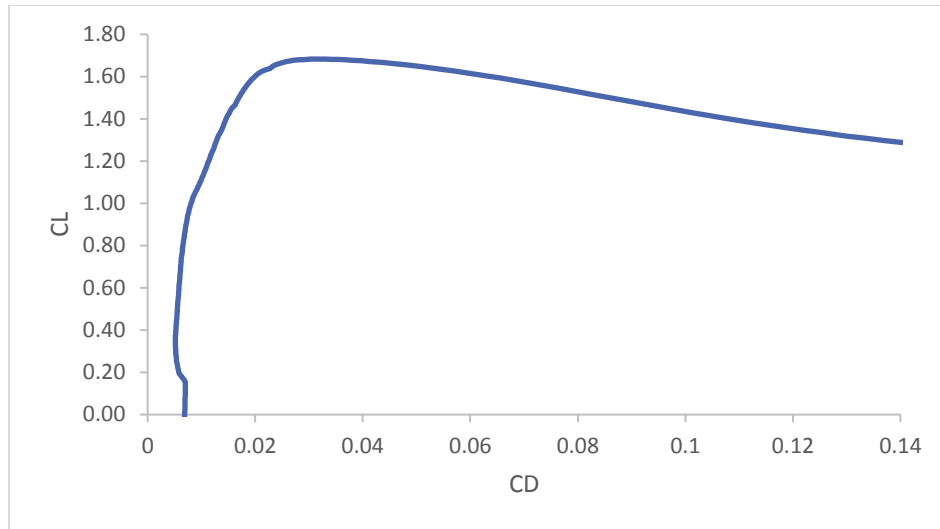


Fig. 51 Second order drag polar

Comparing Fig. 51 to Fig. 4, it is clear the two are not a direct comparison as the quadratic drag polar cited previously estimates drag from the entire size of the aircraft, while X-FOIL only considers induced drag. However, without the scaling effect, the shapes are directly comparable. Clearly then true viscous simulation finds the parabolic shape of the initial drag polar mostly correct, though closer to stall the parabolic assumption becomes no longer valid.

To fill in the computational gap for parasite drag, a platform and interference drag analysis is performed in Vehicle Sketch Pad. The modeled platform area of the aircraft is included as Fig. 52, and the results are listed in Table 36. This new parasite drag is higher than the initial estimate from weight to wetted area interpolation. This is likely from the wide fuselage diameter, external stores, and especially air intakes. This increased drag will need to be considered in further design.

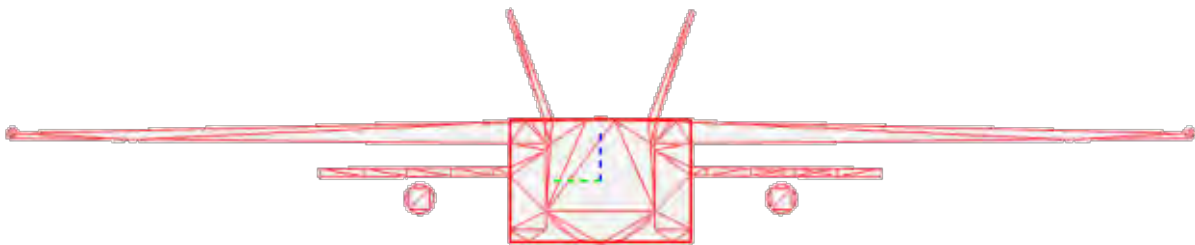


Fig. 52 VSP platform area

Table 36 Parasite drag comparison

Model	Output $C_{D,0}$
First Order Estimate [2]	0.0187
VSP Parasite Estimate	0.0201



At cruise, total drag coefficient considering both parasite and induced drag can now actively compare to induced lift with each value found numerically with second order techniques. This produces the lift to drag ratio plot for cruise in Fig. 53.

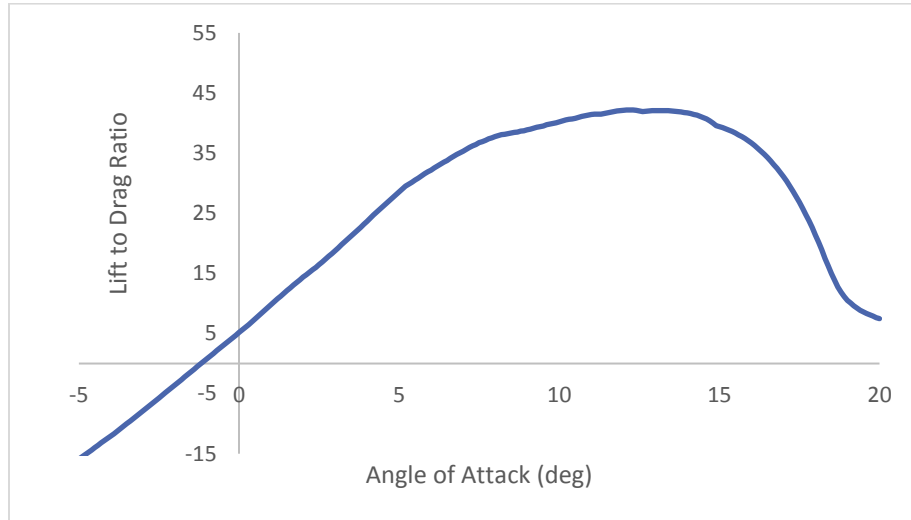


Fig. 53 Numerical lift to drag chart

Next, a model of the aircraft's lifting surfaces is built for Mark Drela's Athena Lattice Vortex (AVL) which creates individual panels based on the specified surface geometry where aerodynamic forces and resultants such as local induced lift, drag, downwash, and wake interference are calculated by the localized vortices at each panel. The lift distribution across all surfaces at the cruise condition is output as Fig. 54.

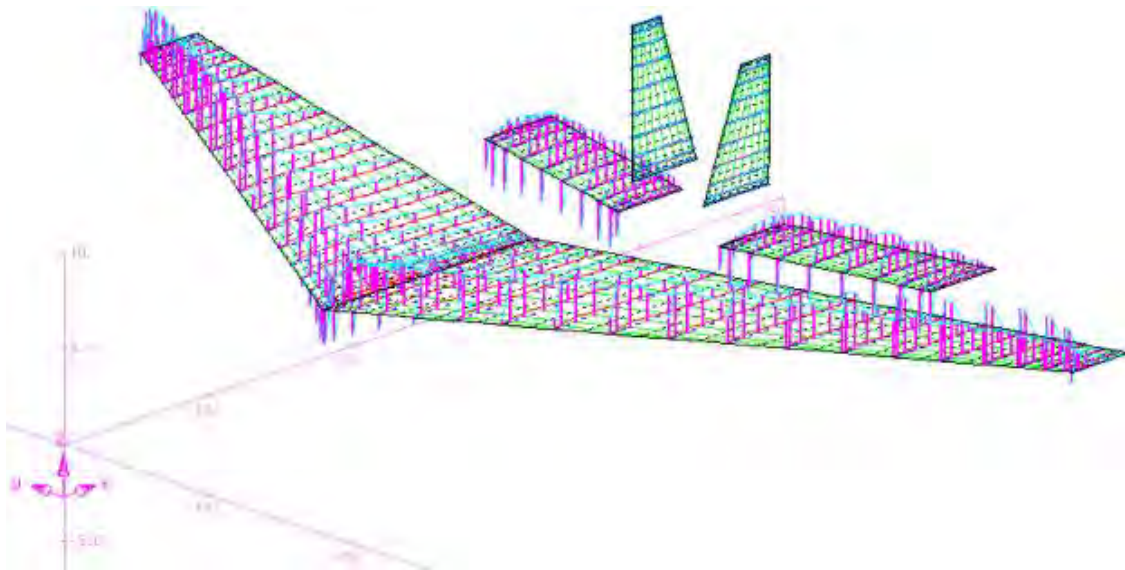


Fig. 54 AVL lift results at cruise condition



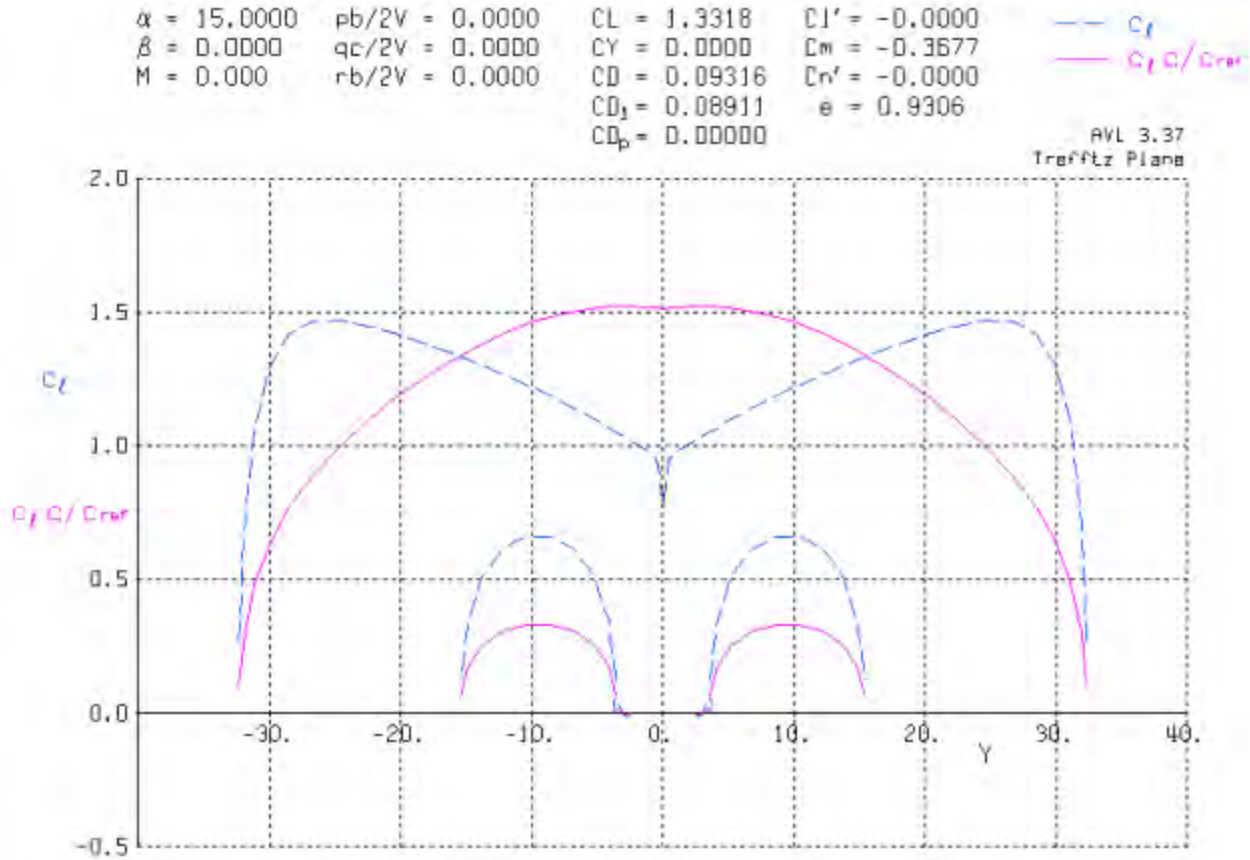


Fig. 55 Trefftz plot at 15 degrees AOA

Setting the aircraft to an Angle of Attack of 15 degrees and comparing the resulting Trefftz plot from Fig. 55, the results from Fig. 50 are confirmed. The maximum sectional lift coefficient at this angle of attack is approximately 1.5, and no portion of the wing has stalled. Beyond this point, the lift slope departs from the linear region, so the results of the Vortex Lattice Method quickly become untrustworthy, but at this maximum, models agree. A refined numerical lift model with verification is established, and no stall is expected before 15 degrees AOA.

Another important result of Fig. 55 is the lateral lift distribution. Although the wing itself becomes highly nonelliptical at high angles of attack, because of the location of the horizontal stabilizer, the overall lift slope becomes close to the theoretical optimal elliptical distribution. The wings would however likely benefit from some twist angle to normalize the sectional lift coefficient. As a final thought, in this configuration local destruction of lift at the wingtips does not seem to act as a concern. Lift sharply increases at the tips without intense indication of destruction of lift by strong tip vortices. This indicates that winglets are not necessary on the aircraft.



Part XVI: Weight and Balance

The first step in estimating first order component weights is once again to consult historical data. Similar components utilized in similar types of aircraft supply ballpark figures for future expectations. While a Risk Reduction Plan coupled with a grounded understanding of margins and projected mass growth is required, technology factors can be applied to estimate weight reductions for future innovation.

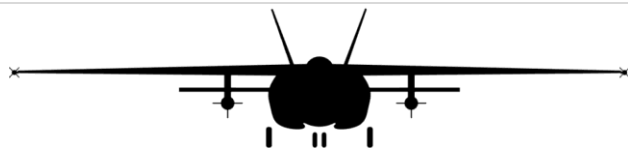
First the gross weight of the aircraft is calculated as 21,000 lb from Eqn. 43, and aircraft of comparable sizes and applicable missions are selected where detailed component weight information is available.

$$W_g = \frac{1}{2\eta_{max}} (\rho S C_{Lmax} V_A) \quad (43)$$

The three comparison aircraft include the F-4E, F-15C, and F/A-18A. The average weight of each component is taken as a percentage of total gross weight of the design. As these summed component weights do not quite equal the gross weight, an adjustment factor is added to converge the weights. The historical component weights and interpolated weights are listed in Table 37.

Table 37 Historical and calculated component weights [32]

Component	F-4E (lb)	F-15C (lb)	F/A-18A (lb)	Average (~)	ZA-20 (lb)
Wing	5,226	3,642	3,798	0.118	3,044.9
Empennage	969	1,104	945	0.028	727.1
Fuselage	5,050	6,245	4,685	0.149	3,838.6
Engine Section	166	102	143	0.004	99.5
Nose Gear	377	264	626	0.012	313.5
Main Gear	1,567	1,129	1,366	0.038	981.9
Engines	7,697	6,091	4,294	0.167	4,306.3
Air Induction	1,318	1,464	423	0.029	751.2
Fuel System	1,932	1,128	1,002	0.038	968.6
Propulsion System	312	522	558	0.013	339.8
Instruments	270	151	94	0.005	121.6
Surface Controls	1,167	810	1,067	0.029	737.3
Hydraulics	543	433	364	0.012	320.8
Electrical	542	607	547	0.016	409.2
Electronics	2,227	1,787	1,538	0.052	1,330.2
Armament	641	627	387	0.015	394.0
Air Cond.	406	685	593	0.016	408.2
Furnishings	611	294	317	0.011	291.9
Aux Gear	412	119	189	0.007	172.1



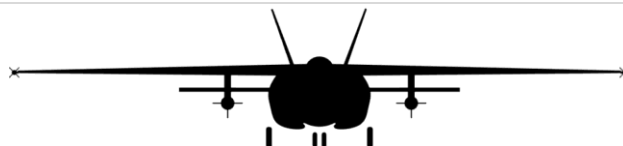
Where needed, extra information such as already known weights are included in the calculation. For example, from the Wing Design, it is known that the wing structure weighs 25 percent of what expected traditionally. The engine is also known to weigh 4750 lb [9]. These become constraints on the inner weight iteration loop discussed in a previous section. For the inner iteration loop, the weight of the aircraft without any expected technology improvements is calculated, and in outer loop the total normalized weight savings factor, or technology factor (η) is applied back to the initial weight regression coefficients found from Fig. 3 and Eqn. 5. Finding the weighted average, the technology factor is equal to 0.88. These new coefficients are found by Eqn. 44. where A' is the coefficient found purely from linear regression. The effect of this change keeps the regression slope the same, but moves it where the predicted empty weight is less along the entire envelope.

$$A = A' - B \log(\eta) \quad (44)$$

Combining the two loops as part of the iterative optimization scheme, convergence is reached when the output weights equal weight dictated by the technology factor. These weights combine with assigned locations to find the Center of Gravity in each configuration as Table 38.

Table 38 Empty center of gravity calculation

Component	Weight (lb)	Arm (ft)	Moment (ft-lb)
Wing	3,044.9	28.13	85,649.19
Empennage	727.1	44.79	32,563.99
Fuselage	3,838.6	19.29	74,037.91
Engine Section	99.5	40.00	3,980.51
Nose Gear	313.5	4.30	1,348.00
Main Gear	981.9	35.50	34,855.92
Engines	4,306.3	44.00	209,000.00
Air Induction	751.2	35.43	26,614.74
Fuel System	968.6	23.13	22,402.69
Propulsion System	339.8	40.00	13,593.19
Instruments	121.6	9.00	1,094.43
Surface Controls	737.3	42.63	31,432.44
Hydraulics	320.8	14.00	4,490.94
Electrical	409.2	10.00	4,091.85
Electronics	1,330.2	5.00	6,650.86
Armament	394.0	12.50	4,924.57
Air Cond.	408.2	9.00	3,673.42
Furnishings	291.9	9.00	2,627.34
Aux Gear	172.1	10.00	1,720.51



This gives an empty weight Center of Gravity (CG) location at Fuselage Station 28.24 ft. The same procedure is followed with a typical configuration expected at cruise to find a cruise CG at 28.25 ft. Again employing AVL, the Neutral Point along with other stability derivatives are output in Fig. 56.

Stability-axis derivatives...

		alpha		beta				
z' force	CL :	CLa =	4.675468	CLb =	0.000000			
y' force	CY :	CYa =	0.000004	CYb =	-0.204820			
x' mom.	Cl' :	Cl'a =	0.000000	Cl'b =	-0.070513			
y' mom.	Cm :	Cm'a =	-0.986671	Cm'b =	-0.000000			
z' mom.	Cn' :	Cn'a =	-0.000001	Cn'b =	0.050777			
		roll rate p'		pitch rate q'		yaw rate r'		
z' force	CL :	CLp =	0.000000	CLq =	7.385429	CLr =	-0.000000	
y' force	CY :	CYp =	0.098320	CYq =	0.000001	CYr =	0.102429	
x' mom.	Cl' :	Clp =	-0.426136	Clq =	-0.000000	Clr =	0.087687	
y' mom.	Cm :	Cmp =	-0.000000	Cmq =	-5.967454	Cmr =	0.000000	
z' mom.	Cn' :	Cnp =	-0.033916	Cnq =	-0.000000	Cnr =	-0.026513	
Neutral point		Xnp =	30.186081					

Fig. 56 AVL neutral point calculation

This neutral point is then compared to the calculated CG from the entire envelope of possible loading configurations of fuel and payload. To give an active idea of the stability margin as it changes with loading, the margin is defined as the difference between the current CG and Neutral Point, and is normalized by the average chord of the wing. When this is plotted as in Fig. 58, static margin in any condition can be read simply from the horizontal distance between that CG and the vertical line representing the Neutral Point. Figure 57 outlines the locations of the empty CG, neutral point, and average chord.

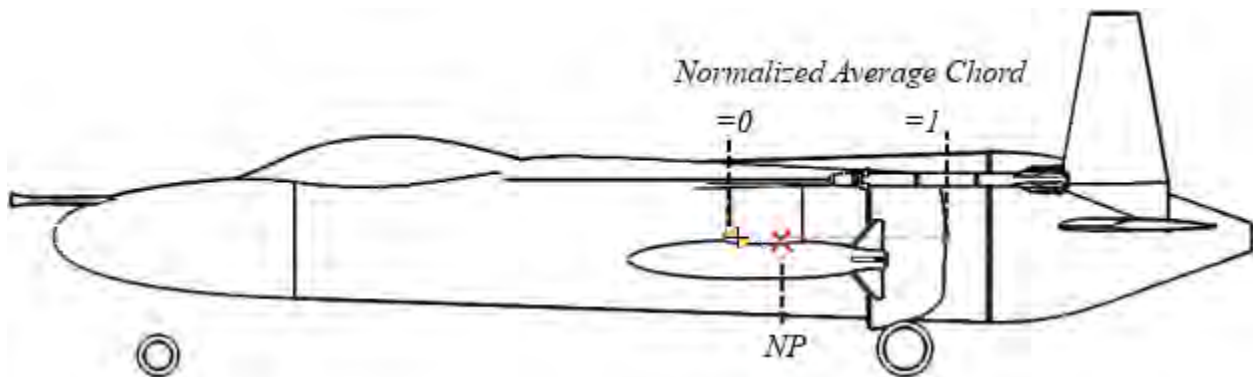


Fig. 57 Normalized chord locations



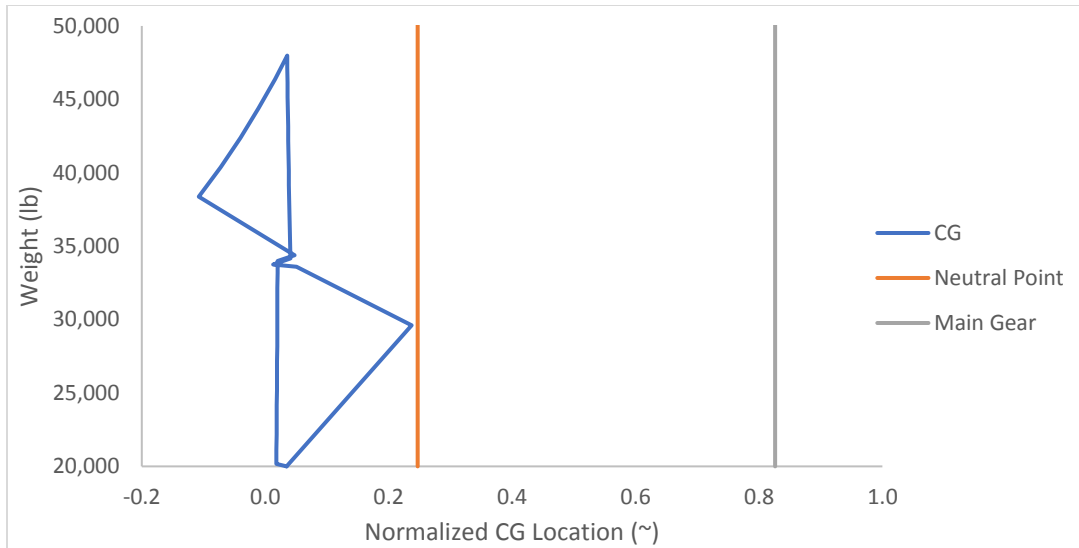


Fig. 58 CG excursion diagram

Following the CG envelope in Fig. 58 counterclockwise, first the pilot with associated gear and wing fuel tanks are filled as the initial vertical lines. The following shift backwards stems from adding AIM-9 Sidewinders to the two wingtip stations. The sharp shift forward from 35,000 to 40,000 lb results from the maximum 4,000 lb of stores attached at the two mid-wing hardpoints. The CG then creeps back to the typical range as payload is added in the weapons bay up to the takeoff weight of 47,000 lb. The vertical line again associates with fuel burn back to almost empty. The sharp shift to nearly the neutral point is driven from shedding the wing stores, and the final return to the empty weight location shifts as ordinance is again removed from the internal weapons bay.

Several important conclusions stem from these results. When using extremely heavy ordinance, the order of weapons drop will play a considerable factor in the location of the center of gravity of the aircraft. Static margin can shift between 35 percent to 2 percent based on payload loadout. The primary driver of these shifts however originates from the capability to carry 2,000 lb ordinance on the external stations. These weapons systems can be carried in the internal weapons bay as well, which greatly increases the flexibility of weight distribution. Without these large concentrations of mass, at most other loadouts the static margin remains around 10-15 percent which is the design point of the aircraft. The introduction of the larger ordinance, because of their position, tend to only push the static margin to increase to around 20 percent. At no configuration does the design become statically unstable, and as shown in Fig. 57 and Fig. 58 the CG always remains well forward of the main gear where tip back never becomes a concern.



Part XVII: Control and Dynamic Stability

Extending the Weight and Balance and Aerodynamic analyses, both are merged together to extend static stability to dynamic stability. First, the moment of inertia matrix of the aircraft is found placed around the CG. Next, the aerodynamic results of AVL are again used to find the full complement of aerodynamic stability derivatives. A linearized state space model of the system is then found using the aerodynamic derivatives normalized by the system parameters of moments of inertia and mass. Finally, the eigenvalues of these systems are found for use with expected damping and natural frequencies.

Inertia matrices of large complex systems are found numerically in SolidWorks around the previously described CG and then combined with other systems and masses as point masses using Eqns. 45-48. This numerical method is found close to the first order estimate of radius of gyration suggested by Roskam [32], and hence assumed more accurate. All other terms are assumed zero for symmetry, and the resulting matrix is given as Eqn. 49.

$$I_{xx} = \sum \left(W_i \left((Y' - Y_{cg})^2 + (Z' - Z_{cg})^2 \right) \right) \quad (45)$$

$$I_{yy} = \sum \left(W_i \left((X' - X_{cg})^2 + (Z' - Z_{cg})^2 \right) \right) \quad (46)$$

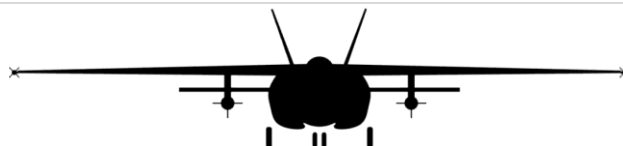
$$I_{zz} = \sum \left(W_i \left((X' - X_{cg})^2 + (Y' - Y_{cg})^2 \right) \right) \quad (47)$$

$$I_{zx} = \sum \left(\frac{W_i}{2} \left((Z' - Z_{cg})(X' - X_{cg}) \right) \right) \quad (48)$$

$$I = \begin{bmatrix} 15,305 & 0 & 179 \\ 0 & 111,780 & 0 \\ 179 & 0 & 125,693 \end{bmatrix} \text{slug} \cdot \text{ft}^2 \quad (49)$$

This finds that there is very little cross coupling which results from the CG sitting slightly off the X-Axis. The moment around the Z-Axis is also found to be much larger than that around the Y-Axis, and roll moment generally lower when empty.

Relevant stability derivatives taken in the body frame for both linear forces and moments with respect to linear and angular velocities as calculated by AVL are included below as Fig. 59.



Geometry-axis derivatives...

		axial vel. u	sideslip vel. v	normal vel. w
x force CX	:	CXu = -0.000261	CXv = 0.000000	CXw = 0.363579
y force CY	:	CYu = 0.000000	CYv = -0.204820	CYw = 0.000004
z force CZ	:	CZu = -0.483496	CZv = 0.000000	CZw = -4.694900
x mom. Cl	:	Clu = 0.000000	Clv = -0.072542	Clw = 0.000000
y mom. Cm	:	Cmu = -0.198892	Cmv = -0.000000	Cmw = -0.995693
z mom. Cn	:	Cnu = -0.000000	Cnv = 0.047835	Cnw = -0.000001

		roll rate p	pitch rate q	yaw rate r
x force CX	:	CXp = 0.000001	CXq = 0.231692	CXr = -0.000000
y force CY	:	CYp = 0.094024	CYq = 0.000001	CYr = 0.106385
z force CZ	:	CZp = -0.000000	CZq = -7.382146	CZr = 0.000000
x mom. Cl	:	Clp = -0.427670	Clq = -0.000000	Clr = 0.071175
y mom. Cm	:	Cmp = -0.000000	Cmq = -5.967454	Cmr = 0.000000
z mom. Cn	:	Cnp = -0.050428	Cnq = -0.000000	Cnr = -0.024980

Fig. 59 AVL stability derivatives

These body reference frame derivatives are used to find the stability of different flight modes using the linear approximation of an aircraft's equations of motion decoupled into longitudinal and lateral. The state space initially includes all nonlinear terms starting from free body forces. A Taylor Series expansion around the trim point of level, non-accelerating flight during cruise finds the final state space representation normalized by mass for all linear forces, and the relevant moment of inertia for moments per Fig. 60.



Linearized Longitudinal Dynamics (Symmetric Level flight equilibrium): Assumed $Z_q = 0, Z_w = 0$. (For stability axes: $\theta_0=0$ for a level flight equilibrium.)

$$\begin{bmatrix} \Delta \dot{u} \\ \Delta \dot{w} \\ \Delta \dot{q} \\ \Delta \dot{\theta} \end{bmatrix} = \begin{bmatrix} X_u & X_w & 0 & -g \\ Z_u & Z_w & u_0 & 0 \\ M_u + M_w Z_u & M_w + M_w Z_w & M_q + M_w u_0 & 0 \\ 0 & 0 & 1 & 0 \end{bmatrix} \begin{bmatrix} \Delta u \\ \Delta w \\ \Delta q \\ \Delta \theta \end{bmatrix}$$

In the above, all the force derivatives are normalized by the aircraft mass and the moment derivatives are normalized by the body y-axis moment of inertia, i.e.,

$$X_u = \frac{1}{m} \frac{\partial X}{\partial u}, \text{ etc.} \quad M_u = \frac{1}{I_y} \frac{\partial M}{\partial u}, \text{ etc.}$$

Linearized Lateral Dynamics (Symmetric level flight equilibrium): (Using stability axes, i.e., θ_0 is zero for a level flight equilibrium.)

$$\begin{bmatrix} \Delta \dot{v} \\ \Delta \dot{p} \\ \Delta \dot{r} \\ \Delta \dot{\phi} \end{bmatrix} = \begin{bmatrix} Y_v & Y_p & Y_r - u_0 & g \\ L_v^* + \frac{I_{xz}}{I_x} N_v^* & L_p^* + \frac{I_{xz}}{I_x} N_p^* & L_r^* + \frac{I_{xz}}{I_x} N_r^* & 0 \\ N_v^* + \frac{I_{xz}}{I_z} L_v^* & N_p^* + \frac{I_{xz}}{I_z} L_p^* & N_r^* + \frac{I_{xz}}{I_z} L_r^* & 0 \\ 0 & 1 & 0 & 0 \end{bmatrix} \begin{bmatrix} \Delta v \\ \Delta p \\ \Delta r \\ \Delta \phi \end{bmatrix}$$

In the above, all force derivatives are normalized by aircraft mass, all roll moment derivatives are normalized by I_x and the yaw moment derivatives are normalized by I_z .

$$Y_v = \frac{1}{m} \frac{\partial Y}{\partial v}, \text{ etc.} \quad L_v = \frac{1}{I_x} \frac{\partial L}{\partial v}, \text{ etc.} \quad N_v = \frac{1}{I_z} \frac{\partial N}{\partial v}, \text{ etc.}$$

$$L_v^* = \frac{L_v}{[1 - (I_{xz}^2 / (I_x I_z))]}, \quad N_v^* = \frac{N_v}{[1 - (I_{xz}^2 / (I_x I_z))]}, \text{ etc.}$$

Fig. 60 Decoupled linear state space model

The terms for $u, w, \theta,$ and ϕ are the values at the given flight condition for the longitudinal speed, vertical speed, pitch angle, and roll angle, respectively. Also, the non-dimensional stability derivatives, provided in Fig. 59 are multiplied by different reference values depending on the term. The directional force derivatives ($X, Y,$ and Z) are only multiplied by the wing reference area. The longitudinal moment derivatives (M) are multiplied by the wing reference area and wing mean geometric chord, and the lateral moment derivatives (L and N) are multiplied by the wing reference area and the wing span. These are normalized in AVL by these reference lengths input with the geometry file.



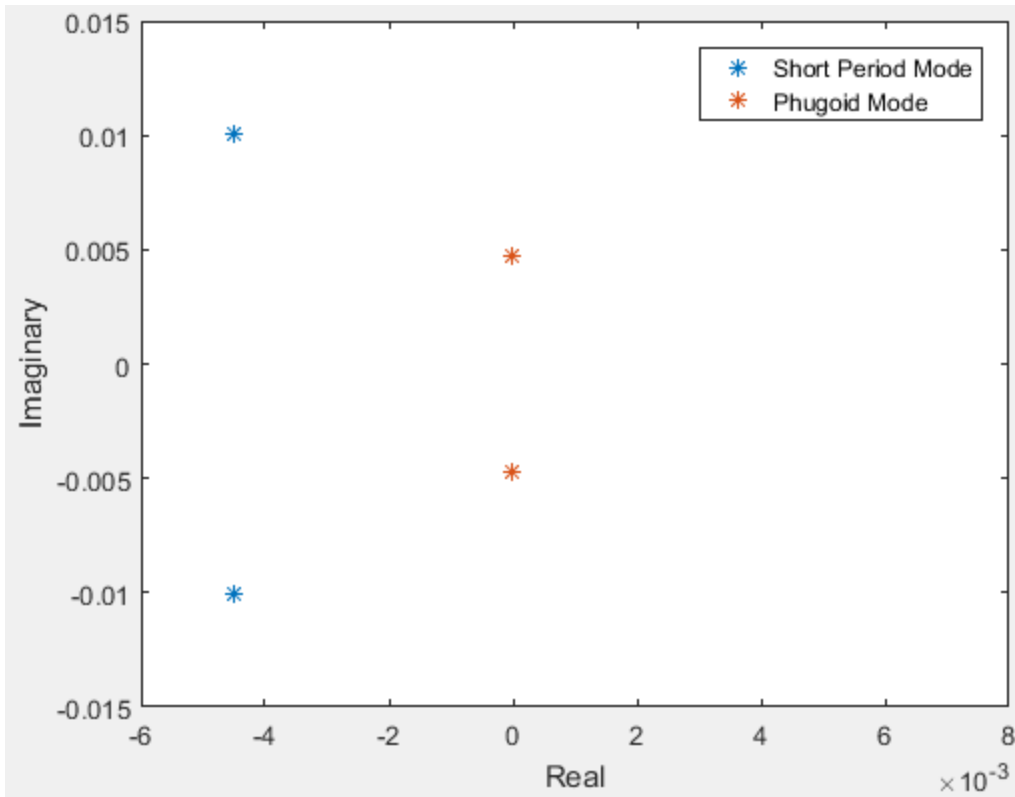


Fig. 61 Longitudinal mode poles

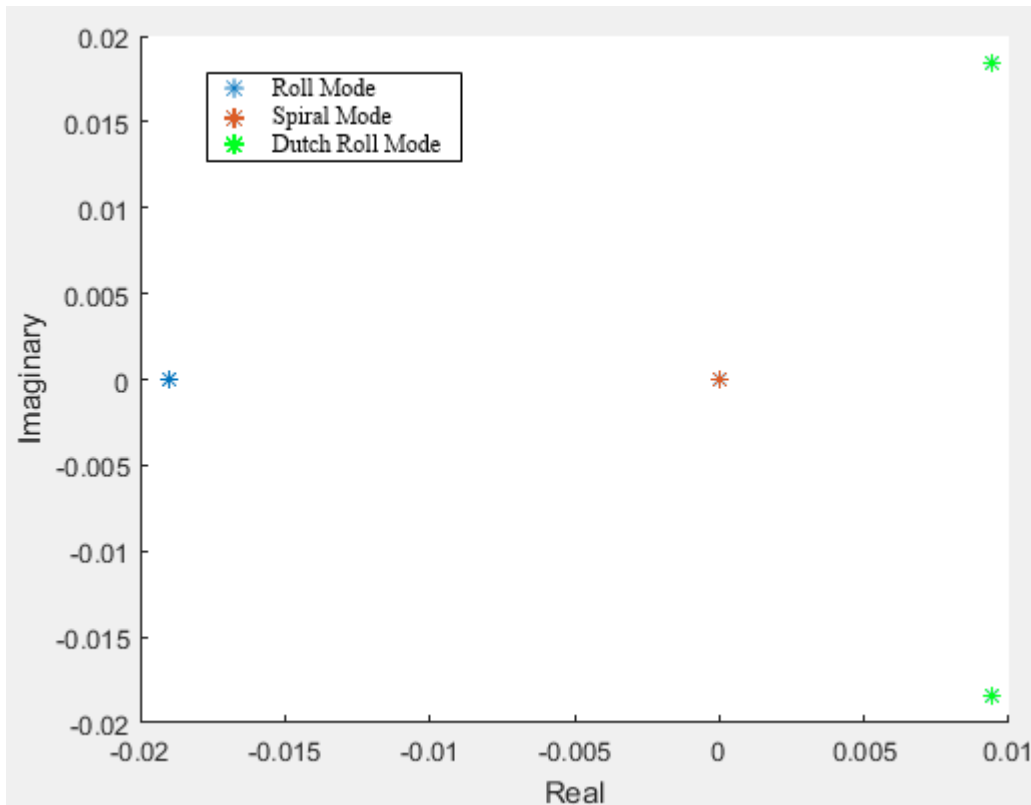


Fig. 62 Lateral mode poles



The resulting poles are mapped into the real-imaginary plane for both cases in Fig. 61 and Fig. 62. As expected, both modes for the longitudinal case are oscillatory. The phugoid mode is very close to zero on the real axis indicating minimal damping. The short mode is located farther away from the origin, as it will return to equilibrium more rapidly after any perturbation. For the short period mode, the flying qualities are determined solely by the damping the mode experiences. If this mode has a stable oscillation, it is considered to have good flying qualities. The phugoid mode is characterized by the time to halve the oscillation. The phugoid mode typically has a larger period, so its effects can more easily be corrected by the pilot or control systems.

In the lateral case, only the Dutch Roll, or roll yaw coupling has any imaginary poles. The roll moment is stable in the left-hand plane, while the spiral mode is marginally unstable. The roll mode flying qualities are based on the inverse of the magnitude for the roll eigenvalue which is the time constant for the response. The spiral mode flying qualities are determined in an identical fashion to the roll mode to obtain the doubling time. The final mode, the Dutch roll, is determined through a combination of the damping and natural frequency.

The corresponding modal statistics are listed in Table 39 as calculated by MATLAB. The military standards for each mode is listed for comparison in Table 40 [33].

Table 39 System dynamic modes

Dynamic Mode	Natural Frequency	Damping Ratio	Time Constant (s)	Doubling Time (s)
Short Period	0.011 (rad/s)	0.407	-	-
Phugoid	$4.74 \cdot 10^{-3}$	$2.01 \cdot 10^{-5}$	-	$7.27 \cdot 10^6$
Roll	0.019	1.0	19.1	-
Spiral	$6.7 \cdot 10^{-8}$	1.0	-	$1.04 \cdot 10^7$
Dutch Roll	0.022	-0.454	-	-

Table 40 Dynamic mode requirements

Dynamic Mode	Level I	Level II	Level III
Short Period	$1.3 \geq \zeta \geq 0.35$	$2.0 \geq \zeta \geq 0.25$	$- \geq \zeta \geq 0.15$
Phugoid	$\zeta \geq 0.04$	$\zeta \geq 0$	$T_2 \geq 55$
Roll	$\tau \leq 1.4$	$\tau \leq 3.0$	$\tau \leq 10$
Spiral	$T_2 \geq 12$	$T_2 \geq 8$	$T_2 \geq 4$
Dutch Roll	$\zeta \geq 0.04; \omega_n \geq 0.4$	$\zeta \geq 0.02; \omega_n \geq 0.4$	$\zeta \geq 0; \omega_n \geq 0.4$

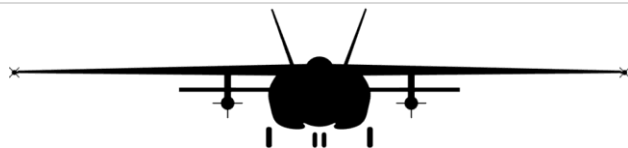


Overall it proves apparent the design is satisfactory in the longitudinal flight modes. The short period damping ratio is within the top Level I requirement, and the Phugoid mode sits at the end of its Level II requirements. This marginal stability stems from the designed undersized horizontal stabilizer. In an attack aircraft marginal longitudinal stability with very little damping is viewed as a positive. The aircraft may be tasked with Ground Following where high pitch rates prove desirable in proximity to the ground. By the same extension, during ground strafing runs the aircraft is essentially diving at the target, and the longer the run continues, the closer to the ground the aircraft becomes, but the better chance of making successful hits. By these factors target fixation can develop, and the ability to quickly pull away from the ground increases safety. With so little damping, Pilot Induced Oscillation (PIO) does become a concern. While attack pilots are some of the best pilots in the world and have exercise in sensitive aircraft, careful introductory training will likely prove beneficial to prevent overall control in transitioning pilots. An active feedback control system could also be designed for monotonous portions of flight where extra maneuverability is not necessary.

With the current configuration and small vertical control surfaces, lateral dynamic stability proves much more on the cutting edge in terms of stability. The time constant for roll is too slow at its current state which indicates that increased roll authority is required moving forward. In terms of the balance between Dutch Roll and Spiral stability, Spiral is currently very overpowered, as its doubling time is much greater than the requirement. The Dutch Roll is unstable and will require at least a yaw damper to soothe out this coupled flight mode.

In conclusion, the current stick-fixed open loop dynamic modes are satisfactory, if marginally stable longitudinally. The aircraft is also naturally unstable laterally. This is not uncommon however, and especially in modern military aircraft where higher pilot workloads are expected in the interest of higher maneuverability. The simple inclusion of a tuned yaw damper and throttle control system could easily remedy most minor dynamic stability issues primarily for the benefit of pilot fatigue, as this aircraft allows for extended operation.





Appendix: Bibliography

- [1] Chantrill, Christopher. *usgovernementspending*. n.d. Web. 25 April 2018.
- [2] Roskam, Jan. *Airplane Design Part I: Preliminary Sizing of Airplanes*. Lawrence: DARcorporation, 2005. Print.
- [3] Johnson, Carl. *CFM56 Engine Deck Data*. 2018. Excel Sheet.
- [4] Hunter, Jamie. *Jane's All the World's Aircraft: In Service 2017-2018*. Surrey: Jane's Information Group, 2016. Print.
- [5] Jackson, Paul. *Jane's All the World's Aircraft: Development & Production 2017-2018*. Surry: Jane's Information Group, 2016. Print.
- [6] Anderson, John. *Fundamentals of Aerodynamics 5th Ed.* . New York: McGraw-Hill, 2011. Print.
- [7] Mattingly, Jack. *Aircraft Engine Design*. Reston: AIAA, 2002. Electronic.
- [8] Millett, Merlin. "Rolling Coefficient of Friction of Rubber Tires." Retrospective Theses and Dissertations. 1957. Electronic.
- [9] "CFM LEAP Overview." CFM. Data Pamphlet. 2017. Electronic.
- [10] Nicolai, Leland. *Fundamentals of Aircraft and Airship Design Volume I*. Reston: AIAA, 2010. Electronic.
- [11] Collinson, R.P.G. *Introduction to Avionics Systems 2nd Ed*. New York: Kluwer Academic , 2003. Electronic.
- [12] "CIT Selects CFM56-5B for New A321 Aircraft." CFM. Online Report. 2015. Web.
- [13] Wright, T. P. "Factors Affecting the Cost of Airplanes." *Journal of the Aeronautical Sciences* (1936): 122-128. Electronic.
- [14] Hess, R. W. "Aircraft Airframe Cost Estimating Relationships: Fighters." Research Report. 1987. Electronic.
- [15] "Jet A Properties." Environment Canada, Emergencies Science and Technology Devision. Data Report. 1998. Electronic.
- [16] Raymer, Daniel. *Aircraft Design: A Conceptual Approach*. Washington: AIAA, 1992. Electronic.
- [17] "Military Pay Chart." Department of Defense. 2018. Electronic.



- [18] Tangopaso. *CFM Leap Image*. 2013. Web.
- [19] United States Air Force. *Conventional Rotary Launcher*. 2010. Web.
- [20] Thaimilitaryandasianregion. *Northrop F-20 Tigerhawk*. 2016. Web.
- [21] NavWeaps. *35mm/1000 KDG Millennium GDM-008*. 2017. Web .
- [22] radartutorial.eu. *Airborne Multimode Radar*. 2015. Web.
- [23] Roskam, Jan. *Airplane Design Part IV: Layout of Landing Gear and Systems*. Lawrence: DARcorporation, 2005. Print.
- [24] Hidnert, P., and H.s. Krider. "Thermal Expansion of Aluminum and Some Aluminum Alloys." *Journal of Research of the National Bureau of Standards* 48.3 (1952): 209. *National Institute of Standards and Technology*. Web. Accessed 13 March. 2018.
- [25] Mallick, P K. *Fiber Reinforced Composites: Materials Manufacturing and Design*. 3rd ed., CRC Press, 2007.
- [26] "EL2 Epoxy Laminating Resin." *Easy Composites*, easycomposites.co.uk, 2016. Accessed 12 March 2018.
- [27] "EL2 Epoxy Laminating Resin Technical DataSheet." *Easy Composites*, 2016
- [28] "HexTow HM63 Carbon Fiber Product Data Sheet." *Hexcel*, Hexcel Corporation, 2016.
- [29] Smith, Eric M. "RE: Hexcel Carbon Fiber Inquiry." Message to Ryan Morse. 25 March 2018. E-mail.
- [30] Roskam, Jan. *Airplane Design Part II: Preliminary Configuration Design and Integration of the Propulsion System*. Lawrence: DARcorporation, 2005. Print.
- [31] *Airfoiltools.com*. 2018. Web. 17 February 2018.
- [32] Roskam, Jan. *Airplane Design Part V: Component Weight Estimation*. Lawrence: DARcorporation, 2005. Print.
- [33] "MIL-F-8785C." Department of Defense. Requirement. 1980. Electronic.

